Investigation of Mechanical Performance and Formability of Welded and Brazed Sheet Materials

INVESTIGATION OF MECHANICAL PERFORMANCE AND FORMABILITY OF WELDED AND BRAZED SHEET MATERIALS

BY:

MOHAMMED SHAKER,

B.A.Sc., M.Sc.

A THESIS

SUBMITTED TO THE DEPARTMENT OF MECHANICAL ENGINEERING

AND THE SCHOOL OF GRADUATE STUDIES

OF MCMASTER UNIVERSITY

IN PARTIAL FULFILMENT OF THE REQUIREMENTS

FOR THE DEGREE OF

DOCTOR OF PHILOSOPHY

Doctor of Philosophy (2017)
(Mechanical Engineering)

McMaster University
Hamilton, Ontario, Canada

TITLE:	Investigation of Mechanical Performance and Formability of Welded and Brazed Sheet Materials
AUTHOR:	Mohammed Shaker M.Sc., (Mechanical Engineering) Military Technical College, Cairo, Egypt.
SUPERVISOR:	Dr. Mukesh Jain
EXTERNAL SUPERVISOR:	Dr. James Chen, CanmetMATERIALS, NRCan
NUMBER OF PAGES:	xxviii, 181

This work is dedicated to military personnel and all the law-enforcement who put their lives at risk to save our lands.

Mohammed Shaker

Abstract

In the last two decades or so, hybrid structures from dissimilar materials and/or sheet gauges have been developed to achieve weight reduction while maintaining or even improving structural performance such as stiffness, crash and impact behavior. In particular, welded and brazed sheet materials in the form of tailor blanks (TBs) are being increasingly used or considered for future applications in different applications such as automotive, aerospace and marine constructions as they offer attractive combination of strength and performance in applications where weight reduction is desirable. However, technical problems are often encountered during forming of TBs from dissimilar base sheet materials with different thickness and/or strength. These include weld line movement and non-uniform deformation. Additionally, there are premature weld failures due to the presence of softening zone (as in TBs made from advanced high strength steels), and brazed interface failure due to insufficient bonding and wetting (as in TBs made from steel and aluminum). These areas of forming of TBs need to be scientifically studied to advance the use of dissimilar materials.

The current research involves an understanding of deformation and forming behavior of steel-to-steel tailor welded blanks (TWBs) made from advanced high strength steel (AHSS) such as dual phase (DP780) steel. The research also involves a study of deformation behavior of steel-to-aluminum tailor brazed blanks (TBBs). TWBs have been

successfully joined using a relatively new welding techniques such as defocused fiber laser welding. TBBs, on the other hand, have been successfully produced by fiber Laser/MIG hybrid brazing and Cold Metal Transfer brazing (CMT).

In addition, the formability of TWBs of different gauges and/or strengths was tested by using a new, simple and reproducible method of formability testing using a double-layer blank method. This method was devised and assessed for testing various steel combinations in different strain paths such that the weld line stayed in position with respect to forming tools and is subjected to the same stress and strain state as the parent material in the weld and its vicinity. Moreover, results from conventional stretch forming tests, single-layer blank, and the double-layer method were compared at the macroscopic level (such as weld line movement, forming limit etc.) as well as at the microscopic level (such as failure location within the weld and failure mode) to isolate the advantages of the proposed double-layer method.

With regard to TBBs made by fiber Laser/MIG and CMT brazing methods, a fundamental knowledge and understanding of the local deformation behavior and material plastic flow in and around the brazed steel-aluminum interfaces were obtained by conducting miniature tensile mechanical tests that focus on continuous observation of the brazed region under a high magnification optical microscope to assess the ductility of the brazed joint and its capacity to carry the load during a material shaping process.

Acknowledgements

First of all, great thanks to ALLAH (God) for his mercy and continuous support all through my life. I have no knowledge except whatever he has taught me. He is the all-knowing, the all wise.

I am honored to convey my deepest sense of gratitude and thankfulness to all the persons who have guided me through this dissertation. They have bestowed on me the best consultation, cooperation and advice to make this dissertation possible and to assist me in receiving a Ph.D. degree.

I want to say that no words can be enough to express my gratefulness, deepest gratitude and respect to Dr. Mukesh Jain, for his invaluable supervision and continuous encouragement. I would like to thank Dr. James Chen from Canmet materials (CMAT) for his active thesis supervision and kind cooperation in leading welding and brazing work. I would also like to gratefully acknowledge the help and support of Dr. Shanker and Dr. Eu-gene who kindly agreed to serve on my doctoral committee and provide advice and supportive comments to help me move towards successful completion of my dissertation.

I am indebted to Dr. Mike Bruhis for his laboratory assistance and friendship. Many aspects of this work depended on his time, patience, and insight. His insights were always instructional and timely. I am also very grateful to my colleagues Dr. Anantheshwara, Dr. Zhutian Xu, and Ibrahim Abdelaty for their collaboration, friendship, fruitful discussions, and insightful feedback.

Special appreciation goes to the technical staff, Ron Lodewyks, Michael Lee, Mark MacKenzie, and John Colenbrander for their technical support.

Most importantly, neither appreciation nor gratitude could payback the patience and love of my family. I would like to express my love and gratitude to my mother for her inspiration and encouragement. Also, special thanks to my dear Wife, Marwa, and my daughters, Mirai, Lamar, and Nuray for their sacrifices, patience and enormous support. None of this would have been possible without their love, patience and encouragement.

Last but not least, I would like to thank my country, Egypt, for funding and supporting my research, and to Canada for partially funding all research related expenses through Dr. Jain's NSERC discovery grant.

Abbreviations

AHSS	Advanced high strength steel
BM	Base metal
CCT	Continuous cooling transformation
CMT	Cold metal transfer
CP	Complex-phase steel
CW	Continuous welding
DP	Dual phase steel
FLC	Forming limit curve
FLD	Forming limit diagram
FZ	Fusion zone
GMAW	Gas metal arc welding
HAZ	Heat affected zone
HSLA	High strength low alloy steel
HSS	High strength steel
ICHAZ	Intercritical heat affected zone
IMCs	Intermetallic compounds
IPPS	In-plane plane strain
LDH	Limit dome height

MIG	Metal inert gas
MS	Martensitic steel
PW	Pulsed welding
SCHAZ	Subcritical heat affected zone
TBBs	Tailor brazed blanks
TBs	Tailor blanks
TIG	Tungsten inert gas
TRIP	Transformation induced plasticity
TWBs	Tailor welded blanks
TWIP	Twinning induced plasticity
UCHAZ	Supercritical heat affected zone
UHSS	Ultra-high strength steel

Contents

List of Figures

List of Tables

Chapter 1

Introduction

The demand for lightweight automotive, aerospace, and marine structures to reduce energy consumption as well as to enhance mobility at lower costs has led to much research and development effort in finding alternative solutions for constructing such structures. In the last two decades or so, with advances in joining processes and techniques, hybrid structures from dissimilar materials and/or sheet gauges have been developed to achieve weight reduction while maintaining or even improving structural integrity such as stiffness and crash behavior. In particular, welded and brazed sheet materials in the form of tailor blanks are being increasingly used or considered for future usage in different applications such as transportation industries as they offer attractive combination of strength and performance in applications where weight reduction is desirable. Therefore, tailor blanks have become an area of interest for many researchers in order to obtain a sound joints as well as an acceptable level of plastic deformation required for shaping components from them after welding or brazing.

1.1 Tailor blanks (TBs)

TBs are blanks that consist of two or more sheets of different chemical compositions, mechanical and physical properties, thicknesses, and surface treatments that are joined together typically by a welding process. Such blanks are stamped into the required three dimensional shapes to create structural components for automotive, aerospace, marine, defense and other industries. TBs allow the use of thicker and/or stronger materials in regions of components that require higher stiffness and strength, whereas a thinner sheet is utilized in low stiffness and strength regions to reduce the total weight of the component. The distributed weight, strength, and stiffness, and consequent weight reduction offer the opportunity for reduced energy consumption while maintaining equivalent or better structural integrity compared to monolithic sheet of uniform thickness. In other words, using TBs enables designers and engineers to tailor the properties of the blank and yet meet or even exceed the current service performance of a particular component. Figure 1.1 shows one of applications of TBs concept in automotive industry.

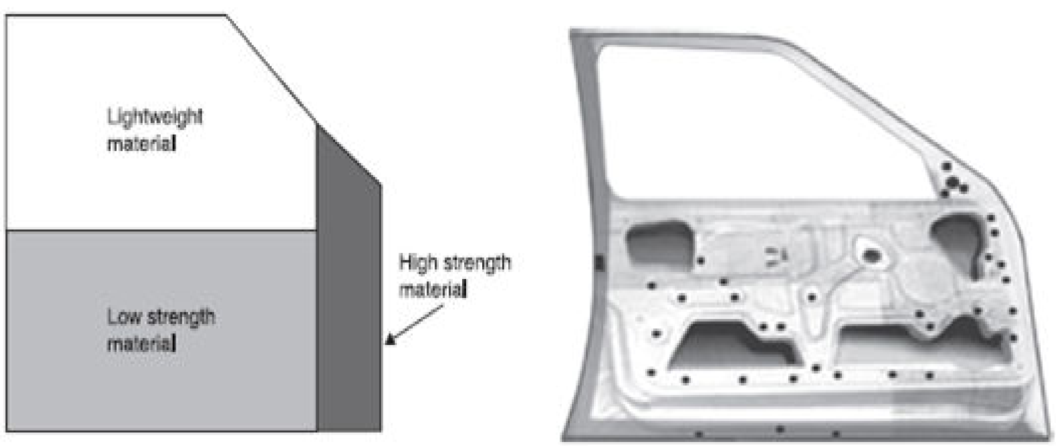

Figure 1.1. Inner door panel from TBs in automotive industry (Kinsey and Wu, 2011).

The benefits from TBs further extend to overall cost reduction due to decreasing scrap material and possibility to use materials trimmed off during blanking operation to produce TBs for another application, and consequently, minimizing the total manufacturing cost. Also, the technology offers benefits in terms of noise reduction, improved part stiffness and enhanced dimensional consistency and accuracy (Kinsey and Wu, 2011).

Joining dissimilar combinations of materials such as steel-to-steel and steel-to-aluminum by welding and/or brazing, however, is often challenging due to their different thermo-physical and mechanical properties that require yet untested welding and forming approaches. Moreover, increased inhomogeneity of the blanks due to the use of very different materials and weldment can affect the formability of the TBs which results in increased wrinkling and propensity for tearing failure during stamping process (Padmanabhan *et al.*, 2011). The quality of a steel-to-aluminum brazed joint is expected to be more critical than that of a steel-to-steel welded joint since in welding, a complete melting of the parent materials occurs and a more homogeneous and larger weld region is present. A brazed joint, on the other hand, consists of a sharp and distinct steel/aluminum interface with brazed material deposited all around this interface to provide interface strength (see Figure 1.2).

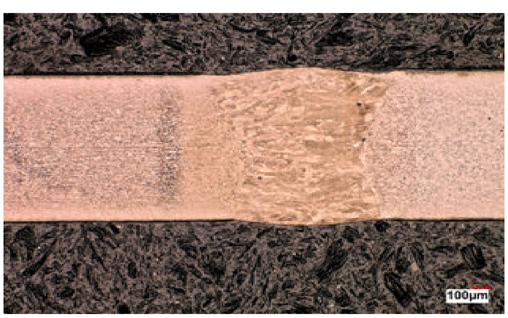

(a) Steel-to-steel welded interface.

(b) Steel-to-aluminum brazed interface.

Figure 1.2. Optical micrographs of joined interfaces for (a) steel-to-steel welded interface, and (b) steel-to-aluminum brazed interface.

1.1.1 Steel-to-steel tailor welded blanks (TWBs)

Steel sheets, and primarily low carbon and mild steels, remain the most commonly used materials in TB stamping, due to their consistent properties, excellent ductility, weldability and lower fabrication costs (Mallick, 2010). Predominantly ferrite microstructure of these steels results in sound welds of good ductility but with relatively lower strength levels. The attempts at improving the strength of these steels using mechanisms such as grain refinement, solid solution strengthening and precipitation strengthening typically result in a decrease in formability and more complex weld microstructures in tailor welded blanks. This trade-off in formability had previously limited the use of higher strength steel and hence thinner gauge steel sheets in the automotive industry (Hilditch *et al.*, 2015).

For the past two decades, fuel efficiency, lowering carbon emissions and passenger safety have been the main drivers in designing automobiles. Vehicle weight reduction represents the main strategy to minimize fuel consumption. Automotive structures that have a higher energy absorption in a crash situation would be ideal for enhancing passenger safety. Lighter vehicles structures have mutually opposing effects as fuel economy is ensured but safety can be seemingly endangered. So, there is an increasingly interest to replace the low strength larger ductility steels with high strength steels (HSS) and subsequently advanced high strength steels (AHSS) in TWBs. This will enable manufacturers to use thinner gauge steel sheets in TWBs to achieve total weight reduction of vehicles without compromising passenger safety (Shome and Tumuluru, 2015). It is projected that, by 2025 the usage of higher strength steels such as HSS, AHSS and UHSS steels would reach 80% of average weight of auto body with closures whereas, this weight would decrease by 150∽200 lbs (Ducker Worldwide, 2014).

Nowadays, the number of TWBs that are incorporated in each vehicle is accumulated due to the great progress in welding processes. It is expected that more TWBs will be utilized for both weight and production cost saving. Currently, most chassis and body structural members are being made from TWBs. Figure 1.3 shows recent applications of TWBs in automotive industry (ArcelorMittal, 2015b).

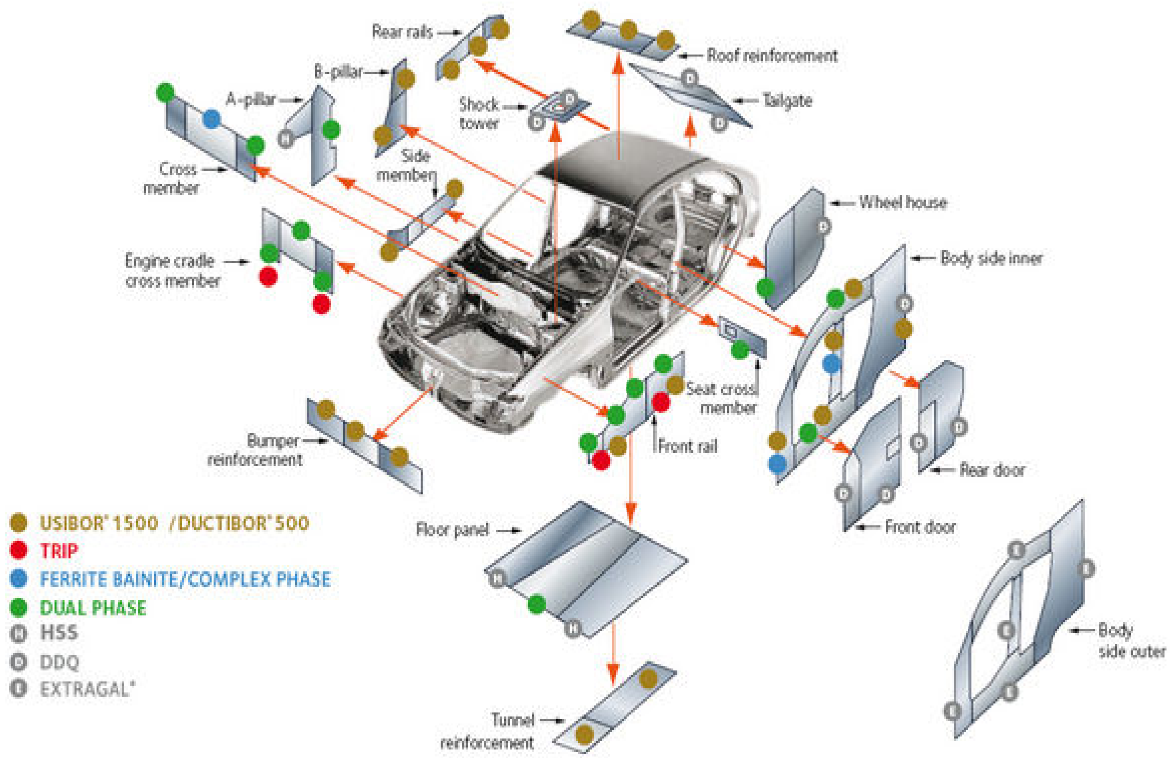

Figure 1.3. Applications of TWBs from steel grades in automotive industry (ArcelorMittal, 2015b).

1.1.2 Steel-to-aluminum tailor brazed blanks (TBBs)

With greater emphasis on environmental regulations and fuel efficiency, lightweight metal alloys such as aluminum alloys and magnesium alloys, are being increasingly utilized in fabricating automotive, aerospace, and other body structures and skin panels.

Low density, high specific strength, corrosion resistance and dimensional stability make these lightweight metal alloys the preferred choice for many applications (Padmanabhan *et al.*, 2011).

Aluminum alloys are utilized in structures for their low density, good workability, superior corrosion resistance and recyclability. Therefore, many conventional all-steel body structures nowadays are being considered for replacement with hybrid steel and aluminum parts, initiating development of technologies for joining of aluminum to steel (Yang *et al.*, 2015). For example, by 2025 in North America, 16% of all the body structure and closure parts, on a volume basis, for light vehicles will be made of aluminum sheets. This means, aluminum sheets for light vehicle bodies and closure parts will grow from less than 1 billion pounds in 2015 to nearly 4 billion pounds by 2025 (Ducker Worldwide, 2014).

Tailored blanks (TBs) made from joining steel and aluminum sheets for subsequent shaping are of much interest to the manufacturing industry. Such a combination, if properly joined, can provide benefit from higher structural rigidity of steels and the lightweight of aluminum, thus integrating the best of both worlds. Brazing is especially attractive for creating tailored steel/aluminum blanks. However, there are many insurmountable challenges to weld the two materials together that are highly incompatible in terms of their thermo-physical properties (this is explained in more details in the literature review).

1.2 Anticipated challenges and issues

Although much progress has been made in the recent years towards welding and forming of many steels, challenges remain for welding and subsequent forming of high strength-to-low strength steel sheets as well as for joining and forming of steel-to-aluminum sheets. Welding and forming of tailored blanks made from parent materials with large differences in thermo-physical and mechanical properties as well as significant differences in thickness is more complex and challenging. More fundamental studies to understand their mechanical and forming behavior to overcome the challenges are needed.

1.2.1 Challenges in welding dissimilar materials

The main objective of any welding process is to obtain a successful joint, i.e., acquiring sufficient tensile strength and ductility as well as fatigue strength so that the joint will not fail in the weld during service. The challenges of joining dissimilar material are summarized as follows (Kannatey-Asibu, 2009):

- The difference in melting temperatures of the two metals, especially due to heat involved during welding, results in earlier melting of one metal than the other when both materials are subjected to the same heat source. This can produce hot tear (a tensile failure) due to weld bead solidifying while the lower melting base material is hot and not strong enough.

- Differences in composition of the materials and lack of solubility between them can lead to the formation of secondary phases such as intermetallic compounds (IMCs) that may make the weld brittle for subsequent plastic deformation.

- Different coefficients of thermal expansion of the two materials increases the internal (residual) stresses in the intermetallic zone during any temperature change in the weldment. Service failure may occur if the intermetallic zone is extremely brittle.

- Discrepancy in thermal conductivity coefficients can result in inadequate amounts of fused metal in the weld.

- Electrochemical difference between the two metals can accelerate corrosion at the IMCs zone.

1.2.2 Challenges in forming dissimilar materials

The formability can be defined as the ability of the sheet metal to be formed into the required shape without failure. It is a process by which TB is brought to its final structural shape. The complexity of forming TBs made from dissimilar sheet materials arises from different microstructures, mechanical properties, deformation behavior and failure mechanisms as well as from different thicknesses of the two parent materials. In addition, different weld regions within a single weld can arise from the chosen welding process such as base metal (BM), fusion zone (FZ) and heat affected zone (HAZ) each with its characteristic size, microstructure and mechanical properties, and deformation behavior. This also means that different formability can exist in the TB under the same forming conditions depending upon the heterogeneity of the weld, i.e., the material of the blanks is no longer uniform. Further, the quality of weldment and weldment orientation plays a crucial role in forming of TBs (Omar, 2011; Kinsey and Wu, 2011).

Formability is neither a material property nor a process property but it is a system property (Omar, 2011). It is not only affected by sheet metal properties but also by the process conditions. Hence, to obtain a successful performance of the stamped components after forming process of TBs of dissimilar materials, many important considerations should be taken into account during both welding and subsequent forming process due to the non-uniform distribution of the mechanical properties within the blanks.

1.3 Research scope

1.3.1 Motivations

Increasingly stringent safety and emissions laws have led to the need for increasing the usage of higher strength metals (e.g., AHSS) as well as lightweight metals (e.g., aluminum alloys). The recent report from Ducker Worldwide (2014) showed that, by the year 2025 in North America, the percentage of using AHSS and aluminum sheets in the production of car body structure with closure parts for lightweight vehicles will be increased to 40% and 16% respectively, at the expense of lower strength grades (see the pie chart in Figure 1.4). However, technical problems are often encountered in formability of TBs especially when AHSS and aluminum sheets are incorporated. These include premature weld failures due to the presence of softening zone (as in TWBs from AHSS), and brazed interface failure due to insufficient bonding and wetting (as in TBBs made from steel and aluminum). Additionally, there is non-uniform deformation and weld line movement, which are the common phenomena during plastic deformation and forming of TBs with different thickness and/or strength of base sheet materials where the thicker or the stronger sheet in the TB tends to resist deformation, while the thinner or the weaker sheet dominates the majority of deformation.

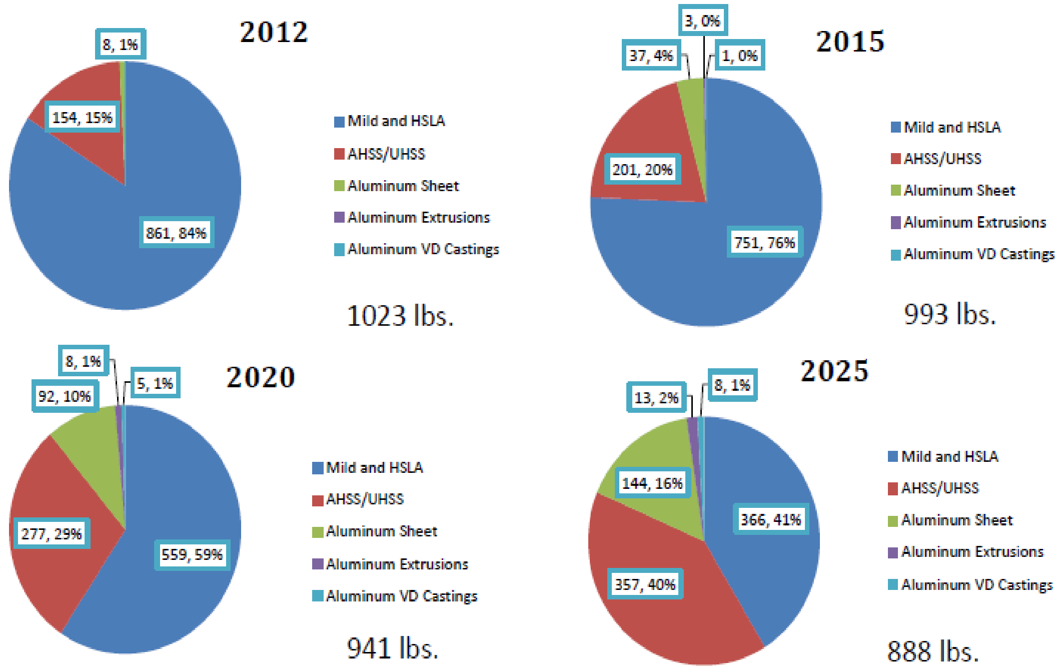

Figure 1.4. The growth of materials usage in production of car body structure with closure for lightweight vehicles (Ducker Worldwide, 2014).

There have been many advances in welding process technology which can enable manufacturers to precisely control welding parameters including the heat input during welding so as to obtain a sound and high quality weldment with limited distortions to the base metals. In particular, high power defocused fiber laser welding, and Laser/MIG hybrid and cold metal transfer (CMT) brazing, which are relatively new welding techniques, are now available for producing TBs. These methods were used in the current research to produce steel-to-steel TWBs and steel-to-aluminum TBBs respectively. In addition, there are no suitable formability tests in the literature that work well with TWBs of different thicknesses and/or strengths. With regard to TBBs, there is virtually no published literature that provides a fundamental understanding of the local deformation behavior at the brazed steel/aluminum interface of butt-joint configurations. These areas of forming of TBs need to be scientifically studied to advance the use of dissimilar materials. Developing a robust forming process for very dissimilar TBs components requires a new and more fundamental understanding of material flow and formability in these materials.

1.3.2 Thesis objectives

The main objective of the current research is to study the correlation between parent material properties, welding/brazing process parameters, weld microstructure and formability of the produced TWBs and TBBs. The TWBs are made from steel sheets of different thicknesses and/or strengths combinations such as dual phase (DP) steel (an advanced high strength steel) and a high strength low alloy steel (HSLA). The TBBs, are made from dual phase (DP) steel and AA2024-T3 aluminum sheets. After surpassing the initial challenges of obtaining sufficient amount of sound TWBs and TBBs from well-established and optimized high power defocused fiber laser welding, and Laser/MIG hybrid and CMT brazing methods respectively, the forming phase of the research was initiated.

For steel-to-steel TWBs, the first and the foremost issue is the formability of TWBs made by defocused fiber laser welding process and utilize base materials of same thickness as well as different thicknesses and/or strengths. With regard to TBBs, a fundamental understanding of the local deformation behavior at the brazed steel/aluminum interface is addressed by conducting specialized miniature mechanical tests that focus on continuous observation of the brazed region under a high magnification optical microscope. Such tests are utilized in an attempt to relate brazed joint characteristics and properties to flow and fracture characteristics of TBBs.

The main objectives of the current thesis are divided into the following sub-objectives:

i. Assessment of the formability of defocused fiber laser welded steel blanks made from advanced high strength steel (such as DP780 steel) using conventional hemispherical punch test:

The effect of defocused fiber laser welding technique on formability, weld quality and failure characteristics of the produced TWBs is analyzed and compared with that of parent sheet materials. The defocused fiber laser welding method is expected to decrease the amount of heat input during welding and consequently reduce the distortion of the base metal. Therefore, problems such as the premature failure during forming due to base metal distortion (or softening phenomenon) could be minimized which in turn could enhance formability of the TWBs.

ii. Development of a new method of formability testing of welded steel blanks of dissimilar thickness and/or strength combinations:

The non-uniform deformation and weld line movement are common problems during the deformation of TWBs of different thicknesses and/or strength. The origins of such problems lie in the differential stretch-draw characteristics of the base sheets that are welded, and the heterogeneity in plastic deformation achieved in the two base sheets during forming due to the difference in thickness and/or strength of the base metals. The non-uniform deformation and weld line movement make it difficult to assess intrinsic formability of the weld in comparison to the parent material. Therefore, a new test for TWBs formability assessment, referred to as double-layer test, has been developed and assessed for minimizing weld line movement during stretch forming without modifying the basic test methodology. The double-layer formability test method is applied to both in-plane and out-of-plane stretch forming process of TWBs made from different thicknesses and/or strengths of parent material combinations.

iii. Assessment of the plastic flow across brazed interface, interface strength, and limiting strains in steel-to-aluminum TBBs made by Laser/MIG hybrid and CMT brazing methods under uniaxial strain paths:
Uniaxial miniature tensile tests were carried out to assess uniaxial tensile ductility of steel-to-aluminum brazed joints made from Laser/MIG hybrid and CMT brazing methods. The current study is from the point of view of brazed interface metallurgical characteristics, load transfer across brazed interface, as well as development of local plastic strain field during plastic deformation of the brazed joint. Additionally, if the brazed joint strength can be improved in brazing trials, what level of forming can be achieved without failure of the brazed joint?

1.3.3 Expected research contributions

The main expected contributions of this research can be summarized as follows:

- Study the effect of using defocused fiber laser beam welding on the formability of TWBs incorporating DP steel in different out-of plane strain paths using hemispherical punch test. The fundamental understanding of formability of TWBs produced by such welding technique in out-of plane test mode is still lacking in literature and requires further investigation.

- The double-layer formability test is a new method of formability in which weld line stays in position with respect to forming tools and is subjected to the same stress and strain state as the parent material in the weld and its vicinity. Therefore, the quality and characteristics of weld zone could be checked and identified. This test is much simpler, versatile in terms of a range of gauge combinations, and more effective than other available techniques such as variable blank holder force (which needs special and complicated forming die design). It also does not utilize shims to compensate for thickness differential (which initiate fracture in the thin gauge metal at the shim boundary (Jain, 2000)), or a stepped die where stress concentration occurs if the upper or lower die is not slackened enough (Narasimhan and Narayanan, 2011), as discussed later in this thesis. The proposed double-layer test is relatively new and its applicability and dependability are needed to be further investigated and compared with conventional single-layer forming method for steel TWBs made from base sheet of different thicknesses and/or strengths to isolate the advantages, if any, of the proposed double layer method.

- Investigation of butt joint configurations of steel-to-aluminum TBBs made by a relatively new processes of Laser/MIG hybrid and CMT brazing. Fundamental deformation studies related to these two brazing methods for joining steel-to-aluminum to create TBBs are lacking. In addition, most studies on brazing of steel-to-aluminum sheet materials to create TBBs in the literature are focused on the effect of brazing parameters on formation of intermetallic compounds (IMCs) layer and its thickness and subsequent effect of layer thickness on the joint strength (i.e., from metallurgical point of view). The present research has a different focus from the published work in that it involves understanding of plastic deformation (general ductility), load transfer across brazed interface as well as local deformation and damage initiation in the brazed interface region.

1.4 Thesis outline

Thesis is arranged in six chapters as follows. A general introduction to the topics of welded and brazed sheet materials in the form of TBs was provided in Chapter 1. The chapter identified the need and challenges encountered during joining and subsequent forming processes of TBs, then the scope and objectives of the present work were stated. Chapter 2 presents a brief review of relevant literature in the light of thesis objectives. The knowledge gaps in the literature related to the proposed general topic are identified towards the end of this chapter. A research plan and experimental methodology to carry out this plan are presented in Chapters 3 and 4 respectively. Chapter 5 presents the results obtained and relevant discussion pertaining to the proposed objectives. Chapter 6 draws conclusions and suggests possible directions for future work.

Chapter 2

Literature Review

The complexity of dissimilar materials joining and subsequent forming processes makes them an area of research interest for scientists and engineers. Also, recent developments in welding and brazing technologies for joining offer many opportunities in automotive manufacturing toward material optimization and cost reduction. A similar trend can be observed in the development of automotive forming technologies.

In the following, literature of materials utilized in TBs in the present research as well as literature related to laser welding and brazing methods are overviewed. Subsequently, a review of work done in the area of joining and subsequent forming of dissimilar materials (steel-to-steel and steel-to-aluminum configurations), is presented.

2.1 Materials

The focus of the present work is on advanced high strength steels (AHSS), conventional high strength low alloy steel (HSLA) and aluminum alloys. These materials are discussed in the following subsections.

2.1.1 Advanced high strength steel (AHSS)

AHSS are multiphase steels that contain different concentrations of ferrite, bainite, martensite and retained austenite phases. The amount of these phases and their morphologies offer a range of desirable functional characteristics in steels (Bhattacharya, 2011; Davies, 2012). These steels offer particular microstructures to achieve strength and ductility combinations that were never before obtained (WorldAutoSteel, 2014). In addition, these steels have good ductility, high tensile properties, high work-hardening coefficient, as well as capacity for high energy absorption during crash. These exclusive combinations enabled auto designers to introduced these steels in critical automotive structural parts such as A, B and C pillars, the roof rails and bow, cross-members, door beams, front and side members, and as bumper reinforcement. They also are extensively used in internal panels made of tailor welded blanks (Shome and Tumuluru, 2015).

AHSS family for automotive application include dual-phase (DP) steel, transformation induced plasticity (TRIP) steel, complex-phase steel (CP), martensitic steel (MS), and twinning induced plasticity (TWIP) steel. They are characterized by yield strengths and ultimate tensile strengths higher than 300 and 600 MPa respectively (Bhadeshia and Honeycombe, 2006). Among all AHSS, DP and TRIP steels have been identified as potential candidates for car body fabrication because of their low manufacturing cost compared to TWIP steel and their better formability compared to MS steel (Nayak *et al.*, 2015). The present research is mainly focused on DP steels.

Dual phase steel, is made up of a continuous soft ferritic matrix reinforced with hard martensite islands (see Figure 2.1). The martensite islands are produced by a short annealing time to the intercritical (ferrite and austenite) region followed by rapid quenching to transform the austenite to martensite while the existing ferrite remains.

Thus, the DP steels have a good combination of ductility offered by soft ferrite phase and high strength depending on the volume fraction of martensite. As the volume fraction of martensite increases, the tensile strength of DP steels increases (see Figure 2.2). The common DP grades designed for the automotive industry range from DP500 to DP1000. However, DP600 and DP780/800 are more widely used (Hilditch *et al.*, 2015).

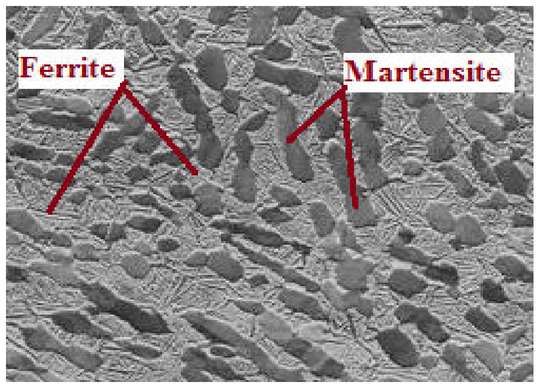

Figure 2.1. Micrograph of DP steels (WorldAutoSteel, 2014).

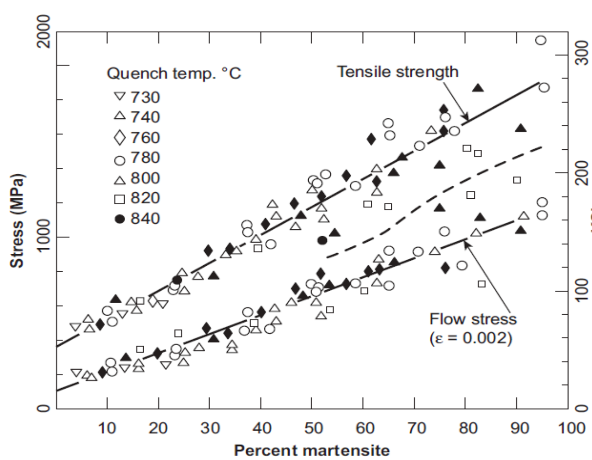

Figure 2.2. Effect of martensite volume on both the yield and tensile strength of dual-phase steel (Davies, 1978).

The ductility of the DP steel makes it good for forming, while the strength is required to maintain structural integrity and enhance crash performance. This uniqueness in DP steel lies in its material flow behavior, relatively high work-hardening coefficients n and K, and plastic anisotropy parameters, R values. Therefore, based on these properties, forming complex shapes with these high strength steel is possible (Bleck, 1996; WorldAutoSteel, 2014).

2.1.2 High strength low alloy steel (HSLA)

Micro-alloyed steels or high strength low alloy steel (HSLA), are a hybrid between plain carbon steels and alloy steels (see Figure 2.3). They have yield strengths of 275 to 550 MPa and tensile strengths of 415 to 690 MPa. The higher strengths are achieved due to the presence of small amounts of alloying elements such as niobium, titanium, and/or vanadium in the order of about 0.1 wt% of each micro-alloying element. The carbon content in HSLA steels is restricted in the range of 0.05 to 0.25%C in order to produce adequate formability and weldability (Davis, 2001; Campbell, 2008).

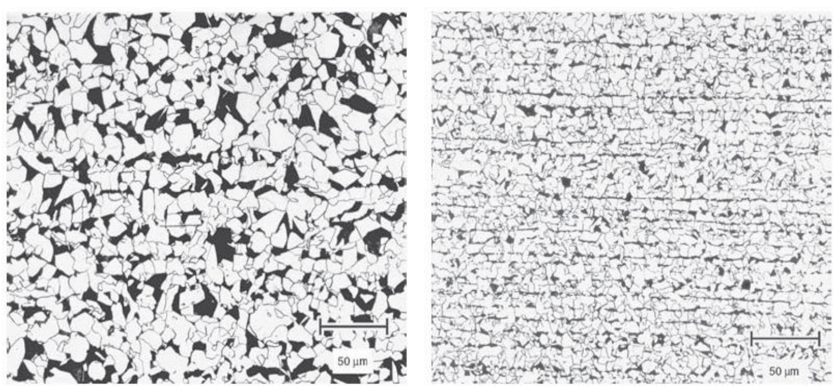

Figure 2.3. The microstructure of plain carbon steel (left), and HSLA (right) (Campbell, 2008).

Solid-solution hardening, precipitation hardening, and fine ferrite grain size are the main factors responsible for the increased strength of HSLA steels, with a fine ferrite size being the most important (ArcelorMittal, 2015a; Campbell, 2008).

The most important factor in HSLA steel selection process beside formability and weldability is the favorable strength-to-weight ratio compared to the conventional low-carbon steels. This characteristic has led to their increased use in automobile components such as suspension systems, energy-absorbing bumper assemblies and for increasing fuel economy through thinner and lighter-weight chassis sections (Davis, 2001).

2.1.3 Aluminum alloys

Aluminum is a lightweight metal with a density of 2.70 g/cm^3 and a moderately low melting point of 655^{o}C. It has a good formability due to its face-centered cubic crystalline structure nature and rather low work-hardening rate (Campbell, 2008). The strength of aluminum can be increased by alloying it with manganese, silicon, copper, magnesium, zinc, etc. Therefore, aluminum grades are identified based on the alloying element and heat treatment, using a four digit representation, from 1XXX to 8XXX. The 5XXX and 6XXX series of aluminum have yield strengths equivalent to mild steel and 7XXX series yield strengths are equivalent to high strength steels (AluMatter, 2010).

Aluminum alloys are widely used in consumer products such as foil, beverage cans, cooking utensils, architectural and electrical applications, and structures for boats, aircraft, and other transportation vehicles (Campbell, 2008). This wide range of applications is possible due to properties such as superior corrosion resistance, natural and chemical inertness, recyclability and good workability. Aluminum alloys also have high thermal and electrical conductivities, high strength-to-weight ratio, fracture toughness, energy absorption capacity and fatigue strength. It does not oxidize progressively because of a hard, microscopic oxide coating that forms on the surface and protects the metal from corrosive environments (Padmanabhan *et al.*, 2011). The major growth of aluminum use in future automobiles is expected to be in the body structures and body panels, such as front rails, roof rails, hoods, deck lids and fenders (Mallick, 2010).

2.2 Welding processes

Welding is defined as the process in which joining occurs between materials of the same basic type or class through formation of atomic, ionic, or molecular-level bonds under the application of heat and/or pressure (Messler, 2004). It is considered as the most functional, versatile and realistic joining method applicable in every industrial field. The choice of welding technique depends on application, design considerations and the scale of structures to be created by welding. Over the years, the use of nonconventional welding methods and techniques such as laser welding, hybrid welding and advanced MIG brazing for tailor blanks has grown steadily. Laser welding, hybrid welding, and cold metal transfer (CMT) have been shown to have numerous advantages over conventional arc welding.

2.2.1 Laser welding

Laser beam welding (LBW) is a fusion welding process where radiant energy of a concentrated coherent light beam is used to produce the heat required to melt the materials to be joined (Messler, 2004). The work pieces' surfaces absorb energy from the focused high irradiance laser beam at the impingement point in the form of heat till the materials reach their melting points to create weld pool (weld bead) at the overlapping workpiece surfaces resulting in fusion welding (Ion, 2005).

According to power density of the laser beam (power per unit area of the joint surface), fusion welding takes place through one of two different welding modes; conduction mode or melt-in mode, and deep penetration mode or keyhole mode (Kannatey-Asibu, 2009) (see Figure 2.4).

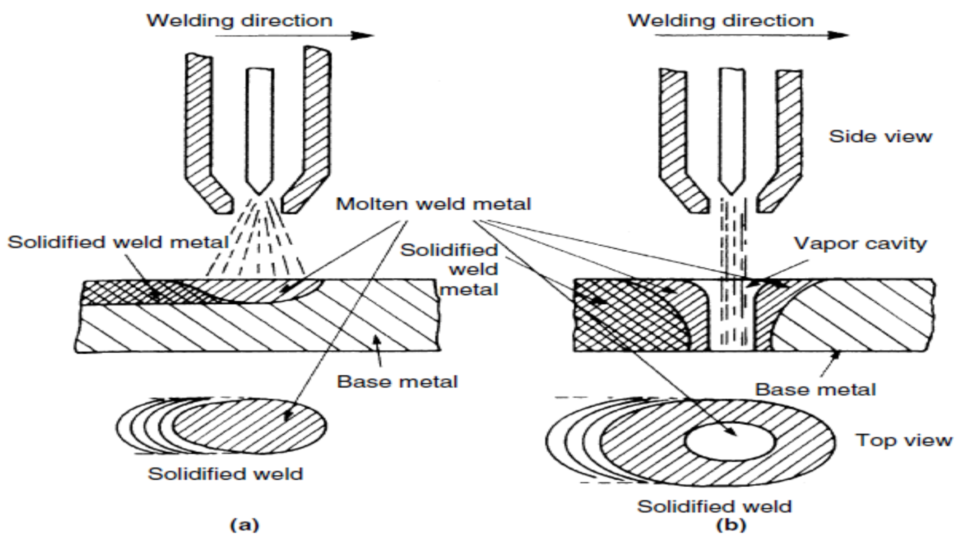

Figure 2.4. Schematic illustration of welding modes (a) conduction mode, and (b) keyhole mode (Messler, 2004).

Conduction welding mode is associated with low energy density of the spot (usually lower than 1 MW/cm^2). The material surface absorbs energy from laser beam and then transfers energy to the surrounding material by conduction. The weld bead in conduction laser welding is characterized by a low depth to width ratio (3:1), which is required in applications with limited penetration conditions (Vaamonde and Vázquez, 2012).

In keyhole welding mode, the beam is focused on the material surfaces to generate a high energy density of the spot (usually higher than 1 MW/cm^2). A part of the material at the impingement point is vaporized to form a narrow and deep vapor cavity (the keyhole) which is surrounded by molten metal. Melting takes place at the leading edge of the cavity and solidification occurs at the rear. The molten material around the keyhole fills the cavity as the beam is traversed along the joint. The steady state of the keyhole is achieved by the equilibrium between forces (hydrostatic pressure, hydrodynamic pressure, and surface tension) that tend to collapse the cavity of molten metal, and the opening forces arising from material ablation pressure and vapor pressure. The maximum and minimum welding speed is required to keep this balance as an adequate amount of vapor pressure is maintained to prevent collapse of the cavity. As steady state is achieved, a narrow weld bead is obtained which is characterized by a high depth to width ratio (10:1). Keyhole is the most used laser welding mode and is excellent for welding applications requiring deep penetration (Vaamonde and Vázquez, 2012; Cretteur, 2015).

Since the development of the first ruby laser in 1960 (Maiman, 1960), various types of lasers have been developed. Each one has different specifications depending on the physical nature of the active medium used for laser action. Here, we will focus only on types of laser that are used in industrial welding processes.

2.2.1.1 Gas lasers

As the name implies, the active medium in these laser systems is gas. It is considered as the most common form of laser used in industry due to relatively lower cost of active medium (gas). However, due to low densities of gases, a large volume of gas is required to obtain a significant laser. Hence, gas lasers machines are usually relatively larger than the solid-state ones. The common examples are the He-Ne and CO_2 lasers (Kannatey-Asibu, 2009).

CO_2 laser is most commonly used in machining of materials. The practical CO_2 lasers consist of CO_2 gas as its active medium mixed with nitrogen and helium to increase the power. It emits well collimated beam of a few millimeters in diameter at a wavelength of 10.6 µm in power range of 1.5∽6 kW. The energy absorption of the laser beam by most metals is low due to its wavelength, with an overall efficiency of up to 20% (Moreira *et al.*, 2012). The downsides of CO_2 lasers are its complex optical system which consists of mirrors and lenses, and the light cannot be transmitted via optical fiber due to its wavelength. CO_2 lasers are used for sheet welding at high welding speeds with a good beam quality (Kannatey-Asibu, 2009).

2.2.1.2 High power semiconductors (diode) lasers

The active medium is semiconductor materials which are based on radiative recombination of charge carriers. Currently available diode lasers for industrial application have power range up to 2.5 kW with average wavelength of 0.808 µm (Kannatey-Asibu, 2009). Diode lasers have the advantage of being relatively lower weight and compact in size which make them easy to fabricate by mass production with lower cost when compared to CO_2 or Nd:YAG lasers. They also have lower cooling requirements, higher lifetime, higher efficiencies of up to 50% and higher absorption coefficient for many metallic materials used in industry. However, they have lower beam quality and lower power compared to the CO_2 and Nd:YAG lasers. Therefore, they are limited to conduction mode only due to the relatively low power densities. Further improvements are needed to enhance their capability for deep penetration welding. Also, special optics are required to transform the beam from the linear emission of laser bars (rectangular or square shape) to a round shape for transmission via optical fiber. Diode lasers are used for surface treatment and welding of plastics. They are also used in pumping of solid-state lasers to increase efficiency (Kannatey-Asibu, 2009; Moreira *et al.*, 2012).

2.2.1.3 Solid-state lasers

In solid-state lasers, the active medium consists of an insulating crystal or glass containing small impurity ions. Most solid-state lasers generate pulsed beams, even though some generate continuous ones. The most common types of solid-state lasers include ruby, Nd:YAG, and Nd:Glass lasers. Among these, Nd:YAG laser is the most commonly used one in industrial applications (Kannatey-Asibu, 2009).

Nd:YAG Laser uses Neodymium Yttrium Aluminum Garnet crystal as active medium. The operation of the Nd:YAG laser can be continuous (CW) or pulsed (PW). The efficiency of both modes ranges between 1∽3%. The power output in continuous mode varies from 0.15∽6 kW; the very high powers (6 kW) are obtained by pumping with a diode laser with possibility of lasing several wavelengths up to 1.064 µm. Applications of Nd:YAG lasers include laser surgery and materials processing (welding, cutting, drilling, and surface modification). The beam can be guided through flexible glass fibers, due to its smaller wavelength. This makes it attractive for 3D operations combined with articulated arm type robots, providing greater flexibility, accessibility and lower costs (Kannatey-Asibu, 2009; Moreira *et al.*, 2012).

2.2.1.4 Fiber lasers

Fiber lasers utilize an optical fiber with a core that is doped with a rare earth element such as erbium (Er), neodymium (Nd), and ytterbium (Yb) as the active medium and the pumping is done using a diode laser. The laser beam is emitted longitudinally along the fiber with output power typically up to hundreds of watts. These systems are then bundled together to provide higher powers (Moreira *et al.*, 2012).

High power fiber lasers have multiple advantages including; very compact design, competitive cost and relatively high output efficiency compared to CO_2 and Nd:YAG lasers, high beam quality with small beam focus diameter; and a robust setup for mobile applications. In addition, using fiber laser in welding process offers higher welding speed and lower energy consumption which make it an attractive option for industrial applications (Kannatey-Asibu, 2009).

2.2.2 Hybrid welding

Hybrid Laser Arc Welding (HLAW) is a joining process that simultaneously combines laser welding and arc in the same weld pool. In general, the beam from any welding laser source (CO_2, Nd:YAG, Diode, Fiber etc.) can be combined with any arc process (MIG, TIG, plasma etc.). However, hybrid laser/MIG and laser/TIG welding are the most common process combinations (Olsen, 2009). Figure 2.5 illustrates the process of laser/MIG hybrid welding.

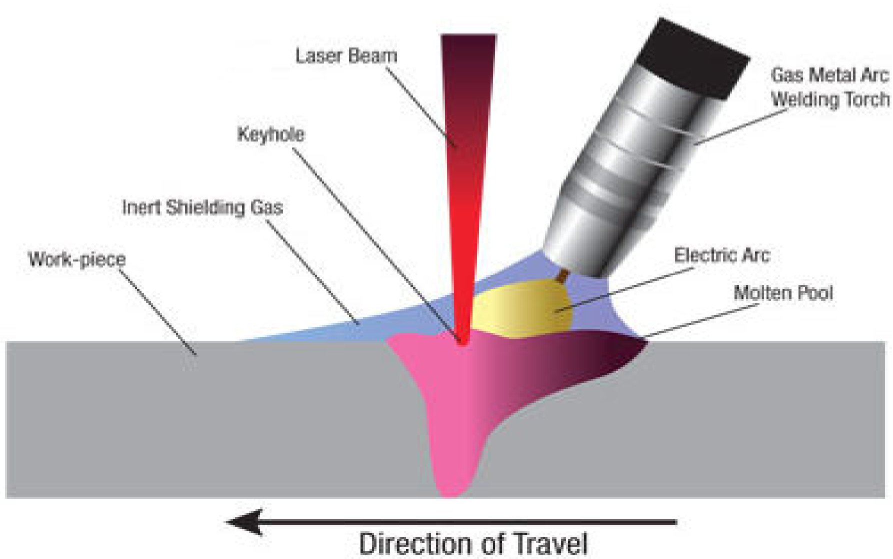

Figure 2.5. Schematic illustration of Laser/MIG hybrid welding process. [Source: Lincoln Electric (2016)].

Laser welding as a joining technology provides high precision, high performance, high speed, good flexibility, high quality, low distortion and full automation welding process. However, high costs of laser apparatuses, small fit-up gap tolerance, easy formation of welding defects such as porosity in fusion zones, and difficult melting of highly reflective or highly thermal-conductive metals such as aluminum, represent the main drawbacks of laser welding. Arc welding is most common and widely used in welding because of lower cost of the machines and ease of operation. However, its limitations are slower welding speeds, shallow penetration of weld beads, and formation of humping beads in high speed welding (Katayama, 2009).

Hybrid laser/MIG welding process, as the most common combinations, can compensate the weaknesses of laser welding and MIG welding by utilizing the individual strengths of both welding processes. Such a process can yield higher welding speeds and consequently lower heat input and less distortion, deeper penetration, and wider gap tolerance. Also, the process can result in considerable reduction of costs of edge preparation as well as weld defect formation. Further, the hybrid process produces welds which are more ductile than welds produced by laser welding only (Katayama, 2009). Lastly, the use of filler material can alienate both geometrical and metallurgical variability issues. A better weld bead surface appearance can be achieved in addition to the compensation of the losses caused by burning of alloying elements, mainly those with low vaporisation temperature, (Quintino *et al.*, 2012).

2.2.3 Cold metal transfer brazing (CMT)

The cold metal transfer (or CMT) is derived from the well-known conventional MIG/GMAW welding process. This technique was invented by Fronius International

GmbH, Austria, in year 2005, and was introduced as a means to join aluminum to galvanized steel (Agudo *et al.*, 2008). The CMT welding technique, when compared with conventional MIG/GMAW welding process, is considered a cold process as the work-pieces to be joined remain colder. The main feature of this technique involves the full digital control of wire motion (filler wire feed rate) using micro-controller and feed motor. In addition, the wire metal transfers to the weld pool without applying current or voltage (off-circuit metal transfer). As a result, the heat input can be minimized, and consequently reducing the thickness of the intermetallic compounds or IMC layer, and thereby improving the mechanical properties of the brazed joints. Moreover, the controlled wire movement and precise wire metal transfer (droplets detachment) results in clean and spatter-free welded surface.

The CMT process operates in a short-circuit mode of controlled pulsed current and voltage through the welding cycle. In the beginning arcing occurs by supplying a high pulse of current between filler wire (electrode) and the substrate, which causes melting of the wire tip. Then, the wire dips into the weld pool bringing a short-circuit formation. Thereafter, the current is reduced and the arcing is extinguished. During the short-circuit, the wire is then retracted to the torch leading to the detachment of the molten droplet and hence, the metal transfer occurs at lower current (i.e., minimum heat input). The filler wire then moves forward again and the cycle is repeated. The CMT welding cycle steps are depicted in Figure 2.6.

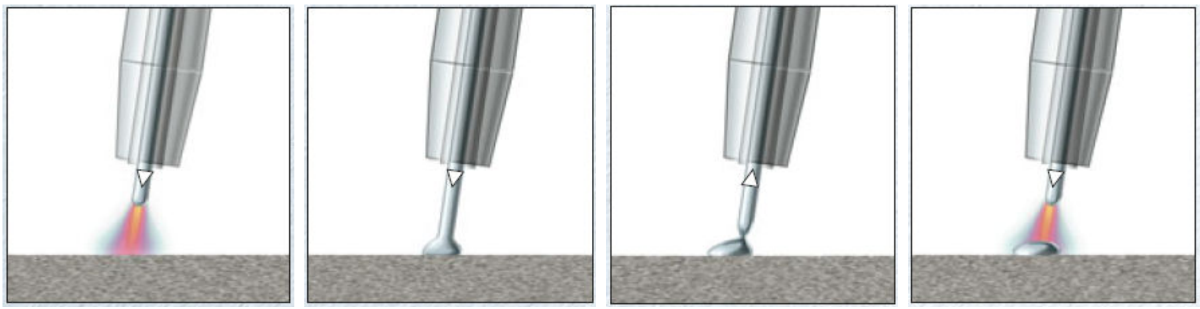

(a) Step1: arcing (b) Step2: dipping (c) Step3: detachment (d) Step4: arcing

Figure 2.6. Schematic drawing of the cycle steps of CMT brazing method. (Source: Fronius (2015)).

2.3 Effect of welding/brazing on the microstructure

2.3.1 Steel microstructure

Due to the higher heating and cooling rates that are associated with laser welding, microstructure transformation kinetics take place under non-equilibrium conditions (Ion, 2005). The development of microstructure transformation under non-equilibrium conditions is mostly presented in the form of continuous cooling transformation (CCT) diagram. Figure 2.7 depicts the CCT diagram of hypoeutectoid steel with the effect of different cooling rates on the microstructural products formed from austenite decomposition. The microstructure transformation mostly depends on the cooling rate, chemical composition, temperature gradient and different alloying elements (Kou, 2003; Ion, 2005). During laser welding, cooling rate increases resulting in formation of hard metastable phases such as martensite.

After welding process, the volume fraction of the newly formed phases and the extension microstructure transformation zones (welding zones) and consequently the mechanical properties of the steel welded blanks are controlled by the welding parameters and the chemical composition of steel sheets (Kou, 2003). Figure 2.8 shows the different welding zones within the microstructure where transformation occurs according to the maximum temperature reached locally. Based on the newly formed microstructures, welding zones are classified to three main zones; fusion zone (FZ), heat affected zone (HAZ), and unaffected base metal (BM) (Kou, 2003).

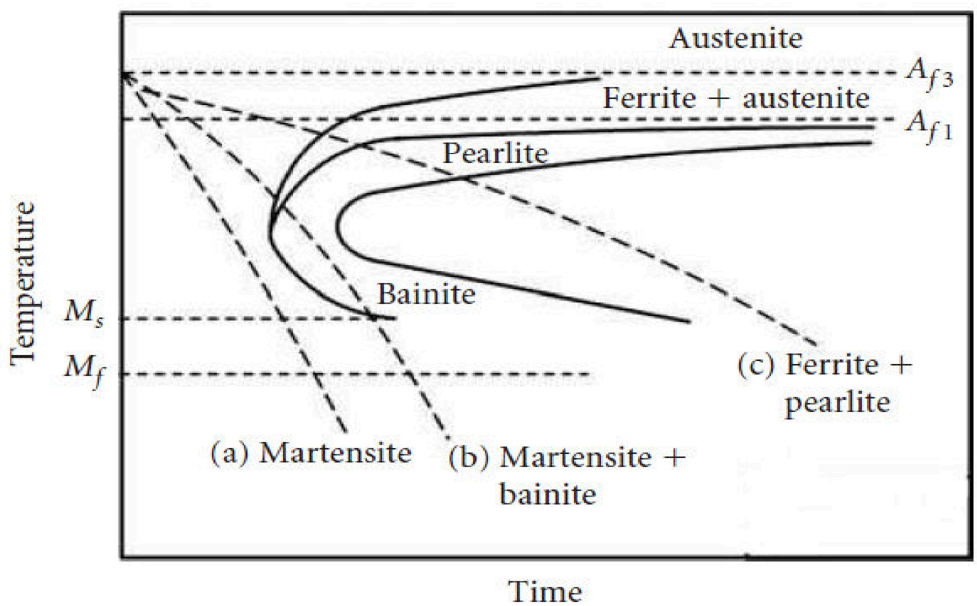

Figure 2.7. Continuous cooling transformation (CCT) diagram for hypoeutectoid steel with different cooling rates (Ion, 2005).

The FZ has the highest local peak temperature and the metal is melted during the welding process at the impingement point then undergoes solidification. For laser welding, the width of FZ is relatively narrow and it has very high hardness compared with the unaffected base material. The higher cooling rate results in formation of hard martensite phase. Therefore, steel welded blanks show higher strength after welding.

The hardenability of this zone increases with the increase of carbon content (Nayak *et al.*, 2015). Moreover, hardness values of FZ alter according to the chemical composition of steel sheets, e.g., existence of martensite phase in the parent metals such as AHSS increases the volume fraction of martensite within the FZ after welding and consequently increases the hardness values in this zone (Cretteur, 2015).

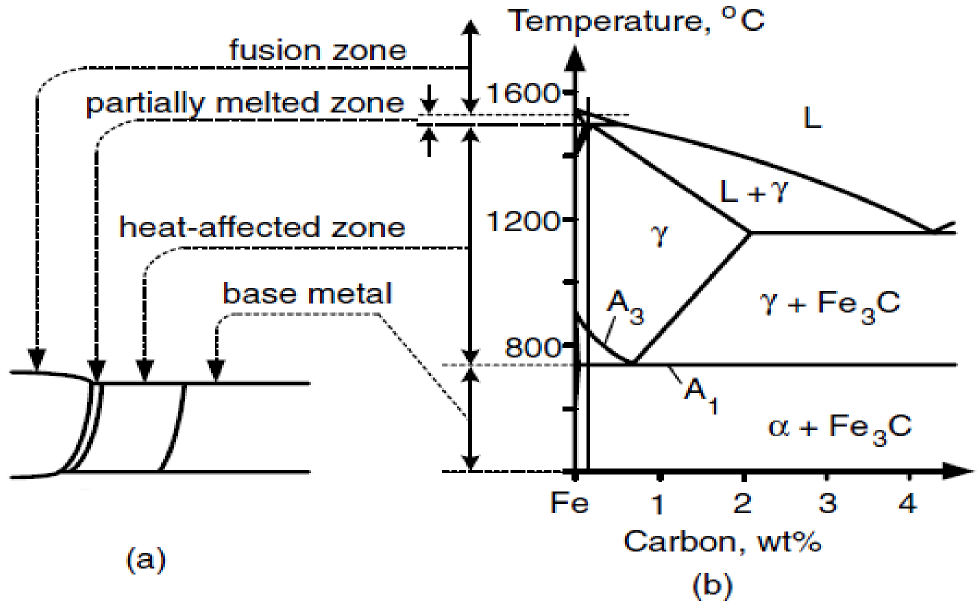

Figure 2.8. Correlation between transformation temperature distribution in different welding zones and Fe-C phase diagram (Kou, 2003).

No metal melting occurs outside of the FZ boundaries. However, the peak temperature during welding still high enough for the material to undergo solid-state metallurgical transformation in HAZ (Kou, 2003; Nayak *et al.*, 2015). Heat transfer occurs from the weld pool towards the colder base material by conduction. The maximum temperature reached locally decreases with increasing distance from FZ (see Figure 2.9). According to this temperature with respect to the critical temperatures Ac_1 and Ac_3, HAZ is divided into three subregions, supercritical, intercritical and subcritical. The supercritical HAZ, occurs closest to FZ, where the steel is heated above its Ac_3 temperature to form austenite then it transforms to martensite during cooling. Intercritical HAZ occurs adjacent to supercritical HAZ, where the peak temperature during welding is between the Ac_1 and Ac_3 temperatures of the steel and the microstructure partially transforms to austenite. Then, it transforms into martensite during cooling and the ferrite remains unchanged. Subcritical HAZ occurs in the outskirt of unaffected BM, where the peak temperature during welding is below the Ac_1 temperature of the steel, and the base material is tempered (Nayak *et al.*, 2015). Hardness drop below that of BM can be obtained within this subregion due to tempering of the martensite phase of BM.

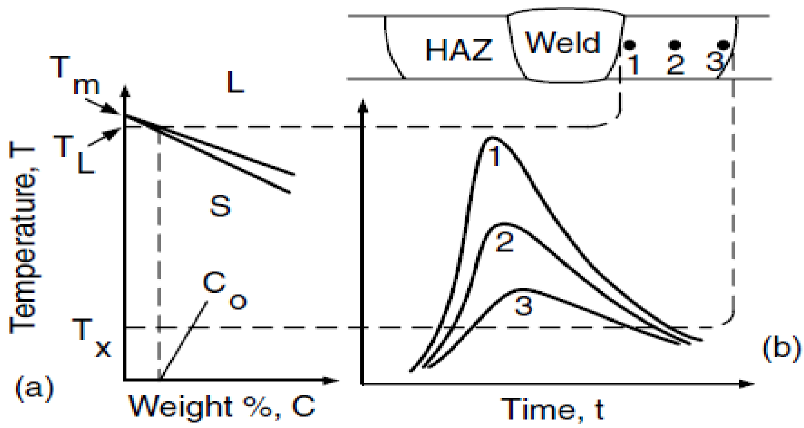

Figure 2.9. Temperature distribution within HAZ (Kou, 2003).

2.3.2 Aluminum microstructure

Unlike steel sheets, the wrought aluminum alloys show lower strength in FZ (or weld seam) after welding/brazing because their microstructure is changed to cast structure with coarse grains (see Figure 2.10). The high temperatures during welding/brazing result in grain growth which degrades the strength of the material in FZ (or weld seam) (Kannatey-Asibu, 2009; Merklein *et al.*, 2014). The chemical composition does not alter in this region, however, the loss of alloying elements with low melting point, mainly magnesium, may cause reduction in strength of aluminum TBs (Mathers, 2002; Ion, 2005). Using filler wire can compensate for the lost of alloying elements but porosity levels tend to increase because of contamination from the wire (Duley, 1999). In HAZ, for non-heat-treatable aluminum alloys, loss of strength occurs due to recrystallization which takes place when the local temperatures exceed 200^{o}C in HAZ. For heat-treatable aluminum alloys, loss of strength occurs due to dissolution of the precipitates in 2XXX alloys, and overageing of the precipitates in 6XXX and 7XXX alloys (Mathers, 2002) (see Figure 2.11).

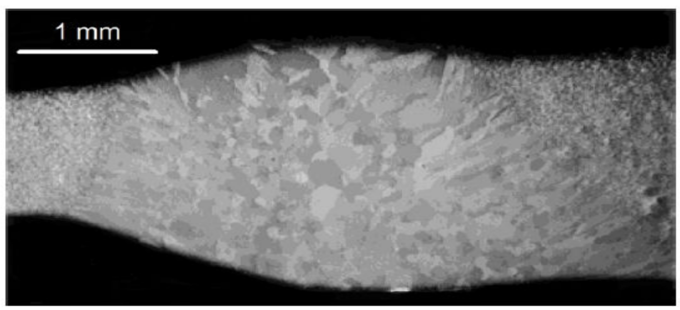

Figure 2.10. Microstructure of FZ (or weld seam) in aluminum after welding process (Merklein *et al.*, 2014).

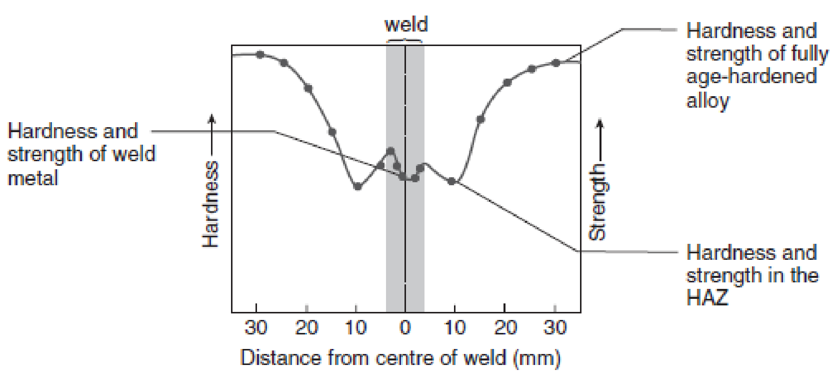

Figure 2.11. Effect of welding on heat-treatable aluminum alloys (example of AA6061-T6 welded blank) [Source: Mathers (2002)].

2.4 Steel-to-steel TWBs

2.4.1 Welding

Intuitively, welding different steel sheets to each other is not considered as a challenging process because they are classified as slightly dissimilar materials, i.e., there is not much discrepancy in both physical and chemical properties between them. However, for TWBs, the requirements of precise joint fit-up and alignment of the workpieces are more stringent especially for laser butt-joining. The problem is compounded by the narrow beam size of laser compared with other fusion welding processes (Shome and Tumuluru, 2015). Any gap between sheets in a butt-joint may cause defects such as weld concavity and undercut, which degrade TWB formability. Moreover, any instability in the keyhole mode of welding, which is predominantly used in industrial laser welding process, often leads to rough and ropy bead surfaces (Nayak *et al.*, 2015).

In the present work, welding of advanced high strength steel (AHSS) mainly dual phase (DP steel) and high strength low alloy steel (HSLA) is considered. However, the two materials have different microstructures and each follows different metallurgical behavior during welding. DP steel consists of continuous soft ferritic matrix reinforced with hard martensite islands. The high strength of DP steel depends primarily on the volume fraction of martensite phase. As the volume fraction of martensite increases, the tensile strength of DP steels increases (Hilditch *et al.*, 2015; WorldAutoSteel, 2014). Conversely, HSLA is a single-phase ferritic steel reinforced with precipitation of small amounts of alloying elements and strengthened by grain size refinement (ArcelorMittal, 2015a; Campbell, 2008). As shown below in Figure 2.12, TWBs from same parent AHSS materials (such as a DP-to-DP combination) exhibit increase in hardness in the weld region but rapid softening in the heat affected zone (HAZ) adjacent to it (Li *et al.*, 2013;

Panda *et al.*, 2009; Xia *et al.*, 2007; Xu *et al.*, 2013). This softened region is caused by tempering of the martensite phase in DP steel, which reduces the hardness of this region during welding thermal cycle (Panda *et al.*, 2009). Nayak *et al.* (2015) found that softening increases as the volume fraction of martensite increases. Softening of the adjacent HAZ regions, and general heterogeneity of the microstructure, can play a critical role in early strain localization in such a region during forming of TWBs that incorporate advanced high strength steels and consequently reduce the ultimate strength of the weld. HSLA steels, on the other hand, do not suffer from any decrease in the hardness after welding, i.e., no softening occurs in the HAZ (Panda *et al.*, 2009; Xia *et al.*, 2007).

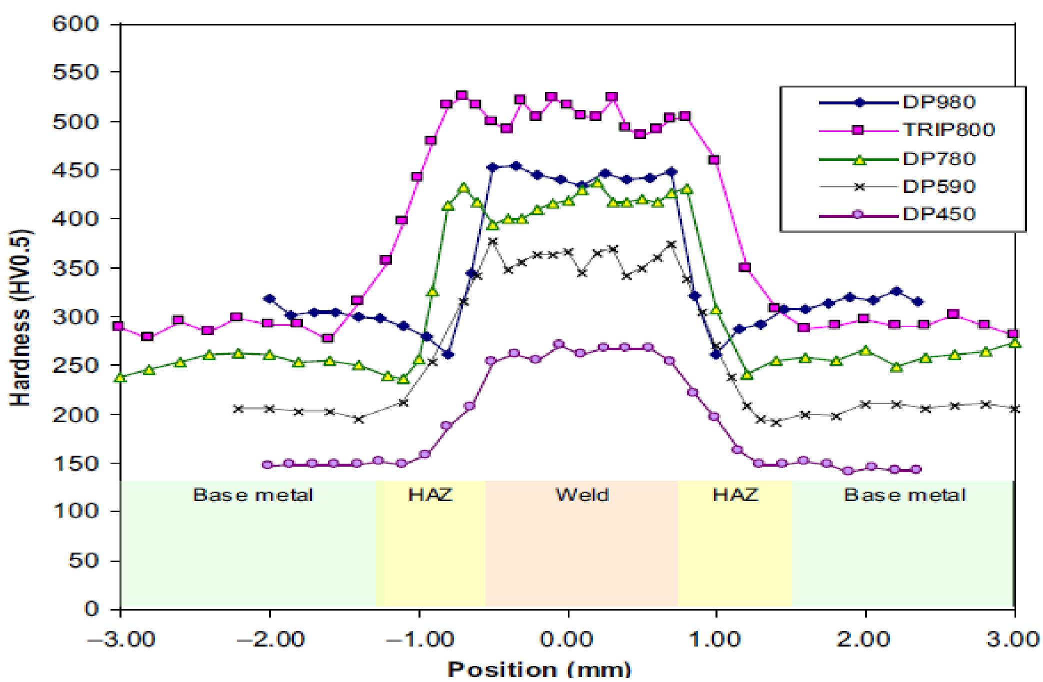

Figure 2.12. Effect of martensite volume fraction of AHSS on hardness profile (Cretteur, 2015).

The mechanical properties of steel-to-steel TWBs such as strength and ductility as well as the width of the welding zones depend on many parameters, namely material microstructure, welding method, weld line orientation, thickness ratio of the blanks and percentage of weld material in the cross-section of the specimen (Merklein *et al.*, 2014). Zadpoor *et al.* (2007) found that TWBs made from steel exhibit an increase in hardness in the weld region depending on the carbon content in the material and the welding method which leads to a cast structure with smaller grain sizes in the FZ than in the parent sheets. In laser welding, hardness in the FZ increases by at least 50% (Chan *et al.*, 2005). Nevertheless, a level of 120% increase is typical for most applications (Kang *et al.*, 2000). As a result of hardness increases of the produced TWBs, the yield strength and the ultimate tensile strength increase while the total elongation decreases (Abbasi *et al.*, 2012).

The formation of the weld is the result of the interaction of the beam with the metal. Therefore, both physical properties of the base metal and welding parameters significantly influence the laser welding process. A deep-penetration welding mode (keyhole), which is generally applied with TWBs laser welding process, may be formed using continuous and pulsed laser beams. Most laser applications in the industry today use continuous-wave lasers. Upon laser source, production issues such as the wavelength, choice of optics, shielding gases, potential use of optic fiber, safety issues and the basic thermal mechanisms, are determined (Duley, 1999; Cretteur, 2015). Indeed, as long as the keyhole welding mode is used, formation of the molten pool and consecutive metallurgical transformations are not significantly affected by the type of laser (Cretteur, 2015).

Generally, optimum welding parameters, which mostly lead to an acceptable level of mechanical properties and visually sound welds, are determined by a trial and error method where welding parameters are varied according to the kind of base materials being joined and its coating, melting and vaporization temperatures, as well as reflectivity and heat conductivity of the workpiece (Dawes, 1992; Duley, 1999). However, the main parameters that must be considered for laser welding are those which affect the amount of heat transferred to the work piece such as the materials involved, power intensity and the interaction time given for the material to absorb heat which is typically controlled by the welding speed (Duley, 1999). For laser welding, many researchers have studied the optimum parameters which give acceptable welds, i.e., sufficient weld depth and narrow widths. Cretteur (2015) stated that most automotive laser welding applications use maximum power capacity of laser in the range 3∽8 kW while speed is adjusted in the range 1∽10 m/min to obtain full laser penetration (i.e., generation of keyhole). For spot size, which mainly influences the weld width, Kielwasser (2009) concluded that smaller spot size increased the energy density and consequently deeper penetration into the sheet, and practically most automotive applications use spot diameters ranging from 0.4∽0.7 mm.

Xu *et al.* (2013) investigated the effect of heat input during welding on the average width of fusion zone (FZ) and (HAZ) by using different laser welding methods and parameters. They concluded that the width of FZ and HAZ decreased with decreasing heat input during welding (see Table 2.1), i.e., the geometry of different welding zones and consequently the regions in which metallurgical transformations occur are affected by welding method and parameters. Cretteur (2015) studied the effect welding speed on the width of the HAZ and the softening ratio. The results showed that a wider HAZ was obtained at low welding speed as more heat transferred to the work piece (high heat input). Moreover, at lower welding speeds, the heat was conducted farther from the FZ and the time spent above the tempering temperature by each point of the HAZ is longer than that in the weld made at higher welding speed, which led to more distinct tempering.

Some researchers have attempted to decrease the HAZ softening by decreasing the local temperature of the area in the vicinity of FZ during welding process by using additional cooling methods such as air, water, water submerging and liquid nitrogen. However, cooling with water has proved to be more effective than the other methods (Sharma *et al.*, 2012). Wei *et al.* (2015) applied a high flow rate of water through grooves in a copper fixture as local cooling method during fiber laser welding of specimens from two different AHSS sheet materials, DP780 and DP980. They found that local cooling could reduce the width of softening area of the HAZ by about 50% and consequently improve the tensile properties of the welded joints. Moreover, subsequent formability of the welded joint in terms of limiting dome height (LDH) tests was improved and the fracture did not occur in the softening zone.

Table 2.1. Effect of different laser welding processes on the width of HAZ and FZ formed in DP980 (Xu *et al.*, 2013).

Welding method	Power (kW)	Welding speed (m/min)	Spot size (mm)	Sheet thickness (mm)	Average width HAZ (μm)	Average width FZ (μm)
Diode	4	1.6	12x0.5	1.2	4000	3000
Nd:YAG	3	3	0.6	1.17	1000	750
CO_2	6	6	NA	1.8	1000	1000
Fiber	6	16	0.6	1.2	250	450

In summary, good quality TWBs with an acceptable level of mechanical properties and ductility for subsequent forming could be achieved by selecting a suitable welding method, parameters and techniques that control or even decrease the amount of heat input during the welding process, and especially when highly affected materials (such as DP steels) are incorporated.

2.4.2 Forming

TWBs made from dissimilar materials of different thickness and/or strength are becoming common in the automotive industry. In recent years the ability of TWBs to reduce weight has been increased by using high-strength steels such as HSLA and AHSS, which also improves the structural integrity performance of the TWBs in crash. In general, formability of TWBs is reduced significantly compared to parent materials due to the presence of the weld. The formability of TWBs is affected by many factors such as base metal properties, thickness/strength ratio, weld orientation, and the effect of welding process on the strength and metallurgical transformation of both FZ and HAZ (Narasimhan and Narayanan, 2011; Nayak *et al.*, 2015). In addition, significant softening may in turn affect the formability of TWBs incorporating DP steels by concentrating strains in the softening region during the forming process, resulting in premature failure (Xia *et al.*, 2007; Panda *et al.*, 2009).

Xia *et al.* (2007) compared the fracture location and LDH values of HSLA and DP980 steel TWBs. They observed that the hardness profile of DP980 is much higher than that of HSLA for the same welding speed. Moreover, the width and location of softening zone of DP980 were affected by the different welding speeds. In addition, the failure in the HSLA welded blank initiated at the welds and propagated perpendicular to the weld line. However, failure of the DP980 welded blanks occurred in the HAZ region parallel to the weld line (at the softened region), while the fracture of its parent blanks initiated farther than the apex of the dome as shown in Figure 2.13. Further, the height of the dome after welding was decreased by about 2% and 57% than the height of the parent blank for HSLA and DP980, respectively. In other words, the formability of TWBs depends not only on the initial but also the post-welding properties of base steel sheets.

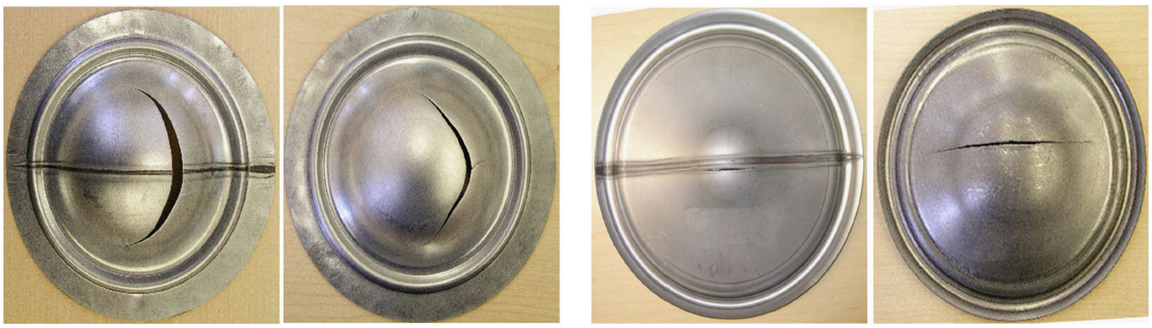

(a) HSLA. (b) DP980.

Figure 2.13. Fracture location of both parent and TWBs specimens of (a) HSLA, and (b) DP980 (Xia *et al.*, 2007).

Sreenivasan *et al.* (2008) studied the formability of AHSS (DP980) and found a significant decrease in LDH of TWBs due to softening in the HAZ and the fracture to occur in the tempered HAZ. Moreover, the formability of the TWBs in terms of LDH was improved by decrease in the width of HAZ and its less softening with increasing welding speed. The width and degree of softening zone within the HAZ are controlled by the amount of heat input during welding and the resultant cooling time between 800 ^{o}C and 500 ^{o}C (or $t_{8/5}$) (Denys, 1989). Maurer *et al.* (2012a) proposed that the strength of the welded joints increases with decreasing width of softening zone and it may reach the strength of the parent metal. This was referred to as the "constraint" effect which can be defined as the suppression of plastic flow of the softening zone by the stronger area in its vicinity. De Meester (1997) stated that the constraint effect is significant if the width of softening zone, W_{SZ}, does not exceed the thickness of the parent materials, t, (see Figure 2.14 (Maurer *et al.*, 2012b)).

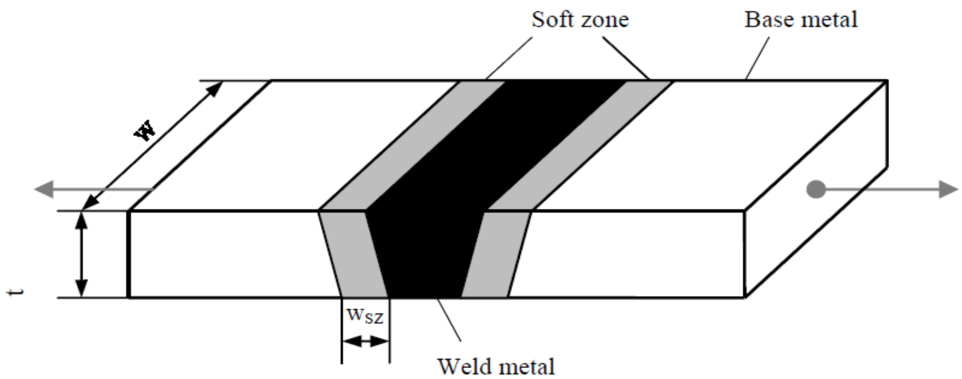

Figure 2.14. Schematic drawing of steel welded joint with a soft interlayer (Maurer *et al.*, 2012b).

Aside from initial and post-welding properties of base metal, thickness/strength difference affects the formability behavior of TWBs. Chan *et al.* (2003) investigated the effects of the thickness ratio of TWBs on the experimental forming limit curve (or FLC) by varying TWBs width to achieve various strain paths from balanced biaxial tension to uniaxial tension with transverse orientation of the weld line. The results showed that the FLC of the TWBs were lower than the base metal, which was expected. Indeed, as the thickness ratio between blanks of the TWB increased, the FLC steadily shifted downward. The trends with respect to thickness ratio are similar to the studies carried out by Panda *et al.* (2009) for the effect of strength ratio on LDH values. The results showed that the LDH values of the TWBs were lower than the base sheet materials. Also the LDH values decreased with increasing the strength of the TWBs (see Figure 2.15).

It is to be noted that strength ratio and thickness ratio not only affect the formability of TWBs, but also lead to weld line movement during forming process (see Figure 2.16). As the thickness and/or strength ratios between the two base blanks of TWB increase, the weld line movement increases since the thinner or weaker blank in the TWB undergoes more deformation. Hence, the weld zone moves from its initial position towards the side of the thicker or stronger blank (Narasimhan and Narayanan, 2011).

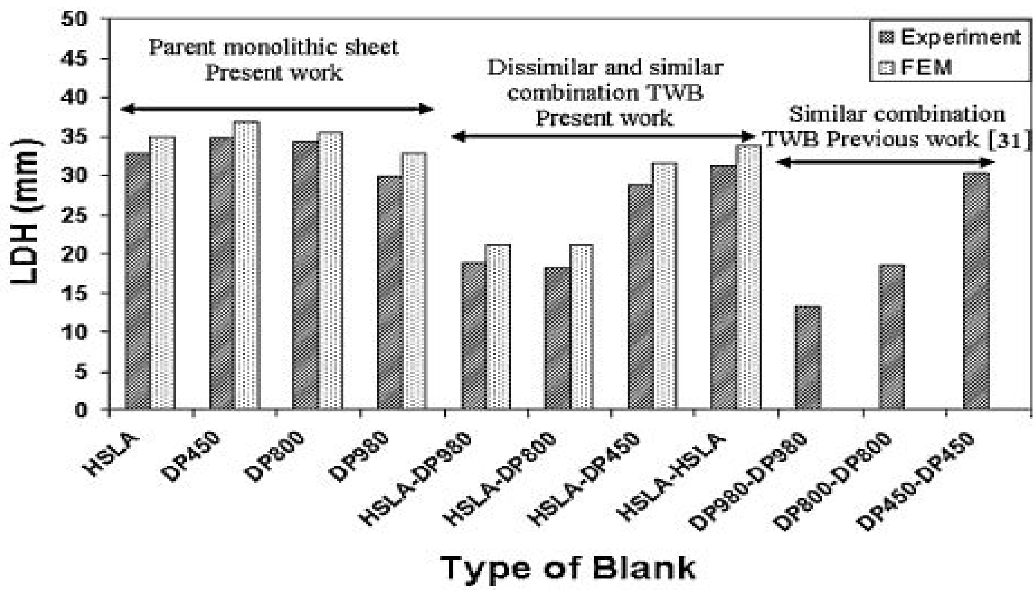

Figure 2.15. Comparison of LDH of different metals and TWBs of different combinations (Panda *et al.*, 2009).

The weld line movement poses a great challenge in formability testing of TWBs as it can lead to reduction of formability and tool design issues. Tools made for conventional single sheets cannot be directly used for forming TWBs, as the thickness difference in the sheet can not be accommodated especially in the clamping region. If the TWB is made of dissimilar thickness blanks, uniform blank holder pressure can not be applied on the blank, as uniform contact between the thinner blank and the tool is absent. In such situations, the thickness difference should be compensated, otherwise wrinkling of the thinner metal, tearing near the weld region and/or weld line movement will occur, which will deteriorate the formability of the welded blanks.

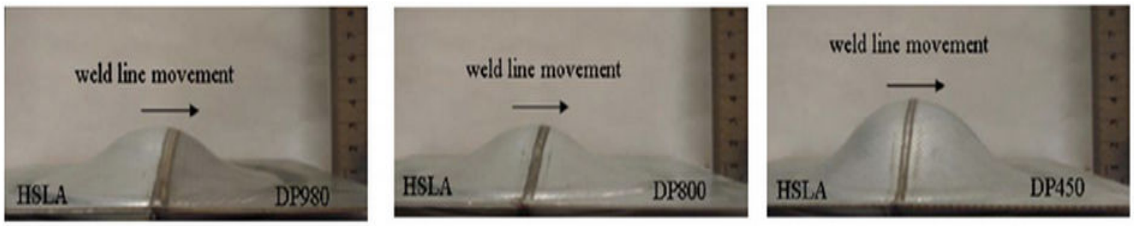

Figure 2.16. Comparison of LDH and weld line movement of TWBs for different metal combinations (Panda *et al.*, 2009).

Compensating the thickness difference can be achieved in several ways such as; (1) shim (piece of sheet inserted below or above the thinner blank in the clamping region), (2) stepped die or blank holder, which is widely used in industries (where die is segmented into different regions) (see Figure 2.17). However, these techniques do not completely solve the weld line movement issue, and problems are encountered with such methods. Utilizing shims initiates fracture in the thin gauge sheet at the shim boundary (Jain, 2000). Also stress concentration may occur if the upper or lower die is not slackened enough in a stepped die technique (Narasimhan and Narayanan, 2011). Therefore, it is essential to understand and control the weld line movement during forming of TWBs with different thickness and/or strength blanks.

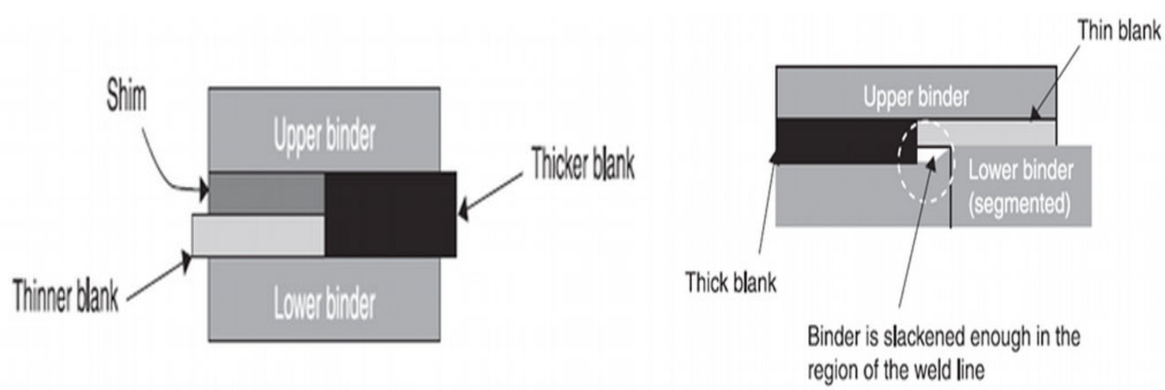

(a) (b)

Figure 2.17. Schematic of some techniques for thickness difference compensation in TWBs (a) shim, and (b) stepped binder (Narasimhan and Narayanan, 2011).

Generally, the formability of TWBs is reduced after welding especially when mechanical properties and microstructure sensitive parent materials are incorporated in the TWBs where premature failure may occur due to softening in HAZ. In addition, weld line movement should be controlled so as to understand the formability of TWBs with thickness and/or strength difference of two base materials.

2.5 Steel-to-aluminum TBBs

2.5.1 Brazing

Joining dissimilar materials combinations such as aluminum and steel pose a number of problems as well. Since the melting temperatures of aluminum and steel are quite different, most conventional fusion welding processes do not yield a sound joint (Padmanabhan *et al.*, 2008). Moreover, the near-zero solubility between aluminum and steel, poor wetting behavior of aluminum, and other differences in physical and chemical properties of the base metals result in the formation of brittle intermetallic compounds (IMCs) layer in the steel/aluminum faying surfaces area (Katayama, 2004; Shah and Ishak, 2014; Sun and Ion, 1995). The brittle IMC leads to a fast fracture of the joint under dynamic (and even static) stress, and consequently affect post-joining deformation and forming (Moller and Thomy, 2013).

Mathers (2002) presented several dissimilar aspects of physical and mechanical properties that complicate the joining process of aluminum and steel; namely, the melting and boiling points of the two metals and their oxides are different, aluminum has approximately twice the coefficient of thermal expansion and six times the coefficient of thermal conductivity compared to steel, the specific heat of aluminum is twice that of steel, and the modulus of elasticity of aluminum is one third that of steel. These incompatibilities pose a significant problem during welding of steel and aluminum sheets.

The solubility of steel in liquid aluminum is close to zero and the solubility of aluminum in steel is quite limited. Moller and Thomy (2013) found that IMC formation occurs when the aluminum content in steel exceeds a volume fraction of 12%. Depending on the aluminum content and the time-temperature cycle, the phases Fe_3Al, FeAl, $FeAl_2$, $FeAl_3$ and Fe_2Al_5 or even more complex structures of higher order are formed. These IMCs form barriers to the welding process of steel to aluminum. Figure 2.18 shows Fe-Al phase diagram and the various IMCs (Massalski *et al.*, 1986).

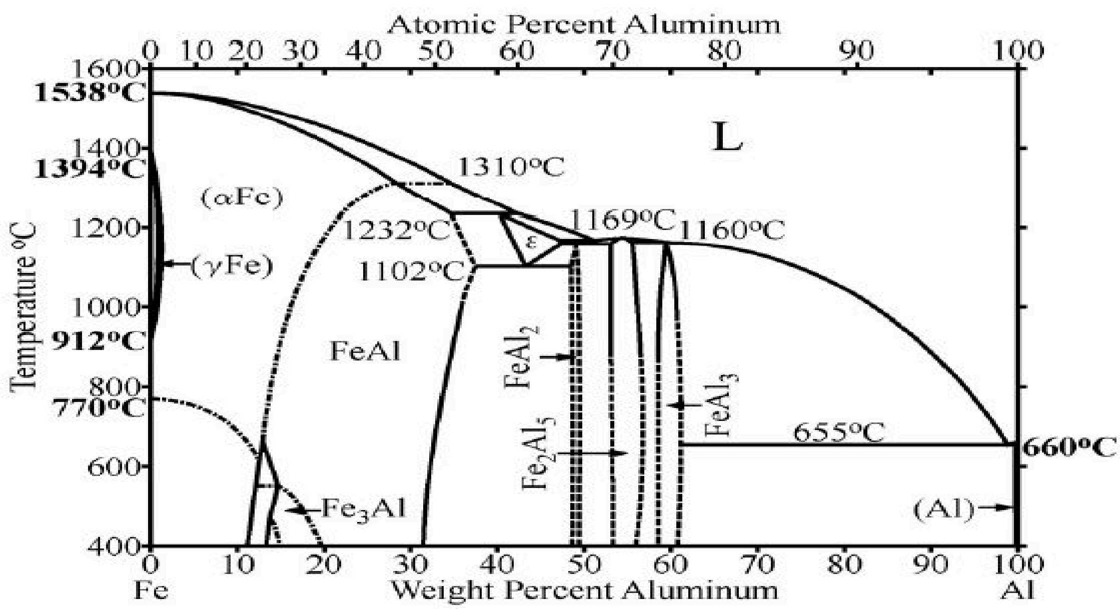

Figure 2.18. Phase diagram for the Al-Fe binary system (Massalski *et al.*, 1986).

Thermodynamic calculations have shown that the aluminum-rich phases are formed preferably (Moller and Thomy, 2013). This was also proved by experimental investigations of Wirth *et al.* (2007). The mechanical properties of IMCs were studied by Yasuyama *et al.* (1996). They found that phase layer hardness increased with increasing aluminum content, i.e., aluminum-rich phases. Table 2.2 presents the microhardness values in HV for the IMCs formed throughout the contact surfaces of the materials. Therefore, the IMC layer is a major concern in aluminum-steel dissimilar brazing. It is to be noted that, most published papers in this field have mainly focused on parameter optimizations and techniques to curb the formation of this layer. Ozaki and Kutsuna (2009) proposed that if the thickness of brittle IMCs layer (aluminum-rich phases) is minimized and the formation of more ductile IMCs layer (iron-rich phases) is promoted, more reliable joints could be obtained. Similarly, Kreimeyer and Sepold (2002) proposed that IMCs layer thickness of less than 10 µm could result in more mechanically sound joint. Dharmendra *et al.* (2011) experimentally investigated the mechanical resistance of Fe-Al brazed lap joint configurations. The thickness of IMCs layer varied in the range 3-23 µm by using different brazing speeds. Joints with IMCs thickness between 8 and 12 µm exhibited higher mechanical resistance. Shi *et al.* (2012) studied the relation between IMCs layer thickness and welding time of lap welded joint configuration. The results showed that aluminum-rich layer thickness in the interface increased with the increase in welding time and the strength of the joint was inversely related to the IMCs layer thickness. Therefore, a thinner IMCs layer contributes to improved dissimilar weld joint strength.

Table 2.2. Vickers hardness of IMCs for Fe-Al binary system (Moller and Thomy, 2013).

Phase	Microhardness HV
Fe_3Al	250-350
FeAl	400-520
$FeAl_2$	1000-1050
$FeAl_3$	820-980
Fe_2Al_5	1000-1100

An alternative approach was adopted by other researchers. They studied the effect of filler materials in inhibiting IMCs formation. In Song *et al.* (2009) and Dong *et al.* (2012), improved filler metals were used during welding by increasing the Si contents. The results showed that ductile Al-Fe-Si ternary phases, which have a lower formation enthalpy, replaced the brittle Al-Fe phases. Moreover, Si additions prevented the build-up of IMCs layer, and minimized its thickness. In addition, Mathers (2002) found that Si-rich aluminum fillers also mitigated hot cracking in weldments. However, Si percentage should be limited to 5 wt.% to produce optimum mechanical property (Song *et al.*, 2009). In addition, the selection of galvanized steel had been shown to have a positive effect on aluminum/steel welding. Lin *et al.* (2010) and Zhang and Liu (2011), observed that the existence of a thin Zn layer on the surface of steel sheets assisted in the welding process because Zn has good metallurgical compatibility with both aluminum and steel. However, additional precautions have to be considered when using such coatings. More heat input yields better wettability, but Zn layer has a lower boiling point of about 907^{o}C. It can evaporate during welding process causing pores in the weld joint that can decrease the joint strength (Mathieu *et al.*, 2006; Dong *et al.*, 2012).

Most researchers believe that an efficient means to reduce phase formation, and potential decrease in joint brittleness, is limiting the time when the joining zone is at elevated temperature (Moller and Thomy, 2013). Some studies utilized nonfusion joining processes in order to minimize the heat input during joining and consequently overcoming the problem of brittle IMC formation. Processes such as resistance welding (Qiu *et al.*, 2009; Zhang *et al.*, 2014), friction welding (Habibnia *et al.*, 2015), explosion welding (Tricarico and Spina, 2010), and ultrasonic welding (Haddadi and Abu-Farha, 2015), have been used. However, these processes are only suitable for certain joint configurations, and offer lower productivity and flexibility, thus limiting their industrial-scale sheet joining applications.

Ozaki *et al.* (2010) proposed that controlling heat input and the time-temperature cycle during fusion welding process leads to attainment of optimized joints in dissimilar materials. Based on this concept, laser welding provides advantages over conventional fusion joining methods in terms of weld quality, high welding speed, flexibility, high energy density, localization of fusion with reduced HAZ, and accurate control of heat input that limits the IMCs layer thickness to a few microns (Mathieu *et al.*, 2006). In particular, hybrid welding processes such as Laser/MIG hybrid brazing, where two distinct welding methods are used simultaneously to take advantage of both methods, have shown to enhance plastic flow, improve elongation, shorten welding time, and yield better aluminum and steel weld joints (Shah and Ishak, 2014; Thomy and Vollertsen, 2012).

Thomy and Vollertsen (2012) investigated the effect of Laser/MIG hybrid welding process parameters on the joining of aluminum alloy (AA6016) to zinc-coated steel sheets (DC05) with filler wire (AlSi12) in a butt joint configuration. The effect of process parameters on joint properties such as wetting length, IMCs layer thickness and tensile strength were examined. The experimental testing of hybrid welding process showed that increasing of laser power above 3.2 kW increased the phase layer thickness to 12 µm and cracking occurred without any application of external load. However, for all other laser powers in the range of 2∽3.2 kW, tensile strength remained well in the range of 180 MPa. Whereas, for MIG arc welding, the phase layer thickness was less than 4 µm for all powers inputs. However, increasing MIG power above 3.2 kW deteriorated the regularity of the seam and reduced tensile strength to 150 MPa. With respect to wire feed rates, phase layer thickness of less than 4 µm was obtained for all feed rates and tensile strength was in the range of 180 MPa. However, the welding speeds and feed rates had to be adjusted simultaneously to obtain regular wetting since insufficient wetting drastically reduced tensile strength to below 120 MPa.

The most recent technique, CMT method variant of MIG welding process, can be used to join aluminum sheets to galvanized steel sheets. In this method, droplet detachment occurs based on short circuit welding, i.e., wetting of the steel substrate by melted droplets of filler wire takes place in the off-current period (lower heat input) (see earlier section 2.2.3). A successful joining attempts were conducted by CMT method using 5xxx and 6xxx aluminum alloys sheets, and the failure of these joints occurred in aluminum base with sufficient mechanical properties of the brazed joints (Fronius, 2015).

In conclusion, different coefficients of thermal expansion and limited solubility between aluminum and steel result in inadequate joint properties. Therefore, controlling or even decreasing of the heat input can mitigate the negative effects of thermal expansion and solubility differences, and yield better steel-to-aluminum joints.

2.5.2 Forming

Despite the fact that butt joints are the common configuration, most researchers studying joining of steel and aluminum prefer a lap joint configuration. It is largely because joining of aluminum/steel in butt joint configuration (as in TBBs), is relatively difficult (Shah and Ishak, 2014). Hence, useful studies related to the mechanical properties and the effect of sample geometries on failure location of TBBs with butt joint configuration are lacking. There is no published research on stretching of TBBs in different strain paths or out-of-plane stretch forming.

Some researchers have attempted to obtain a correlation between bonding parameters and the mechanical properties of TBBs. Moller and Thomy (2013) related the tensile properties of aluminum/steel TBBs to two main aspects of bonding during brazing process; the wetting of the substrate material by the braze metal, and the formation of IMCs in the interfacial surfaces between the braze and substrate metals. Mathieu *et al.* (2007) found a roughly linear correlation between wetting length and tensile strength. Moller and Thomy (2013) proposed that both wetting length and the shape of weld seam have an influence on static strength. Moreover, if seam quality is sufficient, the location of fracture not only depends on wetting length but also on the cross-section of the aluminum/steel interface zone. Fracture may be initiated at a small pore close to the interface zone and its propagation can occur along the IMCs layer (see Figure 2.19). Similar results were observed by Sun *et al.* (2015) for laser brazed butt joints of AA6013 and low carbon steel (Q235) using 4043 filler material. The results showed the thickness of IMCs layer to be 1.8 to 6.2 µm for various brazing parameters. The aluminum/steel butt joints failed at the brazing interface during the tensile test and reached a maximum tensile strength of 120 MPa.

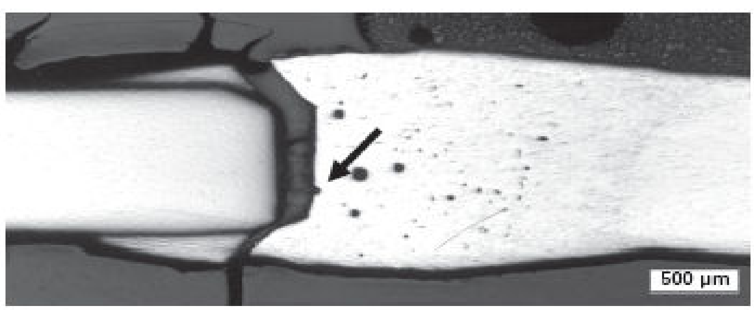

Figure 2.19. Cross section of fracture of steel-to-aluminum TBBs (Moller and Thomy, 2013).

Thomy and Vollertsen (2012) investigated the mechanical performance of Laser/MIG hybrid welding of (AA6016) to zinc-coated steel sheets (DC05) with AlSi12 filler wire in a butt joint configuration. The welded blanks exhibited good bendability in longitudinal bend test (a bending angle of 180^o with bend radius 10 mm), and no transverse cracking or delamination was observed (see Figure 2.20).

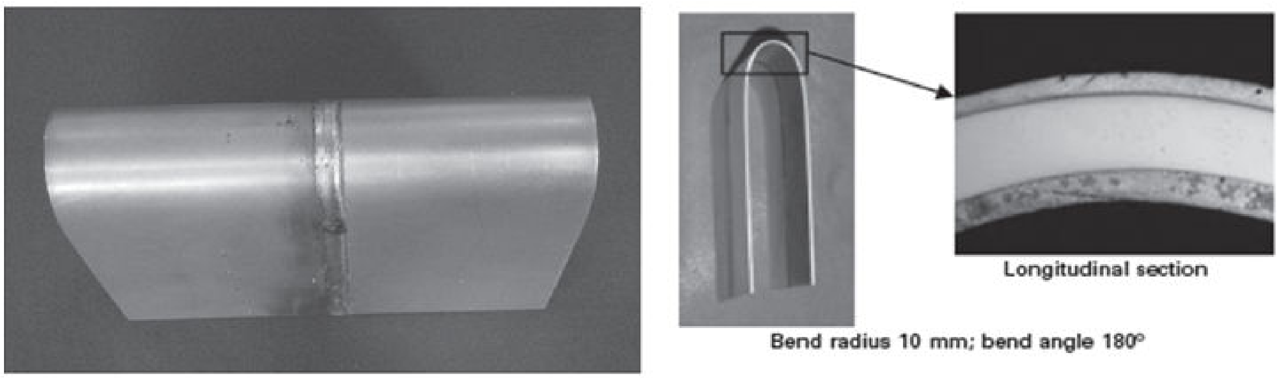

Figure 2.20. Bend test of Laser/MIG hybrid welded aluminum-steel sheet (Thomy and Vollertsen, 2012).

2.6 Summary

From the above-mentioned literature review, it is shown that TBs offer an excellent means to meet competing and seemingly contradictory demands; weight reduction at lower cost without trade-off in structure integrity. However, joining process required to produce TBs and the subsequent stamping process required to bring the produced blanks to the desired shapes are still complex and pose challenges especially when dissimilar materials of different physical and/or chemical properties with dissimilar thicknesses and/or strengths are incorporated. Generally, the results and conclusions obtained emphasized on the following points:

- The non-conventional high-power laser beam welding in general, and fiber laser beam welding in particular, offers a promising alternative joining process for production of TWBs due to many advantages which outweigh other conventional welding processes especially when the parent materials are affected by the amount of heat input during the welding process.

- The welding parameters have to be optimized carefully so as to not only obtain sound welds in TWBs, but also not reduce the base metals hardness (HAZ softening) especially when the parent metals are highly affected by the amount of heat input during welding. Softening in the weld region can lead to premature failure during the post-joining forming process (as in case of AHSS).

- The formability of TWBs is generally lower than the parent materials. Moreover, weld line movement, which is common issue in forming of TWBs with dissimilar thickness and/or strength must be solved with suitable formability test design and test methodology.

- Brazing parameters, brazing time, filler wire materials and properties of parent materials as well as surface coatings have been shown to affect joining of aluminum and steel sheets to produce TBBs. Additionally, wetting of the substrate material by the braze metal, and the formation of IMCs in the interfacial surfaces between the braze metal and the substrate metal have an effect on braze interface strength, quality, and joint mechanical properties.

- Hybrid welding processes (such as Laser/MIG hybrid brazing) have been shown to enhance plastic flow, improve elongation, shorten welding time, and can yield better aluminum and steel brazed joints of higher strength.

- Cold metal transfer brazing processes (or CMT brazing) have been recently introduced and has the potential to join aluminum and steel to create TBBs.

- In general, ductility and formability of steel-aluminum joint are expected to be dependent on the interface strength and geometry and relative strengths/thickness of the parent materials. However, no studies related to aspects of large deformation and formability of TBBs are yet available in the literature.

Chapter 3

Research Plan

This chapter describes a research plan for each of the current research objectives presented earlier in Chapter 1.

3.1 Plan for objective 1

The first objective is concerned with studying the formability of TWBs made from DP780 1 mm sheets welded together using defocused fiber laser welding as well as the formability of DP780 parent sheets. The defocused fiber laser welding method will be utilized to, (i) decrease the amount of heat input during welding which in turn is expected to minimize the width of HAZ, and (ii) increase the weld pool volume and consequently reduce the requirement of the fit-up precision prior to welding (Kuryntsev and Gilmutdinov, 2015). The larger weld pool volume is also expected to remelt the defects that are generated during the welding process. Therefore, the effect of using defocused fiber laser welding process on the formability of DP780/DP780 1 mm/1 mm TWBs will be examined and compared to that of parent sheets in terms of forming limit strains, limit dome height (LDH), fracture position with respect to the weld line and fracture mode.

LDH test will be utilized in the form of standard 4 inch (101.6 mm) diameter hemispherical punch to stretch the test specimen (parent sheets and TWBs). This test will utilize upper and lower dies with a central circular hole and lock-beads within each die to prevent drawing in of the blank during the hemispherical punch stretching process. The test will be typically stopped at the onset of visible necking of the specimen. The various strain paths will be achieved by using different specimen width geometries to obtain the left side of FLD (negative minor strain region), and by modifying the friction state at the punch sheet interface to obtain the right side of FLD (positive minor strain region). All of the test samples will be machined to geometries shown in Figure 3.1.

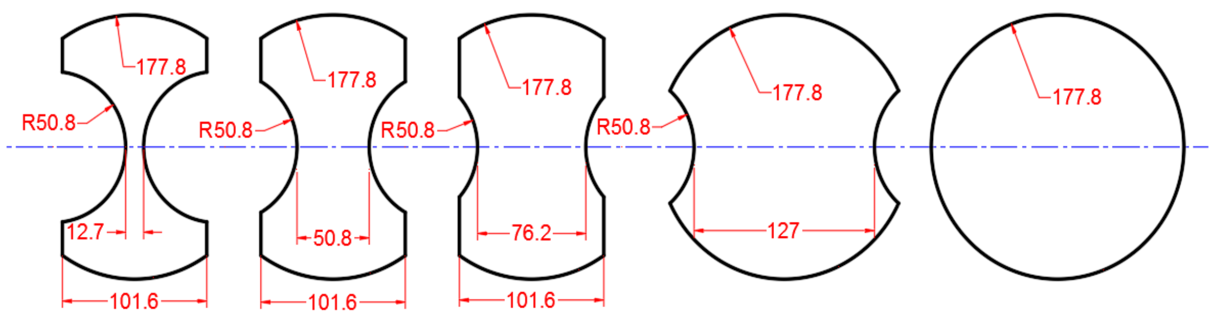

Figure 3.1. Schematic drawing of different sample geometries for different strain paths of TWBs and parent sheets.

An in-situ on-line full-field strain mapping system, Aramis® from GOM Company (GOM-mbH, 2011), will be deployed to capture the deformation process. Aramis will enable accurate and continuous determination of strain distribution over the surface of the specimen during the test and up to the onset of instability or fracture. Aramis is a non-contact optical strain measurement method based on digital image correlation (or DIC) technique. This technique for full-field strain measurement is especially useful for measuring strains in the irregular weld bead region. The procedure for obtaining limit strains in the neck and fracture region is presented in the next chapter.

3.2 Plan for objective 2

For the second objective, the plan is divided into two parts. In the first part, an in-plane plane strain (IPPS) tension test will be utilized to assess the formability of TWBs, similar in essence to an earlier work of Jain (2000) on aluminum TWBs. In the current research, a new test for TWBs formability assessment, referred to as double-layer test will be developed and assessed. The aim of utilizing such a test is to overcome the limitations associated the formability of TWBs of different gauges and/or strengths such as weld line movement (see earlier Section 2.4.2).

At first, trials with different specimen geometries of one of the parent sheets will be conducted to determine the optimum geometry for the plane strain condition (i.e., minor principal strain of zero). Such a geometry is shown in Figure 3.2. Once a plane strain specimen geometry is established, TWBs made from DP780/DP780 and HSLA/DP780 of different thickness combinations will be machined with this geometry and clamped as a pair of TWBs by stacking the thick gauge region of one specimen over the thin gauge section of another where the weld line will be chosen to be either along or transverse to the loading axis (see Figure 3.3). Each pair of specimens will be spot welded together at the clamping edges to ensure that both layers are properly aligned and the relative sliding between the two layers in the grips region during axial loading is prevented. In-situ DIC strain mapping system Aramis® will be used to capture the deformation process during the test for accurate determination of strain distribution over the entire gauge length of the test specimen up to fracture. Tests will be carried out using MTS servo-hydraulic tensile test frame fitted with hydraulic grips. The conceptual simplicity, rapidity and reproducibility of the in-plane plane strain double-layer specimen concept will be assessed as part of objective 2.

The second part of the plan will deal with further exploitation of the above double-layer concept for TWBs for a broader assessment of formability of TWBs using hemispherical punch stretching test. Therefore, the proposed concept of double-layer TWBs for in-plane plane strain test will be extended to out-of-plane limiting dome height (LDH) test.

As illustrated earlier, two stacking specimens will be machined together with the geometries shown in Figure 3.1 and subjected to hemispherical punch stretching (i.e., LDH) tests to attain different out-of-plane strain paths (see Figure 3.4). The tests will be carried out using MACRODYNE forming press of 150 ton capacity. New die inserts with suitable lock-beads will be designed to conduct hemispherical dome tests of TWBs of different thicknesses. Once again, in-situ DIC-based Aramis® strain mapping system will be used to capture the deformation up to the onset of necking of double-layer TWB specimens of different configurations to generate FLDs.

A comparison will be then made between the formability results of double-layer and single-layer (conventional) approaches to asses the efficiency of double-layer approach in out-of-plane forming mode in terms of weld line movement as well as proximity of neck or fracture location to the weld line of TWBs made from different gauge and strength sheets.

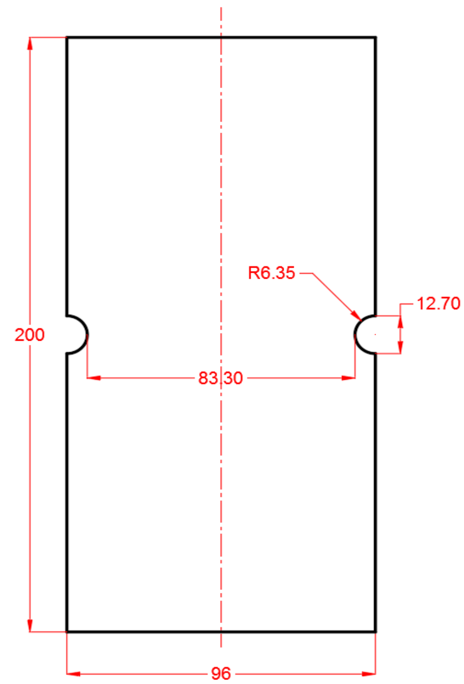

Figure 3.2. Schematic drawing of IPPS test sample geometry for double-layer TWBs.

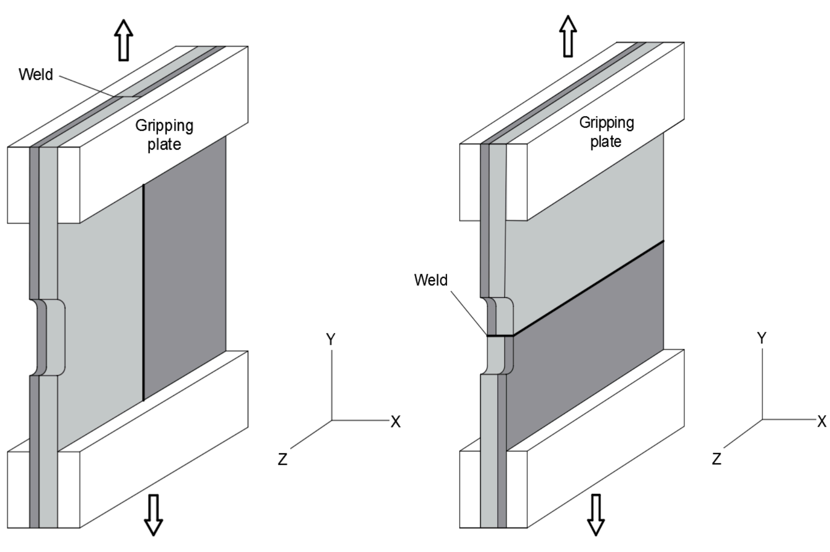

Figure 3.3. Schematic drawing of IPPS test setup for double-layer TWBs with (a) longitudinal weld line, and (b) transverse weld line.

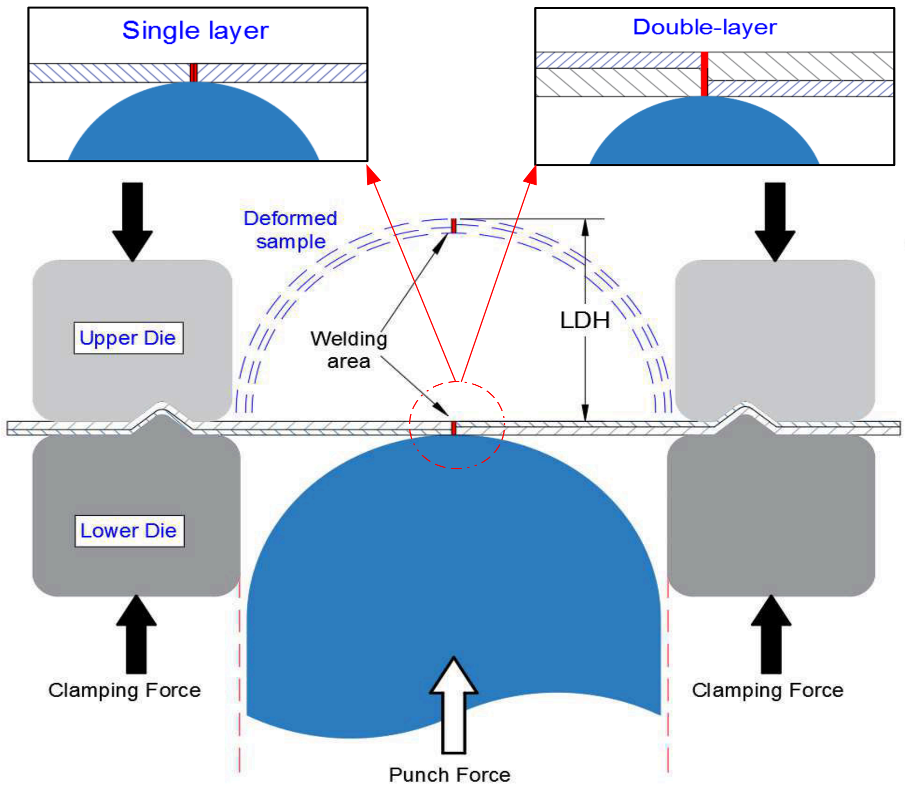

Figure 3.4. Schematic drawing of LDH test setup for both single-layer and double-layer TWBs.

3.3 Plan for objective 3

The third objective pertains to understanding of plastic deformation (general ductility) of steel-to-aluminum tailor brazed blanks (or TBBs). Brazed interface characteristics of TBBs from the point of view of load transfer across brazed interface as well as local deformation and damage in the brazed interface region will be studied. Uniaxial tensile tests will be carried out to assess uniaxial tensile ductility of the AA2024/DP780 1.27 mm/1 mm brazed joints made from Laser/MIG hybrid and CMT brazing methods. The micro-hardness test will be conducted across the through-thickness plane of the TBBs samples to measure the hardness values of different brazed zones. Both tests, tensile and micro-hardness, will provide an understanding of the mechanical properties of the brazed joints.

There is also interest in understanding how the damage initiates in the specimen at the smaller-scale and whether it is associated with any critical strain or stress value. Therefore, a miniature in-situ tensile testing jig, as shown in Figure 3.5, will be used in conjunction with a high magnification digital optical microscope to observe the critical brazed region of finely polished specimens. A very fine speckle-pattern will be applied to the brazed region, as shown in Figure 3.6, to acquire continuous digital images representing the deformation history of the sample. The deformed images will be utilized for DIC-based strain field mapping. Through this test, it will be possible to simultaneously observe the plastic deformation and damage/delamination development in the brazed interface region of TBBs while recording the load development response of the specimen. This methodology will enable relationship between ductile damage development and local strains, as measured by full-field DIC analysis, in the brazed region.

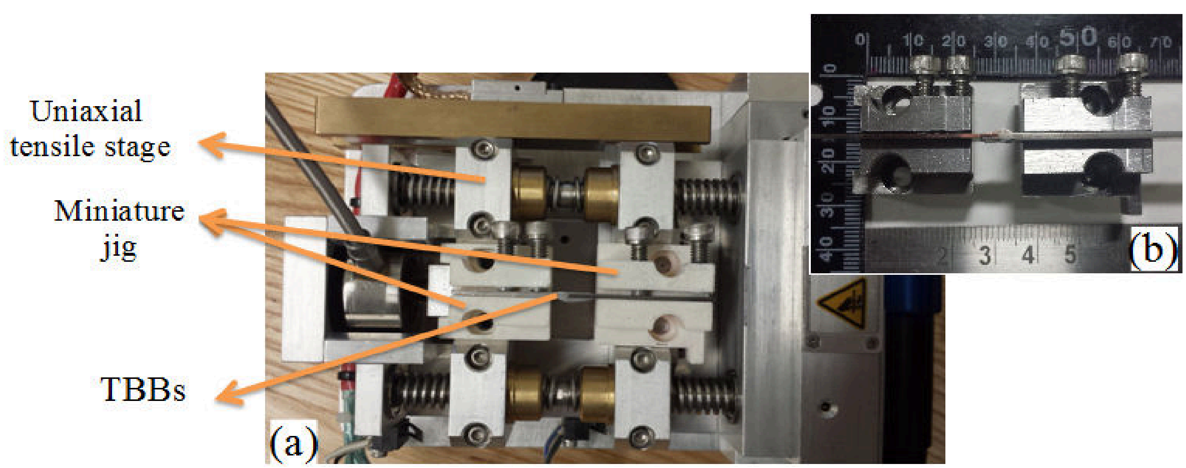

Figure 3.5. Miniature in-situ uniaxial tensile mechanical testing jig; (a) an overview of test jig, and (b) close up of grips region.

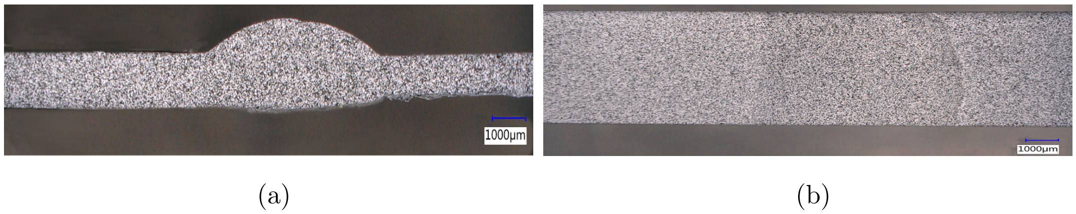

Figure 3.6. TBBs samples with speckle-patterns for miniature uniaxial tensile test; (a) through thickness, and (b) width region.

In addition, brazed samples with different width geometries (as shown in Figure 3.7), will be tested using the earlier experimental test jig of Figure 3.5 to understand the effect of aspect ratio (i.e., ratio of nominal width versus width at groove) on the plastic deformation and/or damage initiation in the brazed interface region.

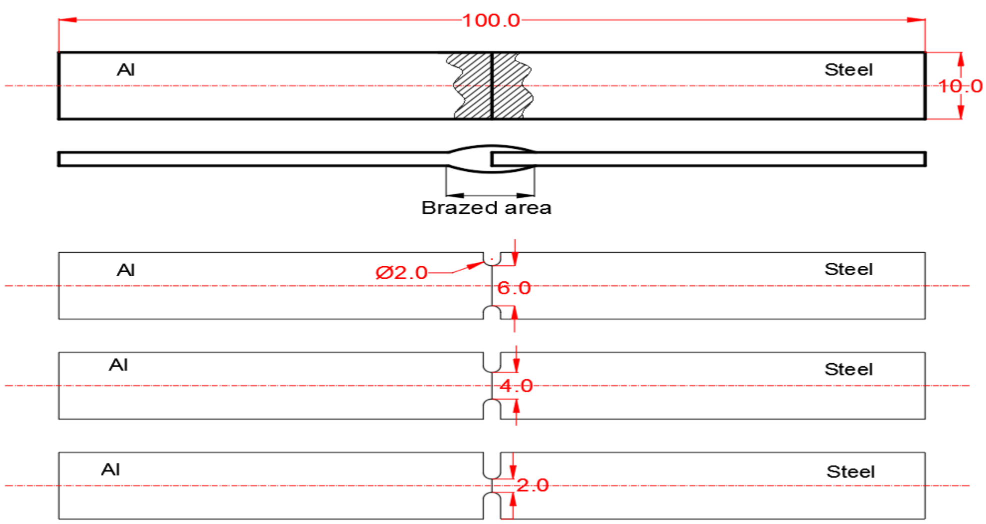

Figure 3.7. Schematic drawing of notched specimen geometries.

It is to be noted that high strength AA2024-T3 sheets are selected to be used in the steel-to-aluminum TBBs because the aim of our research is to study deformation behavior at the brazed interface. Therefore, a higher strength aluminum base metal is required to be stronger than the brazed area (weld seam), and mostly failure will start at the brazed region. Also, all aluminum alloys (heat-treatable and non-heat-treatable) are affect by heat during welding or brazing processes (Schwartz, 2003). So, we need to keep the strength of aluminum base metal as high as possible after brazing process even if it affected by the heat during brazing.

A summary of the research plan in the form of a flow chart is presented in Figure 3.8.

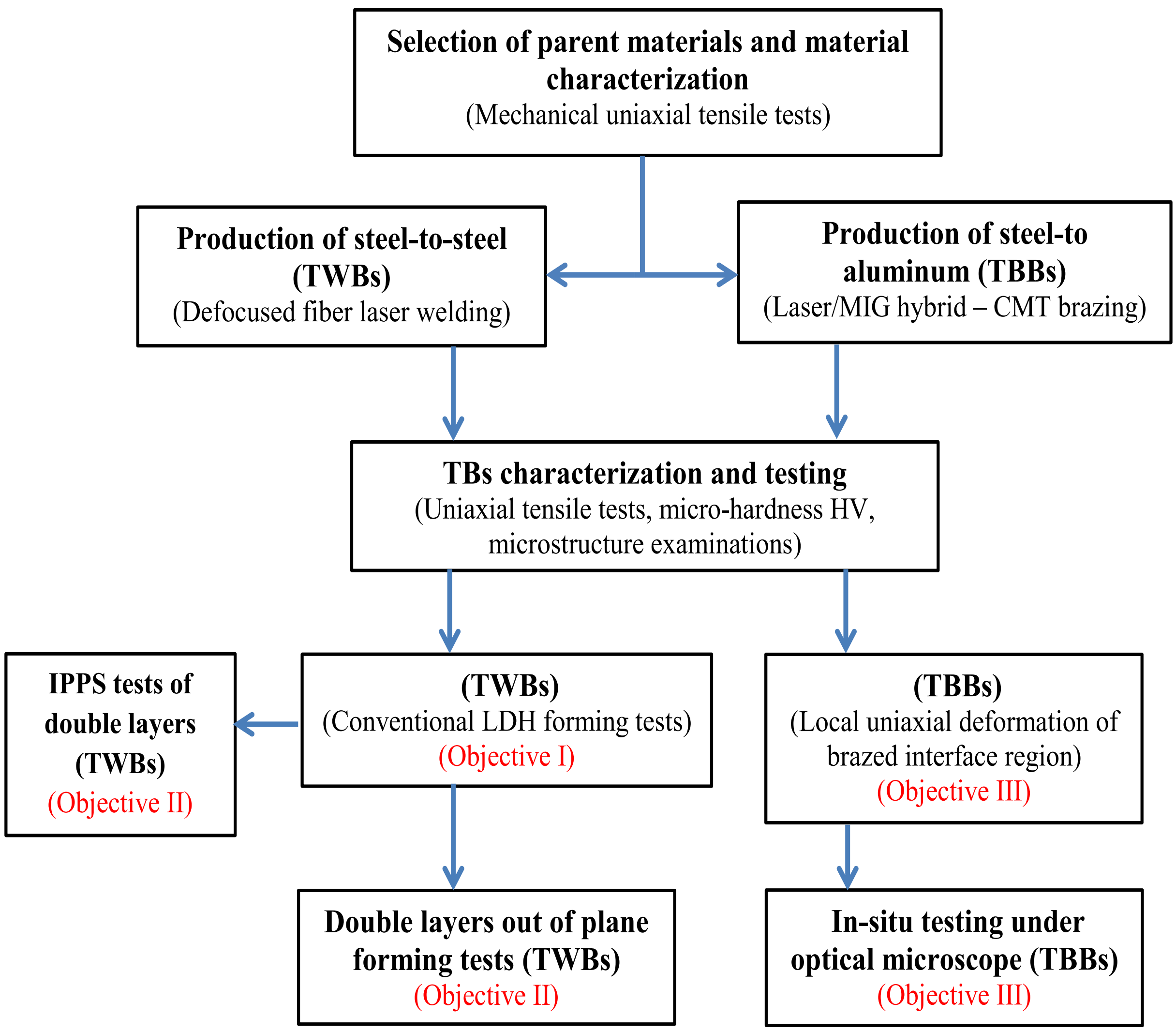

Figure 3.8. Flowchart depicting the sequence of research activities.

Chapter 4

Experimental Methodology

In this chapter, the details of the research methodology and various experimental techniques are provided in the light of research objectives. The methods utilized for characterizing the different properties of both parent materials and tailor blanks are presented. The details of designs, experimental setup and steps followed in specimen preparation, welding and brazing processes, and subsequent forming tests are also presented and discussed.

4.1 Materials

The materials utilized in the current research were all received as cold rolled sheets of DP780 (dual phase steel), HSLA steel, and aluminum alloy AA2024-T3. The steel sheets were received in coated form. A very thin layer of a mixture of intermetallic compounds containing iron, aluminum and zinc using hot dipped galvanizing (GI) process was applied to the HSLA and DP780 steel sheets. Moreover, the DP780 steel sheets were temper rolled after coating to impart a uniform matte surface. The nominal thicknesses of the sheets (with coating layers), are presented in Table 4.1. The chemical composition of these sheets, as reported by the materials suppliers, are listed in Table 4.2.

Table 4.1. Materials used in the current research.

Material	Coating thickness (µm)	Nominal thickness (mm)
DP780	12.25	1 - 1.5
HSLA	11.15	2.3
AA2024-T3	-	1.27

Table 4.2. Chemical compositions of sheet materials (in wt%).

	Chemical composition (weight %)											
Grade	C	Mn	Mo	Cr	Si	Ni	V	Ti	Mg	Cu	Al	Fe
HSLA	0.06	0.64	0.015	0.05	0.24	0.1	0	0.02	-	-	0.03	Bal.
DP780	0.089	2.06	0.116	0.21	0.31	0.01	0.003	0.003	-	0.03	0.046	Bal.
AA2024-T3	-	0.6	-	0.1	0.5	-	-	0.15	1.5	4.4	Bal.	0.5

4.2 Production of tailor blanks

All sheets to be joined, were cut to 200 mm x 100 mm pieces and then welded in butt joint configuration to form a 200 mm x 200 mm tailor blanks (Figure 4.1). The joined edges were precisely cut and milled to ensure close fit-up between them. The sheets were cleaned with acetone to remove contaminations from the surfaces prior to welding. For aluminum sheets, the oxide layer on the surfaces in the vicinity of the edges to be welded were removed and gently cleaned by wire brushing with stainless steel brushes. Subsequently, sheets were held in the welding fixture such that the milled edges were firmly in contact with each other, and clamped with clamping bars to avoid misalignment during welding processes, and then butt jointed together with the weld bead transverse to the rolling direction to produce TWBs and TBBs.

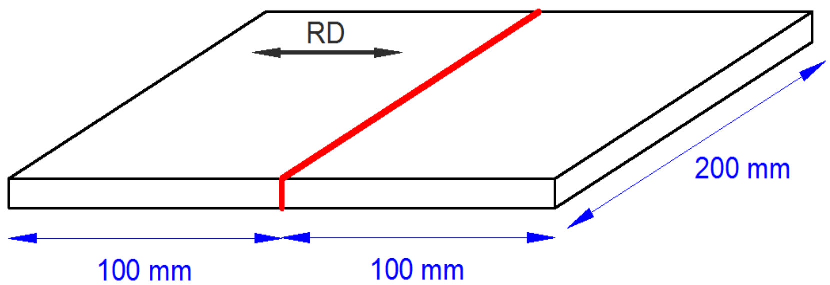

Figure 4.1. Schematic of TBs butt-joint configuration.

4.2.1 Defocused fiber laser welding of steel-to-steel TWBs

Different combinations of steel sheets were laser butt-welded together to produce TWBs. This included the following combinations, (i) DP780/DP780 (1 mm/1 mm), (ii) DP780/DP780 (1.5 mm/1 mm), and (iii) HSLA/DP780 (2.3 mm/1 mm). A high power IPG Photonics YLS-3000 Ytterbium fiber laser head with a maximum power of 3 kW mounted on a FANUC six-axis ARC Mate 120iC robotic arm, was used to weld DP780/DP780 (1 mm/1 mm) and HSLA/DP780 (2.3 mm/1 mm) blanks. In addition, a high power IPG Photonics YLS-8000 Ytterbium fiber laser head with a maximum power of 8 kW mounted on a six-axis ABB 4400 robotic arm, was used to weld DP780/DP780 (1.5 mm/1 mm) blanks. Before the welding operation, the specimen was clamped using clamping bars to the fixture base to keep the specimen in place and prevent any misalignment. The defocused laser beam setup was attained by adjusting the sheet surface above the focus point with defocusing distance ”d” (see the schematic drawing in Figure 4.2).

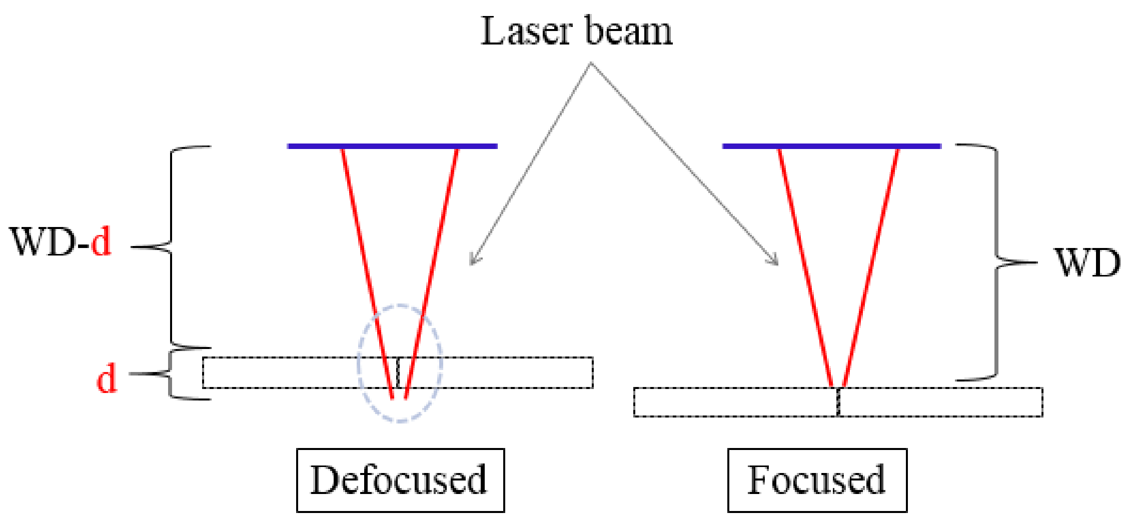

Figure 4.2. Schematic drawing of defocused laser beam setup concept.

During welding, the laser beam source attached to the robot's end was moved along the edges of the samples being joined and the energy from the high power laser beam was concentrated on a small area (spot) to obtain high energy density. A keyhole was created by heating the impingement point of the parent materials above the melting temperature. This allowed the beam to deeply penetrate inside the metals resulting in a deep and narrow weld. No shielding gas was used. However, a high pressure air flow was applied during the welding process to remove metal vapor (plasma fume) from beam incident point as it absorbed the laser radiation, and to ensure keyhole stability. The experimental setup and the welding equipment are shown in Figure 4.3. The welding parameters used are listed in Table 4.3.

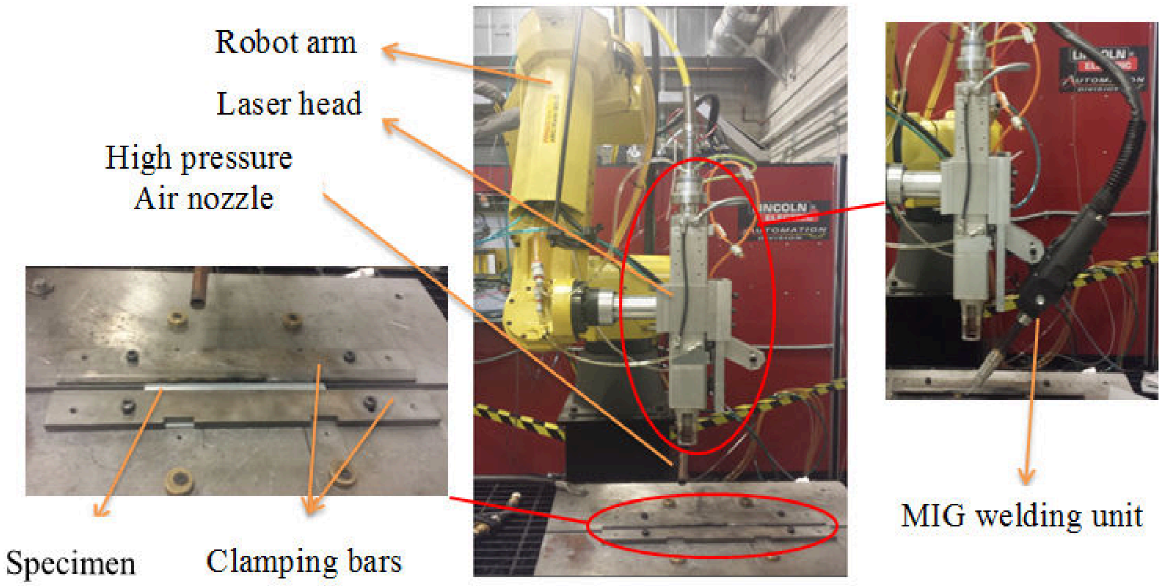

Figure 4.3. Six-axis IPG fiber laser setup for TBs.

4.2.2 Fiber Laser/MIG hybrid brazing of steel-to-aluminum TBBs

The aluminum alloy (AA2024-T3) and AHSS (DP780) sheets were arranged in butt joint configuration with a gap of 0.3 mm using the same setup as in Figure 4.3. In addition, the MIG head was attached to the laser head at an angle of 35^o to the vertical axis of laser head. During brazing, the laser beam, which operated in keyhole mode in the depth direction, was positioned on the aluminum side at a distance of 0.5 mm from the edge to melt the aluminum edge, whereas the projection of the $AlSi_3Mn_1$ filler wire of diameter 1.2 mm was kept behind the laser spot by approximately 5 mm. Shielding gas (100% argon) was fed through the MIG torch at a flow-rate of 20 liters/min. The laser head with MIG unit moved together along the aluminum edges of the samples to be brazed (see earlier Figure 4.3).

The MIG welding was used to create a large melt pool and to supply filler material to the melt pool to increase the melt volume and wetting of steel substrate. The molten wire together with molten aluminum bridged the gap between the aluminum and the steel, and the steel was wetted by both molten aluminum and filler wire. The parameters for hybrid brazing process are listed in Table 4.3. Such a hybrid brazing technique was used to increase brazing speed and to reduce the amount of heat input during joining process. Consequently, the harmful effects of base metal distortion and brittle IMCs layer thickness could be minimized.

4.2.3 CMT brazing of steel-to-aluminum TBBs

AA2024-T3 aluminum and DP780 steel sheets were arranged in butt joint configuration with gap of 0.3 mm using the welding equipment shown in Figure 4.4a. The clamping fixture for aluminum and steel sheets is shown in Figure 4.4b. $AlSi_3Mn_1$ filler wire (electrode) of diameter 1.2 mm was used. The electrode was biased by half of the wire diameter (i.e., 0.6 mm) towards the aluminum sheet with zero working angle between the torch head and the normal to workpiece surface (see Figure 4.4c).

During CMT brazing cycles, the detached molten wire droplets dipped into molten aluminum and bridged the gap between the aluminum and steel. The steel was wetted by the molten filler wire droplets at lower current and cold metal transfer occurred (see earlier Section 2.2.3, Chapter 2). Shielding gas (100% argon) was fed through the torch head at a flow-rate of 20 liters/min. The CMT cycles were repeated while the torch head moved along the aluminum edges of the sample to be brazed. The parameters for the CMT brazing process are listed in Table 4.3. The CMT brazing trials were conducted in collaboration with Fronius, Canada.

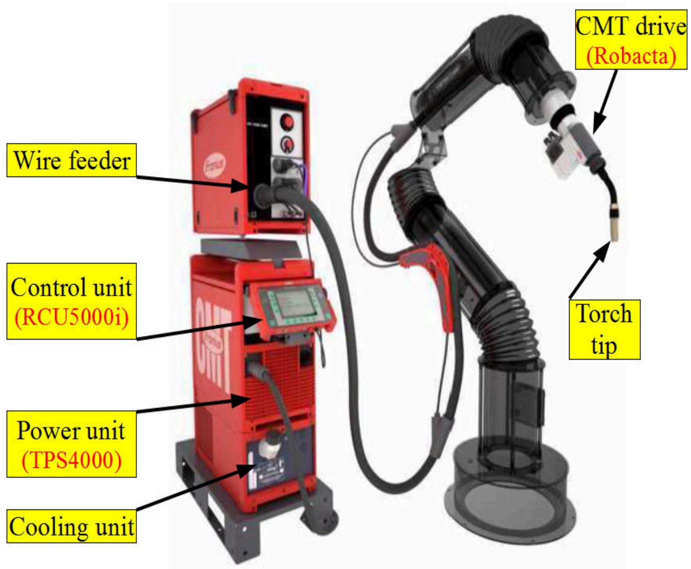

(a) CMT machine components.

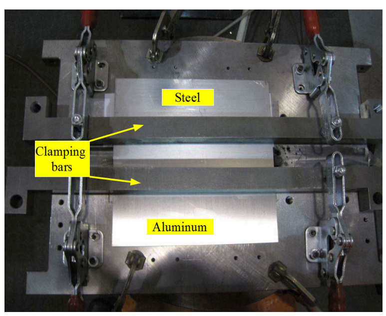

(b) Clamping fixture.

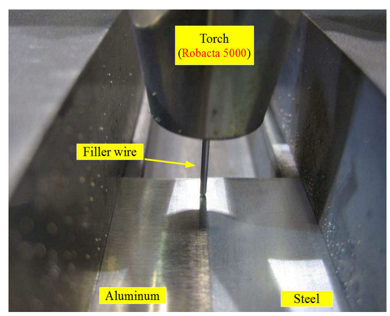

(c) CMT brazing.

Figure 4.4. Experimental setup for CMT brazing method, (a) CMT machine components, (b) workpiece clamping fixture, and (c) CMT torch tip.

The CMT technique is a fully-controlled brazing process that operates in a short-circuit mode. It was mainly used to reduce the amount of heat input during joining of aluminum and steel and to minimize the brittle IMCs layer thickness, and thereby, achieving better mechanical performance of the brazed joint.

Table 4.3. Welding and brazing parameters for TWBs and TBBs.

	Laser welding (TWBs)		Laser/MIG brazing (TBBs)	CMT brazing (TBBs)
	G1 & G2	G3	G4	G4
Power (kW)	3	6	2.3 (laser&MIG)	-
Welding speed (m/min)	7 - 4.5	14	5.75	0.3
Spot size (mm)	0.6	0.6	0.6	-
Focal length (mm)	300	300	300	-
Defocus distance (mm)	-6	-8	-6	-
Working angle (^{o})	6	6	6	0
Filler material	-	-	$AlSi_3Mn_1$	$AlSi_3Mn_1$
Feed rate (m/min)	-	-	∽10	∽3.5
Shielding gas (L/min)	Air (20)	Air (20)	Argon (20)	Argon (20)
current (A)	-	-	-	32
Voltage (V)	-	-	-	20
Frequency (Hz)	-	-	-	22

G1: DP780/DP780 (1 mm/1 mm), G2: HSLA/DP780 (2.3 mm/1 mm),

G3: DP780/DP780 (1.5 mm/1 mm), G4: AA2024-T3/DP780 (1.27 mm/1 mm).

4.3 Material characterization

The produced TBs (i.e., TWBs and TBBs) were then tested to characterize the mechanical properties in uniaxial tension. In addition, weld and braze microstructures were revealed using optical metallography techniques. The results from these tests were examined and compared with the corresponding results from parent materials to check the quality of joining process as well as the effect of joining parameters on welded zones and base metals. Once an acceptable level of mechanical properties (i.e., no failure in the fusion zone), microstructures, and visually sound welds and brazes were obtained, the formability tests on TWBs and uniaxial tension tests on TBBs with miniature tensile specimens were carried out. The details of tests procedures for characterizing the TBs are described below.

4.3.1 Uniaxial tensile test

Uniaxial tensile tests were performed on parent materials, and welded and brazed samples to obtain the standard tensile properties, such as yield strength (YS), ultimate tensile strength (UTS), percent elongation, and power law parameters of strain hardening coefficient (n), and strength coefficient (K). The sub-size tensile specimens were machined according to ASTM E8/E8M-13a (2013) standard with geometry shown in Figure 4.5.

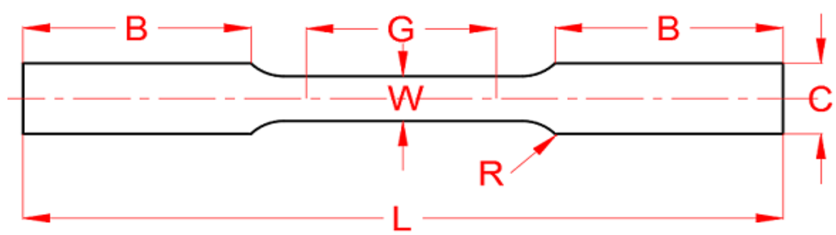

	Dimensions (mm)
G- Gauge length	25
W- width	6
R- Radius	6
C- Width at gips	10
B- Length at grips	30
L- Total length	100

Figure 4.5. Schematic drawing of sub-size tensile specimen.

The tensile specimens from parent materials were tested along the rolling direction, whereas the welded/brazed ones were tested with welding line transverse to tensile axis.

All tests were conducted using MTS servo-hydraulic system with 100 kN load cell under a uniform cross-head speed of 1 mm/min. The load displacement traces were continuously recorded during the test. Simultaneously, images were recorded from gauge region and calculations were carried out using Aramis® system based on digital image correlation (DIC) technique.

4.3.2 Microstructure examination

To examine the microstructures of welded and brazed profiles of TWBs and TBBs, cross-sections were prepared according to standard metallographic procedures to reveal the microstructure of the different zones in the joined specimens. For steel-to-steel TWBs specimens, the main steps involved precision cutting, mounting and grinding using a series of SiC papers of grit sizes 320, 400, 600, 800 and 1200, followed by polishing with diamond suspension. The specimens were then etched using a 2% Nital solution for about 10 seconds. The steel-to-aluminum TBBs specimens were prepared using similar grinding and polishing procedures but only to check the quality of brazing profiles. i.e., to observe if the brazed region was free from cracks and exhibited enough wetting of steel substrate. The average wetting lengths and IMCs layer thickness were measured at the faying surfaces. The weld and brazed profiles were observed using a Keyence VHX-5000 digital optical microscope with a magnification up to 2000X.

4.3.3 Microhardness test

Vickers micro-hardness (HV) profiles were obtained across the weld/braze line from through-thickness optical metallography mounts in the etched condition to reveal the microstructure. LECO M-400-H2 micro-hardness tester was utilized with an applied load of 200 gram and a dwell time of about 10 seconds. The indentation step spacing was 0.1 mm to avoid interference from the strain fields between adjacent indents.

The micro-hardness test was expected to give a direct and accurate indication of the effect of joining parameters on the welded and brazed samples. Moreover, microhardness test together with microstructure examination test were used to identify the width and geometry of different welding zones and position of softening zone and IMC layer thickness.

4.4 Formability tests

To investigate the effect of welding and brazing processes on the deformation and forming behavior of visually defect-free TBs, a series of formability tests were performed for steel-to-steel TWBs and steel-to-aluminum TBBs. The steps for conducting these tests started with gridding surfaces of the tested specimens with random dots (stochastic speckle pattern), then performing the in-plane plane strain and hemispherical punch stretching tests, and ending with post-forming strain measurements. In this section, procedures of the formability tests are presented. The gridding of test specimens and the subsequent strain measurements are presented later in Section 4.5.

4.4.1 Formability tests of TWBs

4.4.1.1 Deformation behavior of single-layer TWBs

To obtain the forming limit diagram (FLD) of TWBs and check their general formability, LDH tests were performed using a 4 inch (101.6 mm) hemispherical punch on a hydraulic press. A Macrodyne 150/150 Ton servo-hydraulic double-action forming press was utilized (Figure 4.6). This system is computer-controlled and has an open die design. For the present work, the system was custom-fitted with 2-camera Aramis system for 3-D strain measurement. The testing and FLD determination procedures employed the well-known Hecker (or Nakazima) method (Hecker, 1974), as illustrated earlier in Figure 3.4. The Hecker method for obtaining LDH and FLD used blanks of different widths clamped with a circular-grooved lock bead.

For studying the effect of defocusing fiber laser beam welding parameters on formability, TWBs of 200 mm x 200 mm sheets from DP780/DP780 (1 mm/1 mm) were milled to obtain samples of geometries shown earlier in Figure 3.1. Specimen widths of 12.7 mm, 50.8 mm, and 76.2 mm were used to obtain the negative minor strain region of FLD, whereas widths of 127 mm were utilized to achieve plane strain mode (zero minor strain). For different strain paths of positive minor strain region of FLD (i.e., bi-axial tension side), specimen widths of 177.8 mm with different friction states; dry, Teflon film, and rubber were used at the punch-sheet interface.

Samples were arranged in such a way that the weld bottom was in contact with the hemispherical dome, with the weld centered about the middle of the die opening. A large clamping load of 100,000 lbf ($\backsim$ 445 kN) was applied between the upper and lower die to prevent the specimen from slipping between the dies during punch stretching. The stretching tests were carried out at a punch speed of 0.005 in/sec (7.62 mm/min) and the tests were stopped upon the formation of a visible neck or fracture. The dome height was then measured using punch load displacement data recorded during tests. The strain field measurements and strain mapping were carried out using the dedicated Aramis software to obtain major and minor strains in the vicinity of the neck or fracture points for the tested specimen configurations at different strain paths. The strain data was then used for constructing the FLD. The procedures followed for the determination of limit strains and constructing the FLD are explained later in Section 4.5.

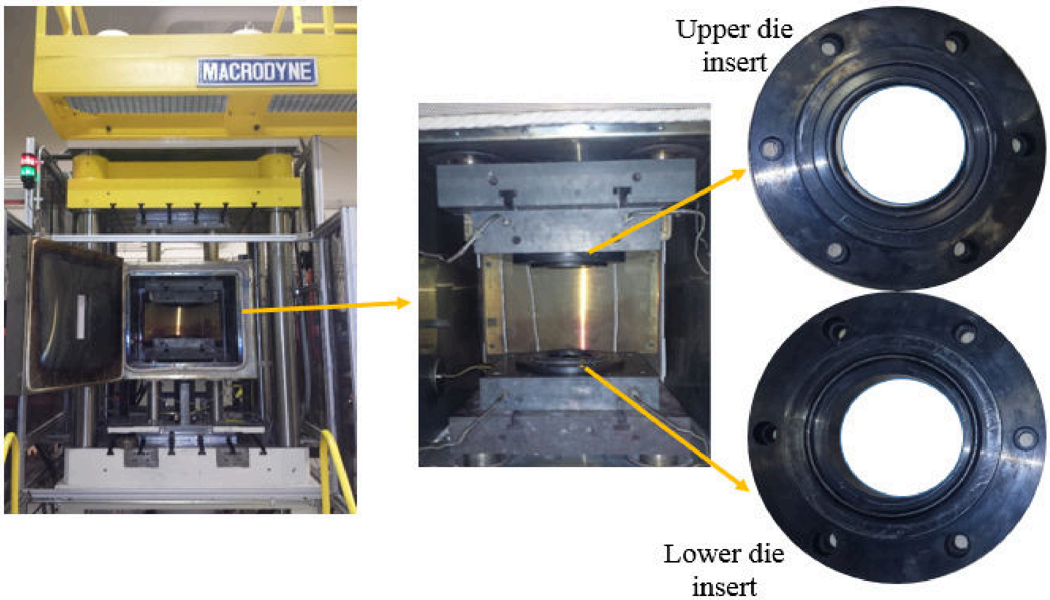

Figure 4.6. Out-of-plane hemispherical dome test setup on MACRODYNE 150/150 ton press.

4.4.1.2 In-plane plane strain (IPPS) test with double-layer TWBs

In-plane plane strain tension tests were performed with double-layer TWBs using MTS 250 kN test system (see Figure 4.7). TWBs composed of DP780/DP780 and HSLA/DP780 of thicknesses 1.5 mm/1 mm and 2.3 mm/1 mm respectively were utilized. A few different sample geometries were tested to obtain the optimum geometry at which near plane strain condition was obtained (i.e., minor principal strain was near zero).

Based on a review of the literature, a width of about six times the gauge length of the tested specimens was chosen. Samples with a geometry, shown earlier in Figure 3.2, were tested as a pair by stacking the thick gauge region of one specimen over the thin gauge section of another and spot welded together at the clamping edges (see earlier Figure 3.3). The surface of the double-layer specimen was imprinted with random dots (i.e., speckle pattern). The specimens were clamped using a 4 inch width hydraulic grips to secure a uniform distribution of the clamping load and then pulled with a uniform cross-head speed of 1 mm/min till fracture (see Figure 4.7). Aramis was deployed for online and continuous capture of the strain field in the gauge region of the specimen.

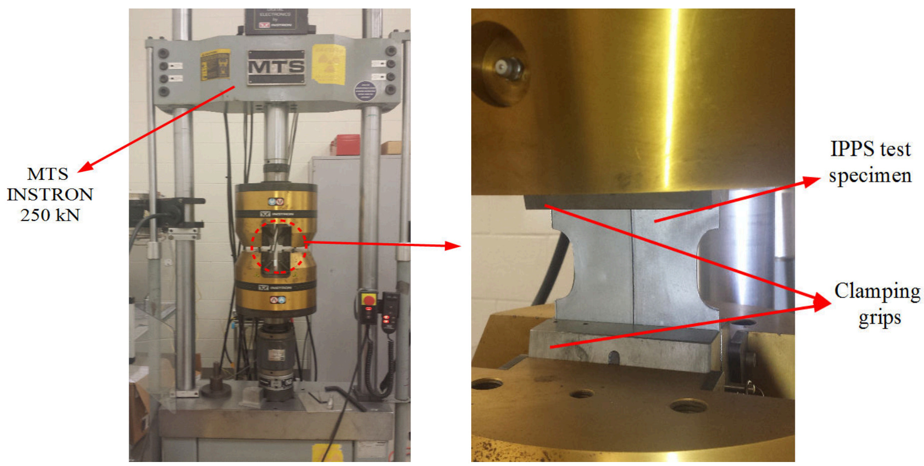

(a) (b)

Figure 4.7. In-plane plane strain (IPPS) test setup.

4.4.1.3 Out-of plane formability test with double-layer TWBs

Two stacked specimens from DP780/DP780 (1.5 mm/1 mm), and HSLA/DP780 (2.3 mm/1 mm) TWBs with the geometries shown earlier in Figure 3.1 were utilized for this test. The set of specimen geometries resulted in a range of strain paths when subjected to hemispherical punch stretching (see earlier Figure 3.4). However, the two layers of double-layer blanks were not spot welded together as in the case of IPPS as the upper and lower dies with a central circular hole and lock-beads within each die were sufficient to prevent drawing in of the blank during the hemispherical punch stretching process as well as to prevent relative sliding between the two layers. The tests were carried out using a Macrodyne 150/150 Ton servo-hydraulic double-action press. New inserts with suitable lock-beads were redesigned to modify the lock bead groove geometry to adapt to the total thickness of double-layer TWBs (see earlier Figure 4.6). A large clamping load of 100,000 lbf ($\backsim$ 445 kN) was applied between the upper and lower die to prevent the specimen from slipping between the dies during punch stretching. The stretching tests were carried out with punch speed of 0.005 in/sec (7.62 mm/min). The test was stopped upon the formation of a visible neck or fracture. The dome heights and weld line movements were measured and the strain field measurements were carried out using Aramis to obtain major and minor strains.

In addition, single-layer specimens from DP780/DP780 (1.5 mm/1 mm), and HSLA/DP780 (2.3 mm/1 mm) TWBs were tested in bi-axial strain paths. New dies inserts for this machine were also redesigned to modify the lock bead groove geometry to accommodate the thickness difference in single-layer TWBs. The results from these tests (dome height, strain field, weld line movements and fracture mode) were then compared with the corresponding results of double-layer tests to assess the forming characteristics of double-layer and single-layer methods.

4.4.2 Tensile tests of TBBs

4.4.2.1 In-situ deformation behavior of miniature steel-to-aluminum TBBs

A miniature in-situ mechanical testing jig (see earlier Figure 3.5) was designed and manufactured to use in conjunction with a high magnification digital optical microscope where a batch of digital images representing the deformation history of the samples were recorded (Figure 4.8). Miniature TBBs strips, made from Laser/MIG and CMT brazing methods, were precisely cut to small width (4.5±0.1 mm) to fit in the miniature jig grooves. Two different observation planes, long transverse (LT) and normal plane (NP), were utilized to record magnified microscope images during the test. The clamping fixtures were specially designed for this purpose (Figure 4.9).

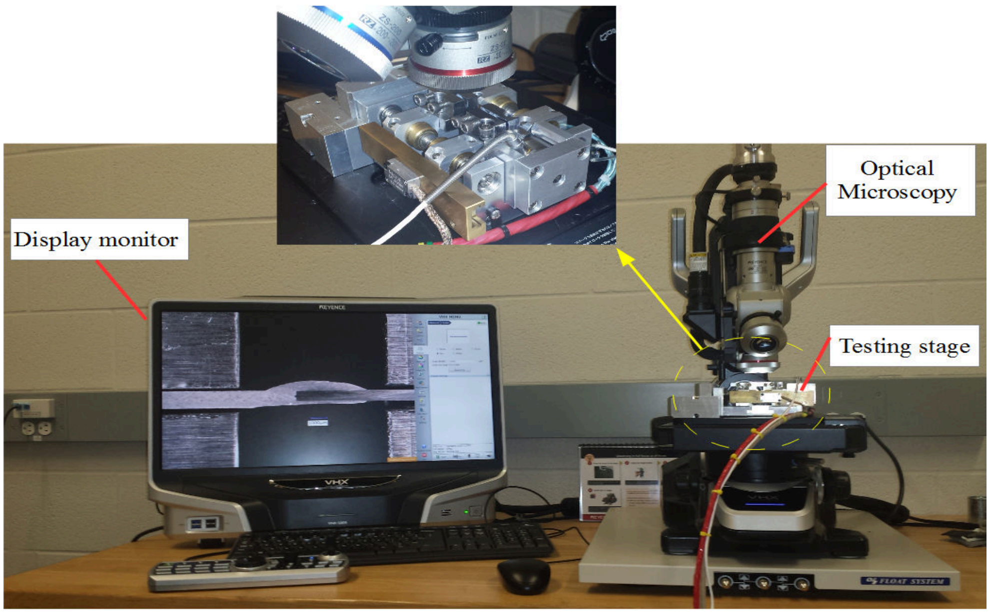

Figure 4.8. Experimental setup for testing steel-to-aluminum TBBs.

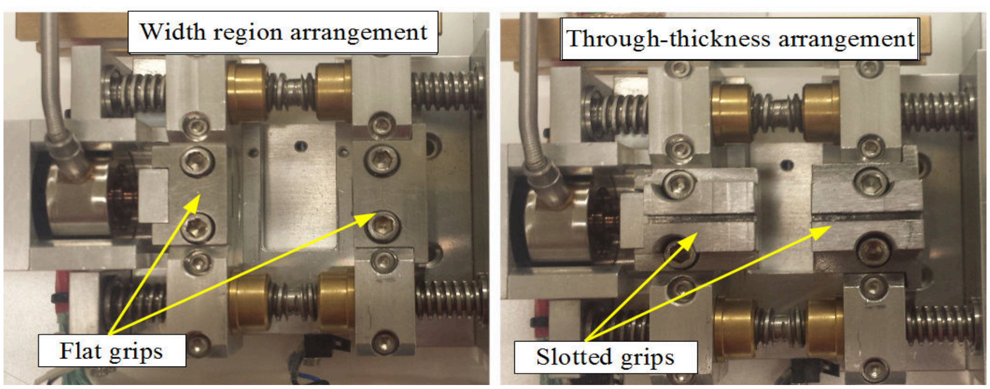

Figure 4.9. Miniature in-situ uniaxial tensile test jig setup for TBBs, through-thickness arrangement (right), and width region arrangement (left).

For specimens observed from through-thickness (LT) plane, the specimen edges were manually polished with a series of SiC papers. The polished surfaces were imprinted with a very fine-scale speckle pattern. For the specimens observed from normal plane (NP), original surfaces were imprinted with a very fine-scale speckle pattern without the need for grinding. All specimens were then tested up to failure in uniaxial tension at a pulling speed of 1 mm/min. A series of digital images representing the deformation history of the samples were recorded by the optical microscope at a magnification of 20x. The images were then imported in the Aramis software for strain mapping measurements. The very fine speckles on the surface were then used for analyzing the local plastic deformation field and its development in the vicinity of the brazed region. The load-displacement histories of the tested specimens were also recorded using a dedicated test controller and data acquisition system ©MTEST Quattro from ADMET, USA. This system is shown in Figure 4.10.

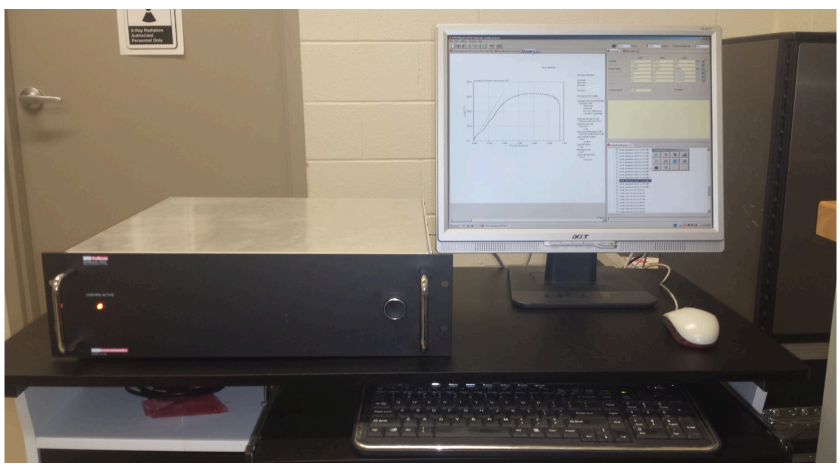

Figure 4.10. MTESTQuattro controller and data acquisition system.

4.4.2.2 In-situ deformation behavior of notched miniature steel-to-aluminum TBBs

To study the brazed interface characteristics of TBBs from the point of view of load transfer across brazed interface as well as local deformation, damage and delaminations in the brazed interface region, notched specimens were tested (see earlier Figure 3.7).

Three different specimen geometries were cut using EDM wire cutting method. The specimen geometries were specifically selected to cause failure at the brazed interface region rather than BM of the aluminum sheet. The normal plane was imprinted with a very fine-scale speckle pattern without grinding. The earlier setup shown in Figure 4.8 was utilized with the flat surface arrangement at a pulling speed of 1 mm/min. The recorded images were then imported into the Aramis software for strain mapping and to analyze the onset of instability for the three different specimen geometries.

4.5 Strain field analysis

4.5.1 Gridding

All test specimens prior to testing were prepared for post-test strain measurements by ARAMIS. This consisted of cleaning the surface of the specimens to be measured with acetone to remove contaminations to ensure good adhesion between the applied pattern and substrate specimens surface. Subsequently, a developer white water-based ink was sprayed onto the specimen surface. Finally, a random pattern of matt black water-based ink was sprayed over the dried white coat to obtain a high contrast speckle (stochastic) pattern. This is shown in Figure 4.11a.

For the miniature TBBs specimens, and due to rather small surfaces, the large size of black ink droplets at higher magnifications under the optical microscope led to poor contrast in the images from the speckle pattern. So, a very fine black toner powder was used instead the black ink to acquire high contrast large magnification images of the speckle pattern. The toner powder was mixed with ethanol and sprayed over the dried white coat using air brush. After the evaporation of ethanol, very fine black toner powder stuck to the dry white coat due to static resulting in a high contrast speckle pattern. Figure 4.11b shows this speckle pattern on the through-thickness surface of the brazed area of TBBs at a magnification of 100x.

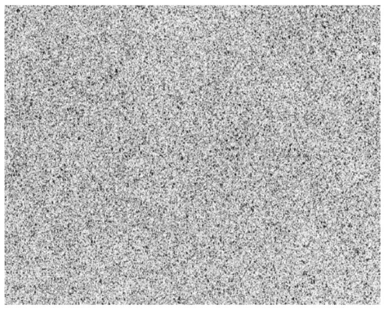

(a)

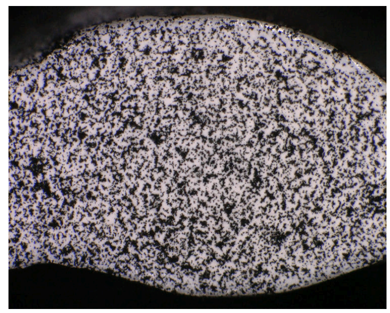

(b)

Figure 4.11. Images of speckle pattern obtained by (a) water-based black ink for large surfaces (magnification=1x), and (b) ethanol-based very fine black toner powder (magnification=100x).

4.5.2 Strain field measurements using Aramis

Aramis®, from GOM Company, is a full-field on-line strain measurement system based on the DIC method. The system consists of high resolution CCD cameras (2 cameras for 3D imaging), a high-performance computer system, sensor controller for the cameras to control image recording. The images were processed using Aramis software (see Figure 4.12a). The surface of the deforming specimen was initially applied with a speckle pattern as described earlier. The pattern was recorded during the test using CCD cameras. The images were then converted to gray scale images. A gray scale is a digital image in which the value of each pixel is a single sample. This non-contact technique tracks the gray level change of the speckles in small rectangular area or facet during deformation at regular intervals. Change in the intensity of the speckle pattern during deformation reflects a change in the pixel intensity, i.e., the gray scale values.

The distribution of gray scale values of a facet in the un-deformed state corresponds to the distribution of gray scale values of the same area in the deformed state (Figure 4.12b).

A dedicated DIC software with the Aramis system converted the displacement of the random dots to a change in pixel intensity of the gray scale and then to a displacement vector field. By analyzing the displacement vectors within the entire image, a good correlation in each window corresponding to the actual displacement of the pattern was obtained. Further, by comparing the facets in the current image with those of the previous image, the shift, rotation and distortion of the facets could be calculated, so that the incremental and total strain could be obtained (Figure 4.12b (Ganesh, 2015)).

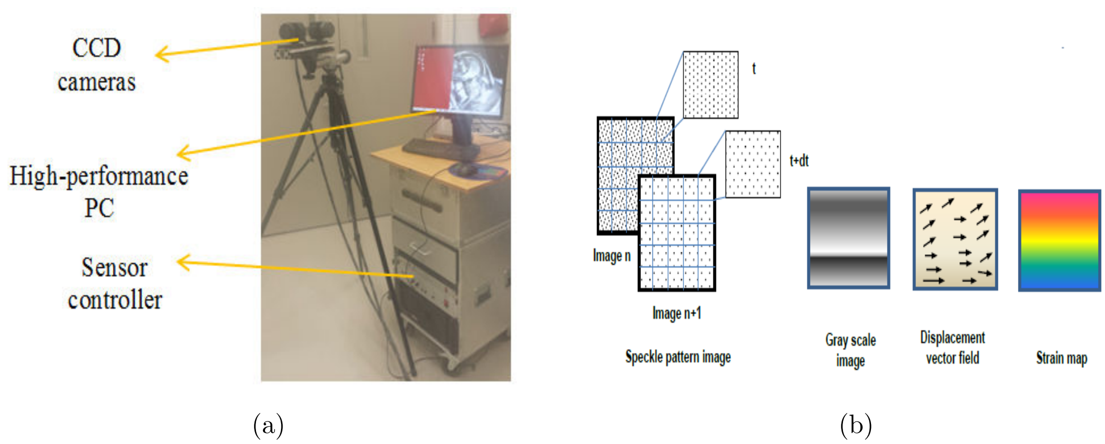

Figure 4.12. An illustration of Aramis on-line strain measurement, (a) system components, and (b) DIC methodology for strain measurement.

4.5.3 Determination of forming limits (limit strains) for FLC

For determining the limit strains or principal strain pairs at the onset of necking of the deformed specimen, a new time-dependent method (or t-d method), developed by Martínez-Donaire *et al.* (2014), was utilized. The on-line measure of strains on the surface of the deformed specimen using Aramis provided a complete history of strain at temporal and spatial scales in the necking zone and its vicinity. In the t-d method, temporal evolution of major strain and major strain rate at a series of aligned points in section perpendicular to the fracture zone on the surface of specimen were measured (see Figure 4.13 and 4.14). The instability region width (boundary of the necking zone) was identified such that the major strain of points (e.g., point A and B in Figure 4.14) within this region increased until fracture. In contrast, the major strain was reduced till it ceased for point out side this region (e.g., point C in Figure 4.14). Then the boundary of the necking region was taken to be the first point in vicinity of this region that the major strain ceased and the strain rate reached zero just before the fracture occurred (see Figure 4.14). The time, t^*, corresponding to the maximum value of strain rate for point at the boundary of necking zone (point C) was determined and identified as the time for onset of localized instability (or necking). For determination of the major limit strain, major strain history of the fracture point (point of the highest major strain e.g., point A) was measured. Then, major and minor strain values corresponding to t^* were identified as initial limit strains. The final limit strain was the average value of the limit strains determined in three adjacent sections perpendicular to the necking region as shown in Figure 4.13.

For constructing the FLC, a curve was drawn using the drawing software Autocad such that it best fitted the limit strain points. After that, the drawn curve was digitized to receive several points. The coordinates of these points, (i.e., the major and corresponding minor strains), were imported into excel file for constructing the final FLC.

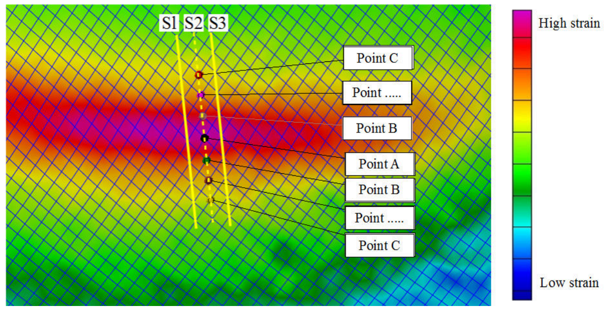

Figure 4.13. Major strain mapping of necking zone just before fracture stage.

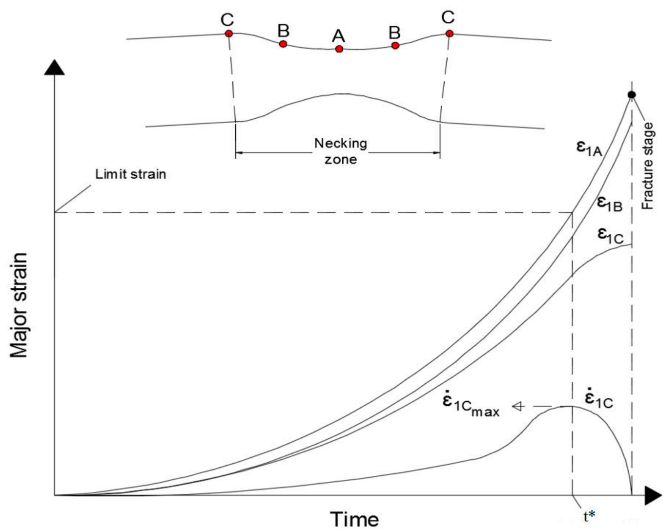

Figure 4.14. Schematic drawing of time-dependent methodology [modified from: (Martínez-Donaire *et al.*, 2014)].

4.6 Summary

The research methodology described in this chapter utilized emerging joining techniques to produce steel-to-steel TWBs and steel-to-aluminum TBBs. These consisted of defocused fiber laser beam welding, Laser/MIG hybrid and CMT brazing methods. A conventional formability test was used to study the effect of using defocusing fiber laser beam welding technique on the deformation behavior of TWBs incorporated AHSS.

Also, a new formability test was devised and used to assess formability of TWBs that incorporated different strength and thickness combinations. With regard to TBBs from both Laser/MIG hybrid and CMT brazing methods, specialized miniature mechanical tests was designed, developed and utilized to understand the local deformation behavior at the brazed steel-aluminum interface using an advanced digital optical microscope and well-controlled tensile stage. A 2-camera Aramis system was extensively used for strain mapping and analysis of limit strains and other characteristics of flow and formability from various test specimens.

Chapter 5

Results and Discussion

In the following, the results obtained in the current research are presented. This chapter is divided into four main sections. The first section examines characteristics of the parent materials individually and the tailor blanks in terms of standard mechanical properties, microstructures and hardness profiles. The next section presents the forming limits of TWBs produced by defocused fiber laser beam welding techniques. The third section describes the deformation behavior of double-layer TWBs in both in-plane and out-of-plane formability tests. The final section presents the local deformation of the brazed interface regions of TBBs produced by Laser/MIG and CMT brazing methods using uniaxial tensile tests.

5.1 Tailor blanks (TBs)

The parent sheet material combinations that were utilized to produce TBs are listed in Table 5.1. For steel-to-steel TWBs, the full weld penetration (keyhole formation) was achieved using defocuced fiber laser beam welding with parameters that were listed earlier in Table 4.3 (Chapter 4). For steel-to-aluminum TBBs, the wetting of the steel substrates by the melted aluminum from both aluminum filler wire and base aluminum sheet was obtained using laser/MIG hybrid brazing and CMT brazing. The brazing parameters were also listed in the earlier Table 4.3.

Table 5.1. Welded and brazed combinations of TWBs and TBBs.

Joint type	Material combinations	Thickness combinations (mm/mm)
TWBs	DP780/DP780	1/1
	DP780/DP780	1.5/1
	HSLA/DP780	2.3/1
TBBs	AA2024/DP780	1.27/1

5.2 Material characterization

5.2.1 Uniaxial tensile properties

Samples of parent sheet materials were tested in uniaxial tension along the rolling direction. The engineering stress-engineering strain curves for the materials are shown in Figure 5.1. A distinct yield region is observed in AA2024. For HSLA, a significant yield point elongation with the formation of Luder bands is observed during tensile testing. DP780 steel, however, exhibits a gradual and continuous transition from elastic to plastic deformation. The 0.2% offset strain method was utilized to obtain the YS of the DP780 steel and AA2024 aluminum. The strain hardening coefficient (n), and strength coefficient (K), were identified by fitting the experimental true stress-true strain curves to Hollomon equation (also known as power law). The various mechanical tensile properties are presented in Table 5.2.

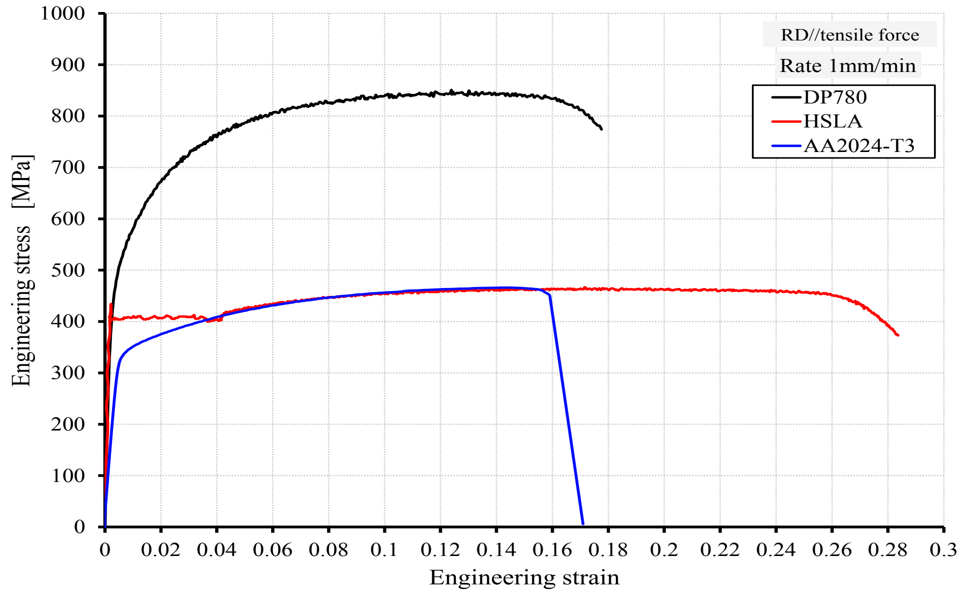

Figure 5.1. Engineering stress-engineering strain diagrams of parent materials of DP780, HSLA and AA2024-T3.

Table 5.2. Average mechanical properties of parent materials

Material	YS (MPa)	UTS (MPa)	K (MPa)	n -	Uniform elongation (%)	Total elongation (%)
DP780 (1mm)	497	851	1441	0.19	12.4	17.76
HSLA (2.3mm)	417	463	744	0.17	14.39	29.09
AA2024-T3 (1.27mm)	334	466	736	0.16	14.4	15.91

For the welded samples, tests were performed with weld line perpendicular to tensile axis (referred to as transverse direction). The transverse tensile tests were used to check robustness of the weld, i.e., to ensure that no cracks formed in the fusion zone (or FZ) before the specimen failure occurred in the thinner or weaker material due to straining.

Figure 5.2 shows the engineering stress-engineering strain diagram for the steel-to-steel TWBs. It was noted that the failure always occurred in the weaker or thinner material and the behavior of welded test specimens was quite similar to the behavior of the weaker or thinner of the two parent materials. This was because there was small plastic deformation of the stronger or thicker sheet side and most of the deformation was confined to the weaker or thinner sheet (see Figure 5.3a). For example, by comparing the engineering stress-strain curve of HSLA/DP780 TWB of thickness combination 2.3mm/1mm in Figure 5.2 with the corresponding curves of DP780 and HSLA parent materials in Figure 5.1, one can clearly see that the UTS value for HSLA/DP780 of 2.3mm/1mm combination is quite similar to that of DP780 parent sheet. The total elongation, on the other hand, depends on how the deformation of each of the parent materials on both side of the weld and the weld itself contributes to the total deformation, as well as the thickness ratio between the parent materials on both side of the TWB. The contribution of the weld regions to the total deformation depends on the width and strength of fusion zone (FZ) and the heat affected zone (HAZ). In addition, the total deformation of the TWB specimen decreases with increase in the thickness ratio between the parent materials on both side of the TWB, i.e., for identical guage and strength combination such as DP780/DP780 1mm/1mm, deformation occurred on both sides of the weld line (Figure 5.3b), and the total elongation was nearly similar to that of DP780 parent material which indicates the marginal effect of defocused laser beam welding process on the stress-strain response of the TWB (further details and explanations concerning the effect of defocused laser beam welding process are presented in Section 5.3). On the other hand, in case of unequal thickness and/or strength, such as DP780/DP780 1.5mm/1mm and HSLA/DP780 of 2.3mm/1mm combinations, the deformation was confined to the thinner sheet side (Figure 5.3a), and the total elongation decreased with increase in the thickness ratio. The total elongation was typically much lower than each of the parent materials of the TWBs (see Figure 5.2).

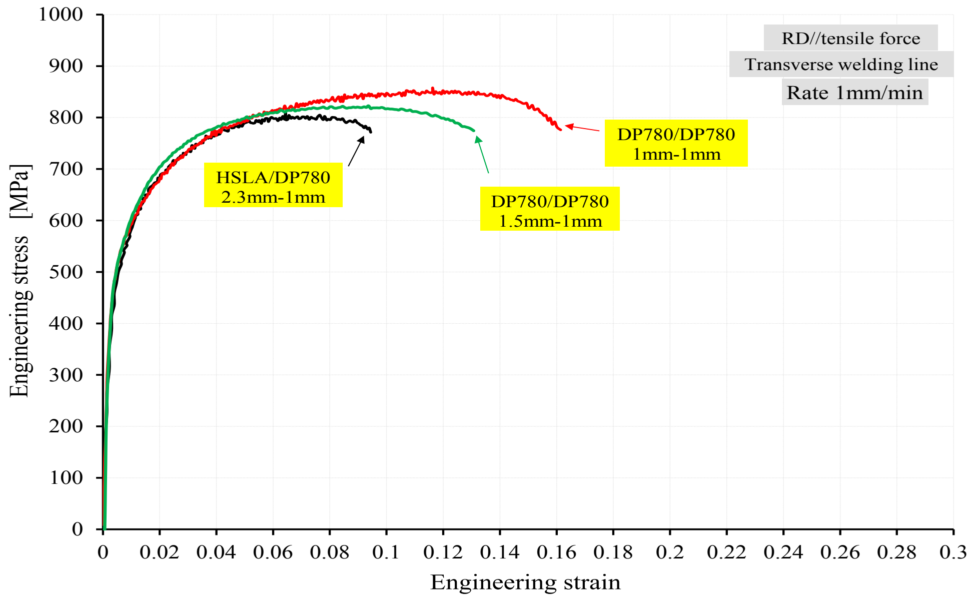

Figure 5.2. Engineering stress-engineering strain diagrams of steel-to-steel TWBs of different thickness and material combinations.

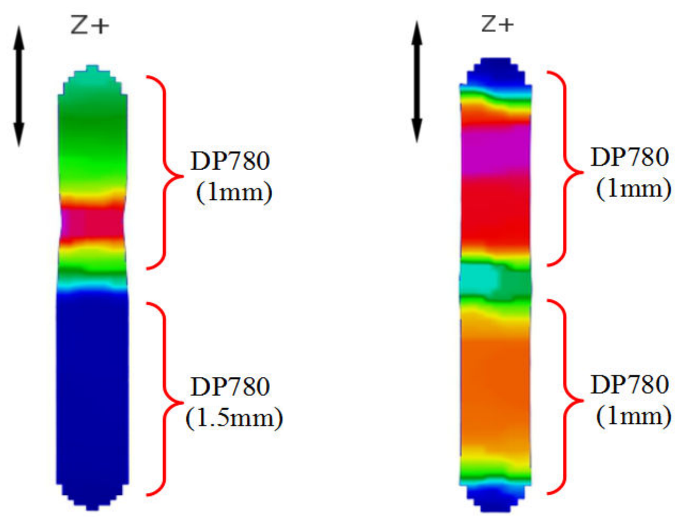

(a) Thickness ratio=1.5. (b) Thickness ratio=1.

Figure 5.3. Comparison of major strain distribution for uniaxial tensile specimens of DP780/DP780 TWBs of (a) 1.5 mm/1 mm thickness combination, and (b) 1 mm/1 mm thickness combination.

For the steel-to-aluminum TBBs produced by Laser/MIG hybrid and CMT brazing methods, tensile tests were conducted on a series of visually sound specimens to check the fracture location and mechanical properties of the produced TBBs. The results of this test and the corresponding discussion are presented later in Section 5.5.

5.2.2 Microstructure examination

The metallographic examinations on the cross section of TBs were performed to check the quality of steel-to-steel TWBs and steel-to-aluminum TBBs.

For steel-to-steel TWBs, Figure 5.4 presents the typical through-thickness microstructure of different weld zones of DP780/DP780 1 mm/1 mm, DP780/DP780 1.5 mm/1 mm, and HSLA/DP780 2.3 mm/1 mm TWBs, respectively. For all TWBs configurations, both sheets were melted and the weld shows a full penetration in TWBs with no cracks or porosity present.

Figure 5.5 reveals the microstructure of the weld side of DP780 and HSLA (upper two images), and the magnified images for their HAZ (bottom two images). The microstructural differences in HAZ for both DP780 and HSLA sides of the weld arises from differences in microstructures and chemical compositions of their base materials as well as welding parameters and cooling rates.

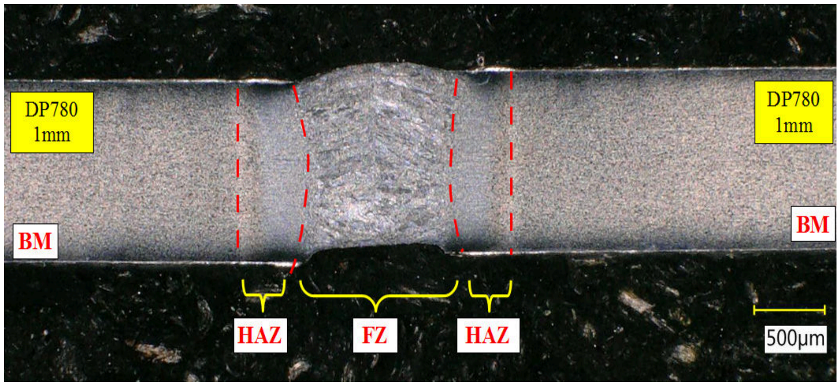

(a) DP780/DP780 1 mm/1 mm TWBs.

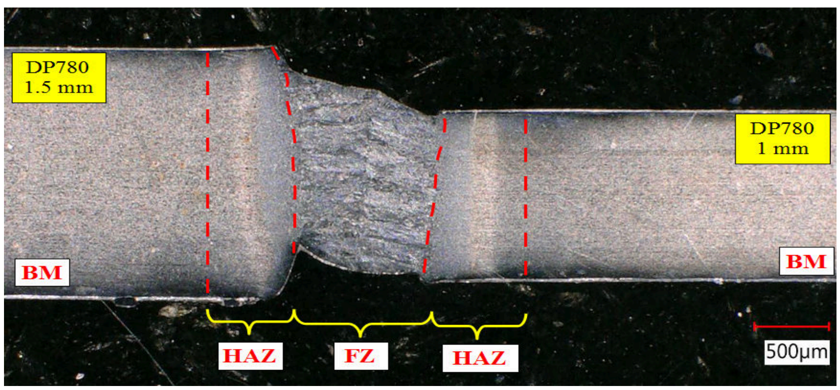

(b) DP780/DP780 1.5 mm/1 mm TWBs.

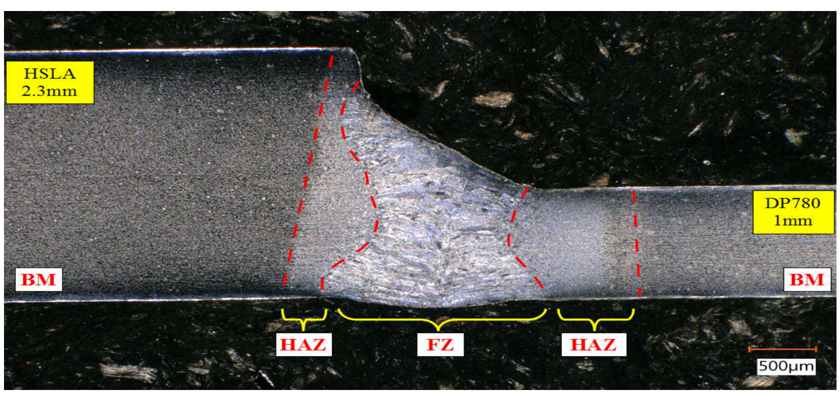

(c) HSLA/DP780 2.3 mm/1 mm TWBs.

Figure 5.4. Through-thickness welds optical micro-graphs for (a) DP780/DP780 1 mm/1 mm TWBs, (b) DP780/DP780 1.5 mm/1 mm TWBs, and (c) HSLA/DP780 2.3 mm/1 mm TWBs.

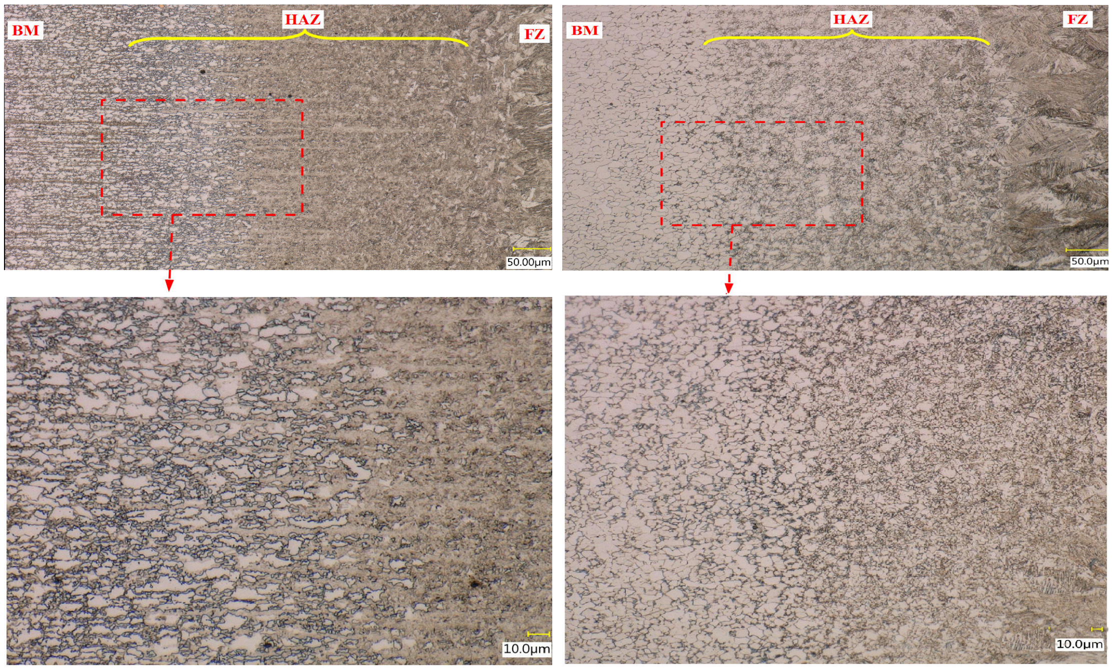

(a) DP780 weld side. (b) HSLA weld side.

Figure 5.5. Through-thickness optical micro-graphs of weld zones (upper), and magnified images for HAZ (bottom) of HSLA/DP780 2.3 mm/1 mm TWB for (a) DP780, and (b) HSLA weld sides.

The microstructure of the HAZ on HSLA side consists of tempered zone at the edge of the HAZ adjacent to the unaffected BM, the refined grains in the recrystallized zone, and grain coarsening region near the fusion boundary. For the HAZ on DP780 side, due to the microstructure of BM (ferrite grains and martensite islands) as well as the peak temperature experienced by the workpiece during the welding and the subsequent rapid cooling after fiber laser welding, the HAZ is composed of three subregions. These correspond to supercritical (UC) HAZ in the vicinity of fusion boundary (mainly martensite), intercritical (IC) HAZ (refined grain area of fine martensite grains in ferrite matrix), and subcritical (SC) HAZ (tempered zone) adjacent to the unaffected BM. In the latter case, part of martensite phase of the BM could be tempered, causing a hardness drop (or softening) compared to that of BM based on heat input during welding (see Figure 5.6).

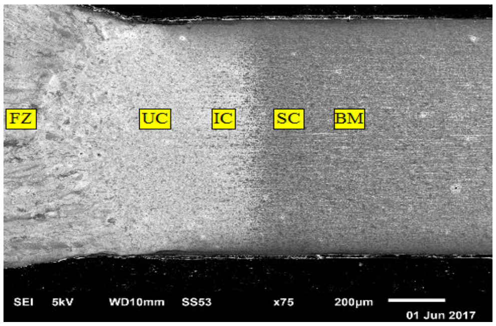

(a) DP780 side weld zones.

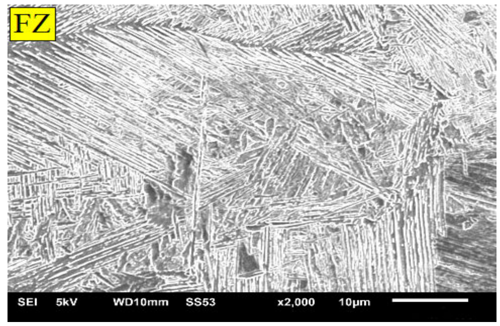

(b) Fusion zone.

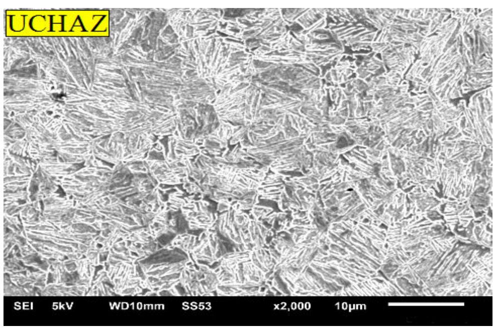

(c) Supercritical HAZ.

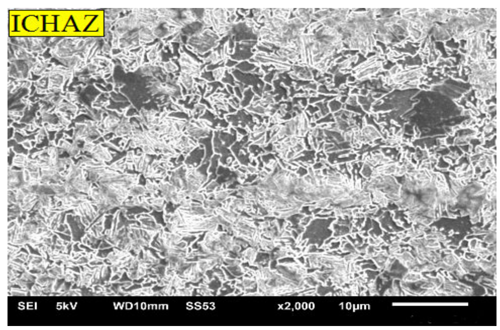

(d) Intercritical HAZ.

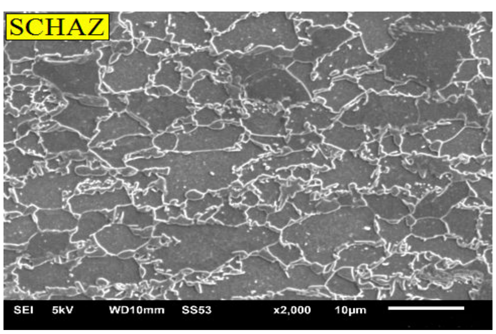

(e) Subcritical HAZ.

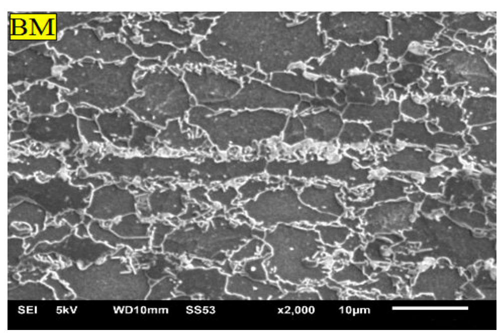

(f) Base material.

Figure 5.6. SEM images of through-thickness microstructure of different weld zones on DP780 side of HSLA/DP780 2.3 mm/1 mm TWB; (a) overall view of DP780 weld side zones, (b) fusion zone (FZ), (c) supercritical HAZ (UCHAZ), (d) intercritical HAZ (ICHAZ), (e) subcritical HAZ (SCHAZ), and (f) Base material (BM).

The width of FZ and HAZ as well as their microstructures, are controlled by the welding parameters, mainly the amount of heat input during the welding process and the cooling rates. The average widths of the FZ, as measured optically for different TWB specimens of DP780/DP780 1 mm/1 mm, DP780/DP780 1.5 mm/1 mm, and HSLA/DP780 2.3 mm/1 mm, were 0.93 mm, 1.02 mm, and 0.95 mm, respectively. Whereas, the average width of the HAZ with the subregions on both sides of the weld was about 0.6∽0.85 mm for the three TWBs configurations. Table 5.3 lists the average width of the FZ and HAZ of the three TWB configurations.

Table 5.3. The average width of the FZ and HAZ with the subregions as measured optically for different TWB configurations.

		HAZ with subregions (mm)	
TWBs	FZ (mm)	Thicker sheet side	Thinner sheet side
DP780/DP780 (1 mm/1 mm)	0.93	0.7	0.7
DP780/DP780 (1.5 mm/1 mm)	1.02	0.8	0.85
HSLA/DP780 (2.3 mm/1 mm)	0.95	0.6	0.8

It was reported that the mechanical performance of the TWB depends on the width of the FZ and area in its vicinity (i.e., HAZ). In general, better mechanical performance can be obtained from the TWBs with minimum width of welding zones (i.e., FZ and HAZ) especially if the parent material is affected by the welding process as in case of DP steels. In the current research, the average width of HAZ, including subregions, of DP780 was about 0.8 mm which is less than the thickness of the DP780 parent sheet (1 mm). In other words, the width of the softening zone (tempered region) of HAZ, if it exists, was less than DP sheet thickness. Therefore, the transverse plastic flow of softening zone is likely to be confined and constrained by stronger surrounding areas and consequently, the strength of the TWB may increase and reach that of the parent materials (see earlier Section 2.4.2). The level of softening occurred was identified by hardness profiles, as discussed later in section 5.2.3.

For steel-to-aluminum TBBs, Figure 5.7 shows the profile of the brazed region of AA2024/DP780 1.27 mm/1 mm TBBs made by Laser/MIG hybrid and CMT brazing methods. No cracks were observed and only aluminum sheet and filler wire were melted and wetted the steel substrate. The microstructures revealed good adhesion at the faying surfaces for both brazing methods. However, better transition was observed between the brazing area and the steel substrate at the end of wetting lengths for CMT TBBs specimens compared to Laser/MIG TBBs specimens (as shown by the dashed circles in Figure 5.8). In addition, more pores were observed in the brazing area (weld seam) of Laser/MIG TBBs specimens than CMT TBBs specimens. This may be attributed to the higher evaporation rate of lower melting point elements and zinc coating layer during Laser/MIG brazing process than in CMT brazing. It is to be noted that, for Laser/MIG process, wetting of steel substrate with molten aluminum occurred during fusion from both laser beam and MIG arcing (i.e., continuous heat input). In contrast, wetting in CMT brazing cycles occurred at the moment of short-circuit or off-arcing (i.e., with minimum heat input) (see earlier Section 2.2.3).

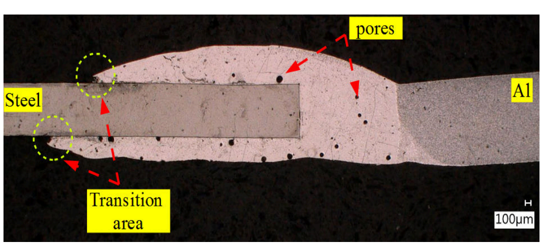

(a) Laser/MIG hybrid brazing.

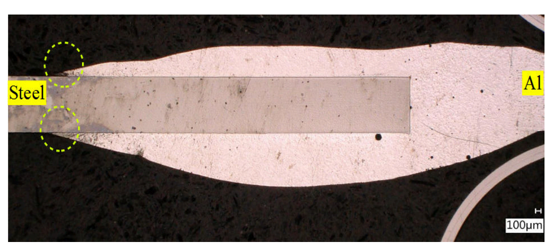

(b) CMT brazing.

Figure 5.7. Macrograph of brazed joint cross-section of AA2024/DP780 1.27 mm/1 mm TBBs for (a) Laser/MIG hybrid brazing, and (b) CMT brazing.

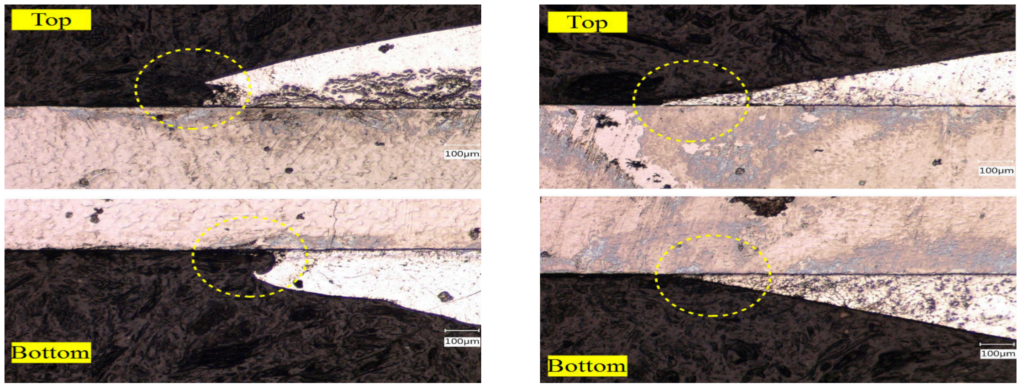

(a) Laser/MIG hybrid brazing. (b) CMT brazing.

Figure 5.8. Magnified macrograph of the top and bottom transition region between brazing area and steel substrate in brazed joint of AA2024/DP780 1.27 mm/1 mm TBBs for Laser/MIG hybrid brazing (left), and CMT brazing (right).

The microstructures allowed measurement of the average upper and lower wetting lengths as well as the average thicknesses of the IMCs layer. The average upper and lower wetting lengths were almost the same for the CMT brazed specimens and larger compared to that of Laser/MIG brazed specimens. With respect to the average thickness of the IMC layer, both brazing methods yielded quite uniform layer thickness with values lower than the critical value of 10 µm reported in the literature below which good tensile properties could be achieved (see earlier Section 2.5). For Laser/MIG brazed specimens, the average thickness of the IMC layer at the upper, lower, and side faying surfaces (Figure 5.9b, c, and d) respectively, were higher than the corresponding IMC layer thicknesses of specimens made by CMT brazing method (Figure 5.9e, f, and g). It was reported that the formation of IMCs layer and its thickness is mostly related to the amount of heat input during wetting process, which was different for both Laser/MIG and CMT methods as discussed above. The average thicknesses of IMCs and the average wetting lengths of TBBs specimens from Laser/MIG hybrid and CMT brazing methods are presented in Table 5.4.

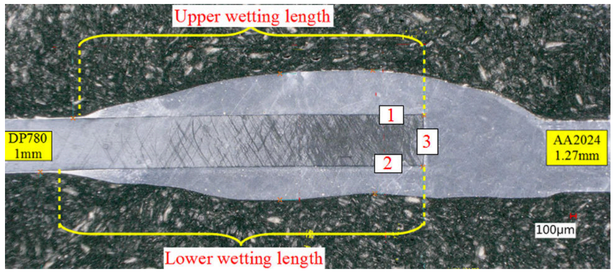

(a) AA2024/DP780 1.27 mm/1 mm TBBs.

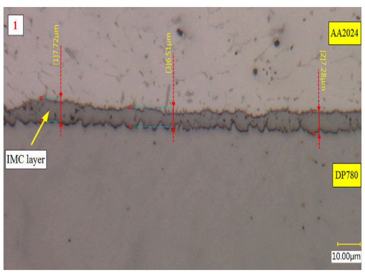

(b) Upper

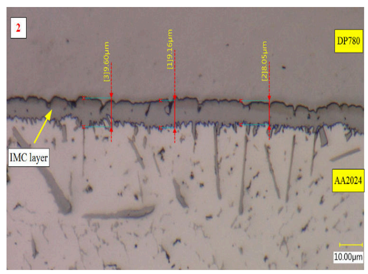

(c) Lower

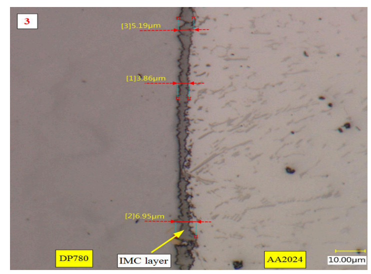

(d) Side

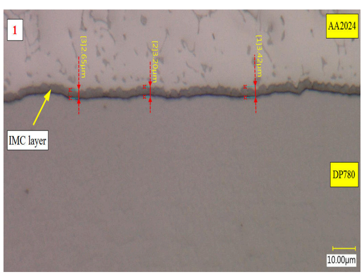

(e) Upper

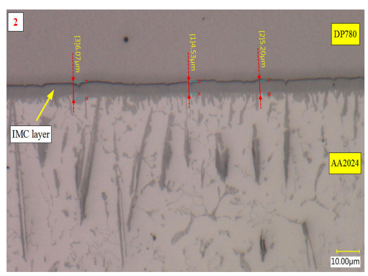

(f) Lower

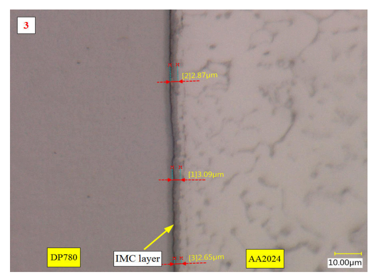

(g) Side

Figure 5.9. Micrograph of upper, lower, and side faying surfaces with IMCs layer for Laser/MIG hybrid brazing method (b, c, and d), and CMT brazing method (e, f, and g), respectively.

Table 5.4. Comparison between the average thicknesses of IMCs layer and the average wetting lengths for Laser/MIG hybrid and CMT brazed specimens.

	Thickness of IMCs (μm)			Wetting length (mm)	
	Upper	Lower	Side	Upper	Lower
Laser/MIG	7	8	5	4	4.5
CMT	3	5	3	6	6

5.2.3 Microhardness measurements

Microhardness measurements were carried out in the through-thickness direction of steel-to-steel TWBs and steel-to-aluminum TBBs. So, the local properties of the welded zones (FZ, HAZ and BM) were obtained and compared. The microhardness distributions were taken as the average of 2 indentation line profiles across the weld cross-section.

For steel-to-steel TWBs, Figures 5.10, 5.11, and 5.12 present the microhardness profiles of DP780/DP780 1 mm/1 mm, DP780/DP780 1.5 mm/1 mm, and HSLA/DP780 2.3 mm/1 mm respectively. The FZ for the three TWBs configurations showed higher hardness values compared to that of HAZ and BM. This was due to the formation of mostly martensitic structure resulting from the higher cooling rate experienced during solidification of the FZ after fiber laser welding. In the HAZ, at the outside boundaries of the FZ, the hardness values decreased till it merged with BM hardness profile at the outskirt of HAZ. Difference in hardness values in HAZ has been related to the microstructure transformations that occurs according to the peak temperature reached locally based on distance from the FZ boundary. The base metal microstructure transformed to austenite during heating and then it transformed to martensite as per the cooling rate. The degree of transformation and the volume fraction of martensite within HAZ after cooling depend on the peak temperature reached locally and the value of this temperature compared to the critical temperatures Ac_1 and Ac_3 (see earlier Section 2.3). In addition, no significant softening or hardness drop was observed in the HAZ. However, very slight hardness drop was noted in the HAZ of DP side of HSLA/DP780 2.3 mm/1 mm due to decrease in welding speed to 4.5 m/min that resulted in more heat input to the specimen. No softening in the HAZ was observed on the HSLA side. Also, the hardness values in BM of DP780 were higher than that of HSLA due to the microstructures of DP steel which contains hard martensite phase. Therefore, DP780/DP780 TWBs showed lower hardness difference, difference between FZ and BM harness values, which could improve the stretchability of DP TWBs as discussed later in this chapter.

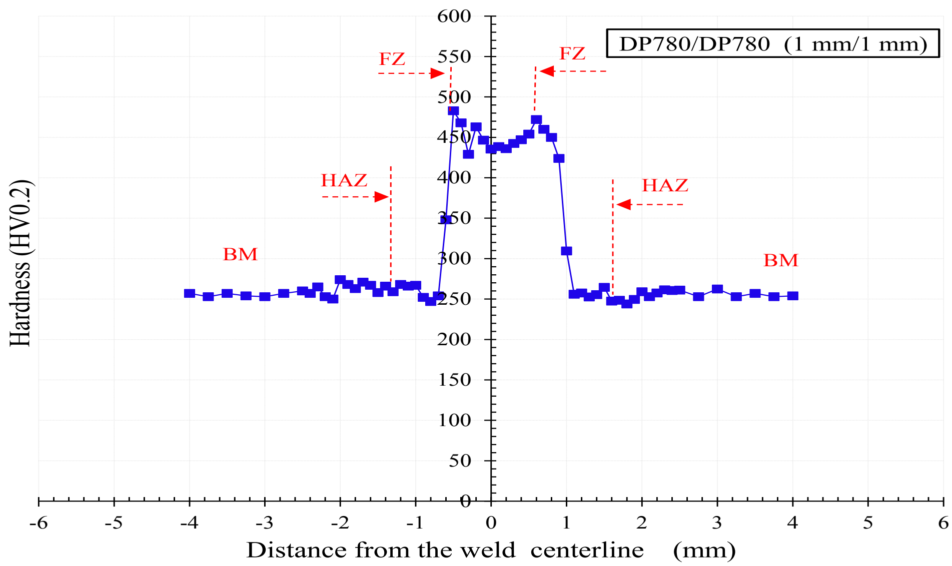

Figure 5.10. Hardness profile along through-thickness surface of DP780/DP780 1 mm/1 mm TWBs.

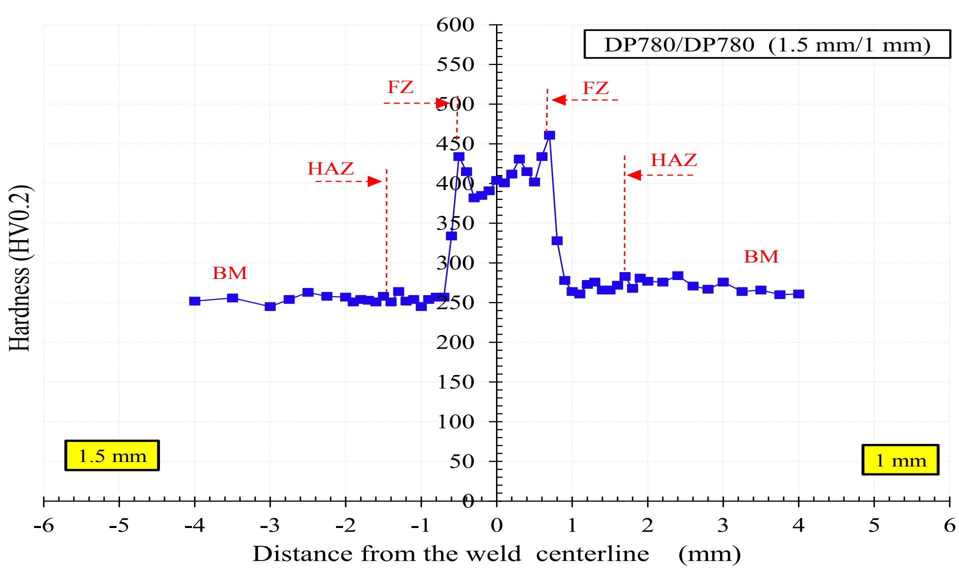

Figure 5.11. Hardness profile along through-thickness surface of DP780/DP780 1.5 mm/1 mm TWBs.

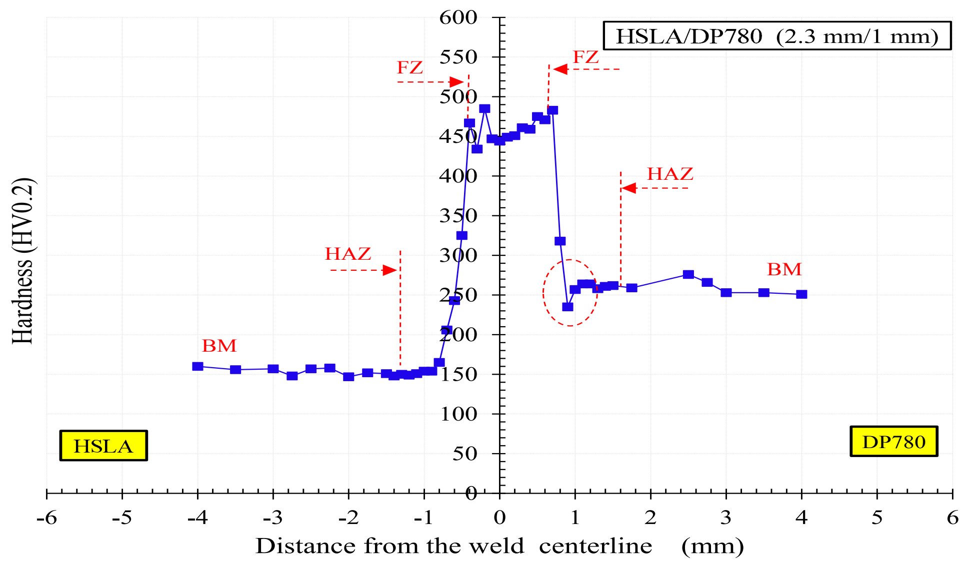

Figure 5.12. Hardness profile along through-thickness surface of HSLA/DP780 2.3 mm/1 mm TWBs.

For steel-to-aluminum TBBs, Figures 5.13 and 5.14 present the microhardness profiles of AA2024/DP780 1.27 mm/1 mm TBBs made by Laser/MIG and CMT brazing methods respectively. The DP steel side showed considerably higher hardness values in the region adjacent to the aluminum/steel interface for both brazing methods. Hardness profile then decreased gradually until it merged with that of BM of DP steel. For the aluminum side, the weld seam, adjacent to the aluminum/steel interface, showed lower hardness values compared to that of aluminum BM as it transformed to cast structure during solidification after brazing process for both brazing methods (see earlier Section 2.3). A significant drop of hardness values was observed in the region adjacent to weld seam in aluminum BM for Laser/MIG TBBs specimens (Figure 5.13). This may be attributed to the effect of heat input during hybrid brazing which may have caused partial annealing in this region and resulted in hardness drop (see earlier Section 2.3.2). Consequently, stress concentration mostly occurs in this region during subsequent forming process as presented later in this chapter. In contrast, CMT TBBs specimens did not show any hardness drop in aluminum BM. The hardness values increased gradually from weld seam boundary till it merged with that of aluminum BM.

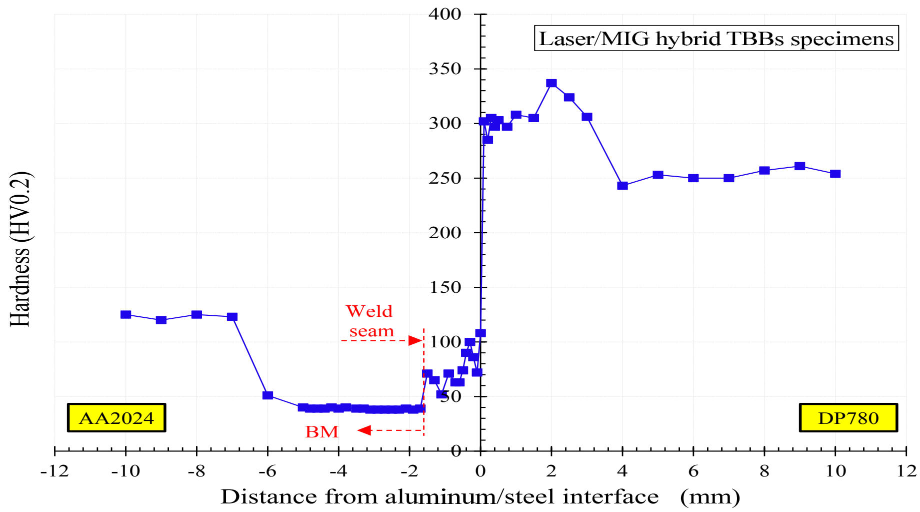

Figure 5.13. Hardness profile along through-thickness surface of AA2024/DP780 1.27 mm/1 mm TBBs made by Laser/MIG hybrid brazing.

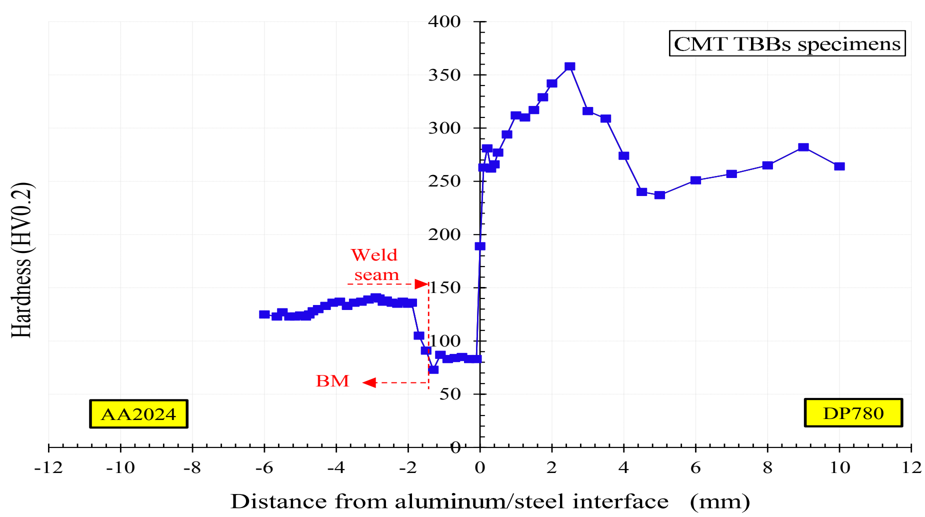

Figure 5.14. Hardness profile along through-thickness surface of AA2024/DP780 1.27 mm/1 mm TBBs made by CMT brazing.

From the microhardness results, it can be said that using defocused fiber laser beam welding can be used to decrease the softening that occurs during welding of steel-to-steel TWBs incorporate DP steel, as defocused fiber laser beam decreases the amount of heat input during the welding process. It is to be noted that the effect of thickness difference within TWB on the degree of softening in the BM has not been reported in the literature. It is also out of the scope of the current research. With respect to steel-to-aluminum TBBs, Laser/MIG and CMT brazing methods were used to decrease the thickness of IMCs layer of TBBs as discussed in Section 5.2.2. However, the mechanical properties of aluminum BM adjacent to the brazing area can be affected by the amount of heat input during the brazing process.

5.3 Effect of defocused fiber laser welding on formability of DP780 TWBs

5.3.1 Effect on failure location

Figure 5.15 shows the fractured DP780/DP780 1 mm/1 mm TWBs specimen after the uniaxial tensile test. It was noted that fracture occurred in BM away from the HAZ. The results from uniaxial tensile tests (i.e., fracture location and total elongation) provided clear indication that no deformation localization (visible necking) occurred in the softening area of the HAZ. The softening area has a lower strength than the FZ, unsoftening areas of the HAZ, and BM and causes a reduction in the total elongation of TWBs. In the current research, however, fracture occurred in the BM, and the strengths (yield and ultimate) of both DP780 TWB and DP780 parent materials were nearly matched, while a slight difference in the total elongation was observed (see Figure 5.16). This may be attributed to the constraint effect which means that the plastic deformation of softening zone was curbed or constrained by the embracing zones with higher strength. In other words, the strength of the TWB increases with decreasing width of softening zone and this strength may reach the strength of BM (see earlier Section 2.4.2).

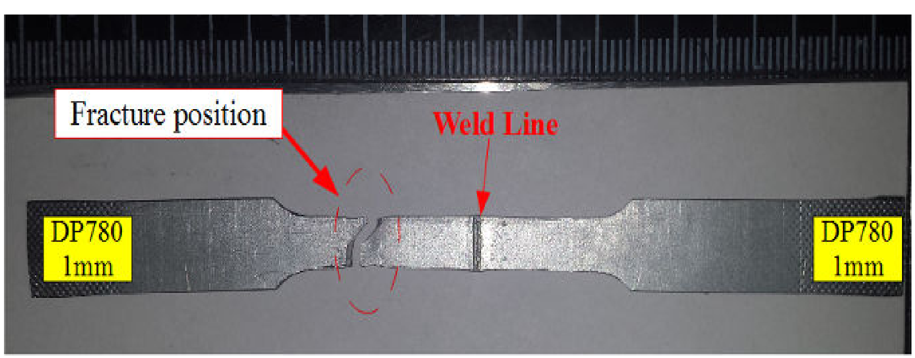

Figure 5.15. Fractured specimen from uniaxial tensile test of DP780/DP780 1 mm/1 mm TWBs.

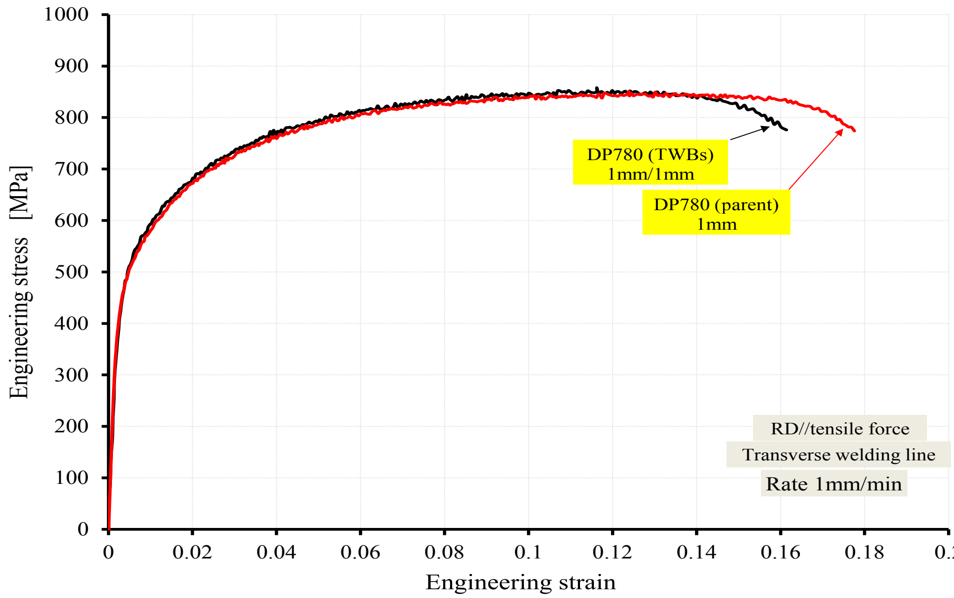

Figure 5.16. Comparison between engineering stress-strain curves of DP780/DP780 1 mm/1 mm TWB and DP780 1 mm parent material.

Further experiments were conducted using out-of-plane hemispherical punch stretching test under different strain paths and lubricant conditions to check the fracture locations in different forming modes. Figure 5.17 shows different dome-shaped fractured specimens of DP780 TWBs and the corresponding DP780 parent material. In DP780 TWBs specimens, it was noted that the fracture occurred at locations away from the softening zone and it was similar to the fracture locations in each corresponding specimen of parent materials. For full size 177.8 mm biaxial TWBs specimens, the fracture orientation was across the weld line at the pole (center of the dome) for rubber and teflon lubricant conditions (Figure 5.17a, and c), and it was shifted away from the pole in dry condition (Figure 5.17e). Moreover, in all full size biaxial specimens under all lubricant conditions (rubber, Teflon and dry), fracture initiated at the weld (FZ) and the crack propagated towards the BM through the HAZ on both sides of TWBs and perpendicular to the weld line. This was largely because of the hard and brittle martensitic phase microstructure of FZ and supercritical HAZ. These zones have the highest strength and lowest deformation within the TWB and prone to fracture initiation. The major strain distributions measured at the sections shown in Figure 5.18, along the weld line and at the fracture location across the weld line, are presented in Figure 5.19. The results show that there was no strain localization in the softening zone, and at the fracture stage, the strain concentrated at point on weld line (FZ) as seen in Figures 5.19a and b. The strains decreased from their maximum value at the FZ towards both sides of the blank through the HAZ as seen in Figures 5.19c and d.

For 127 mm (zero minor strain) and 50.8 mm (negative minor strain) TWBs specimens, the fracture occurred also away from the softening zone and located in the BM parallel to the weld line (Figure 5.17g and i). The strain distribution measured at sections along and across weld line (Figure 5.20) showed that the major strain was localized in BM while the weld zones (FZ and HAZ) were not affected (see Figure 5.21a, and c for 127 mm TWB specimen). It was noted that the fracture location shifted toward the center of the dome as the width of the samples decreased from 127 mm to 50.8 mm and to 12.7 mm for both TWBs and parent materials (see Figure 5.17(g-l)). Thus, for 12.7 mm TWBs specimens, the major strain localized at the pole area (center of the dome) as shown in Figure 5.17k, i.e., both the weld line (FZ) and the area in the vicinity (HAZ) were subjected to higher strain. However, the area on both sides of weld line (i.e., HAZ) was weaker than FZ and fracture mostly occurred in HAZ as depicted from major strain distribution profile in Figure 5.21b, and d.

Based on these results of out-of-plane hemispherical punch test for same gauge DP780 TWBs, the constraint effect as mentioned earlier for in-plane uniaxial tension still applies for out-of-plane hemispherical punch stretching tests for all strain paths. Since there was no strain localization or fracture in the softening zone as it was surrounded by zones with higher strength, its plastic deformation was constrained.

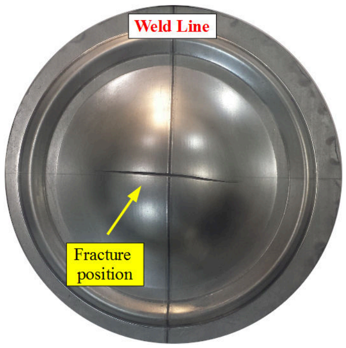

(a) 177.8 mm TWB (rubber).

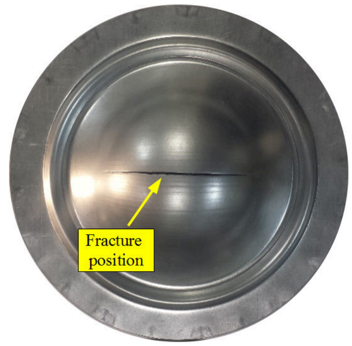

(b) 177.8 mm parent (rubber).

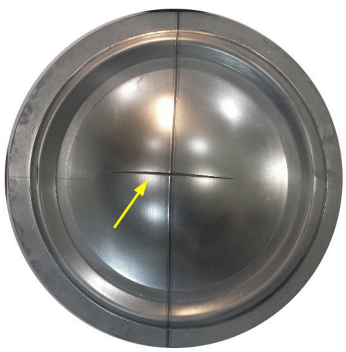

(c) 177.8 mm TWB (Teflon).

(d) 177.8 mm parent (Teflon).

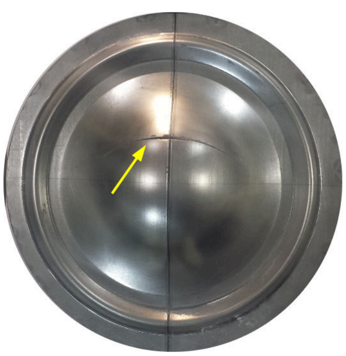

(e) 177.8 mm TWB (dry).

(f) 177.8 mm parent (dry).

(figure continued on next page)

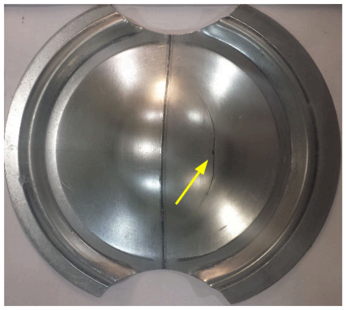

(g) 127 mm TWB.

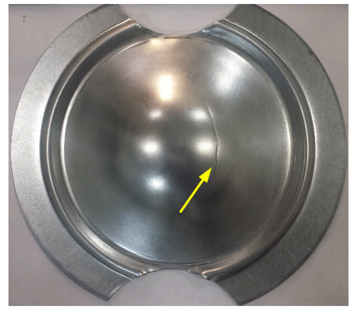

(h) 127 mm parent.

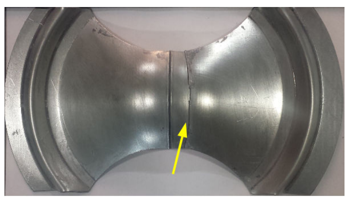

(i) 50.8 mm TWB.

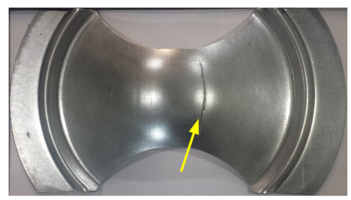

(j) 50.8 mm parent.

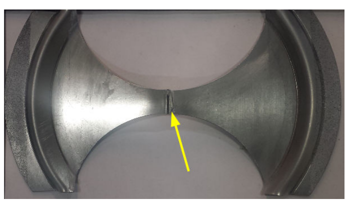

(k) 12.7 mm TWB.

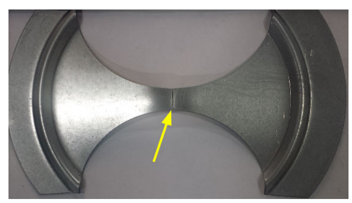

(l) 12.7 mm parent.

Figure 5.17. Comparison between fracture positions for DP780/DP780 1 mm/1 mm TWBs (left column), and DP780 1 mm parent sheets (right column) in different strain paths and lubricant conditions. (arrows indicate location of fracture).

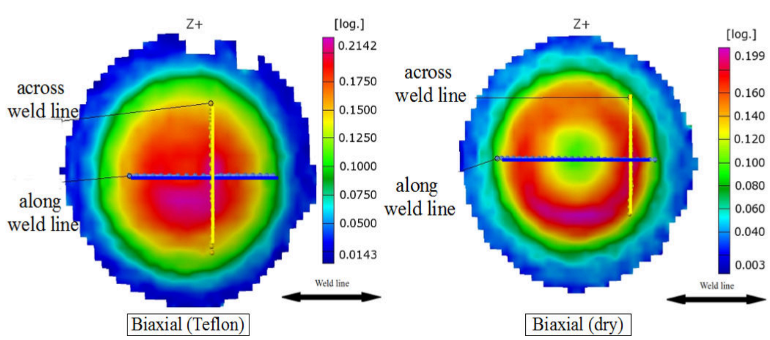

Figure 5.18. Sections lines for major strain distribution measurements for 177.8 mm biaxial (Teflon), and 177.8 mm biaxial (dry) TWBs specimens.

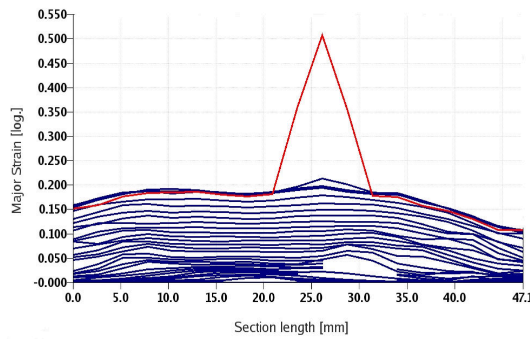

(a) Major strain distribution along weld line, biaxial (Teflon).

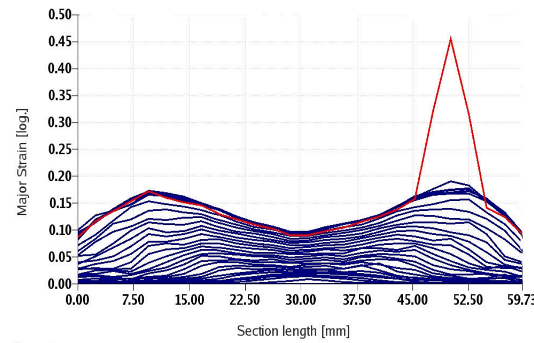

(b) Major strain distribution along weld line, biaxial (dry).

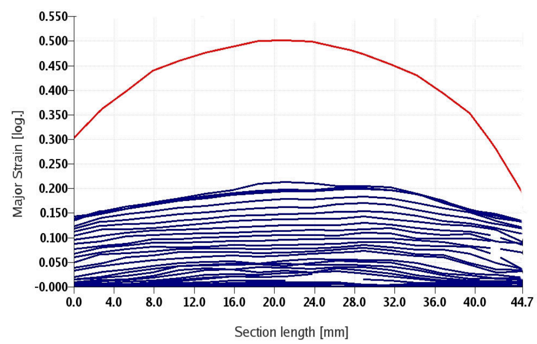

(c) Major strain distribution across weld line, biaxial (Teflon).

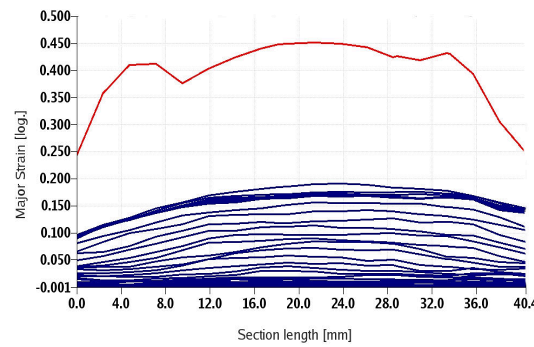

(d) Major strain distribution across weld line, biaxial (dry).

Figure 5.19. Major strain distributions up to fracture along and across weld line for DP780/DP780 1 mm/1 mm TWBs of 177.8 mm (full size) specimen with Teflon (left), and 177.8 mm (full size) specimen dry (right). (red curves indicate strain at fracture stage).

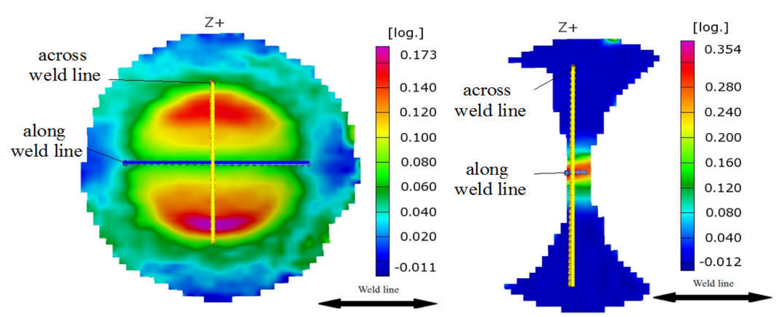

Figure 5.20. Section lines for major strain distribution measurements for 127 mm plane strain (left), and 12.7 mm uniaxial tension TWBs specimens (right).

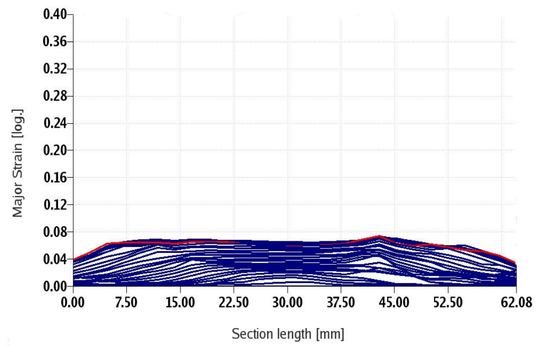

(a) Major strain distribution along weld line.

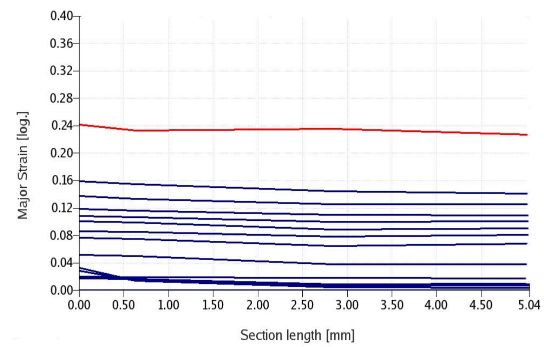

(b) Major strain distribution along weld line.

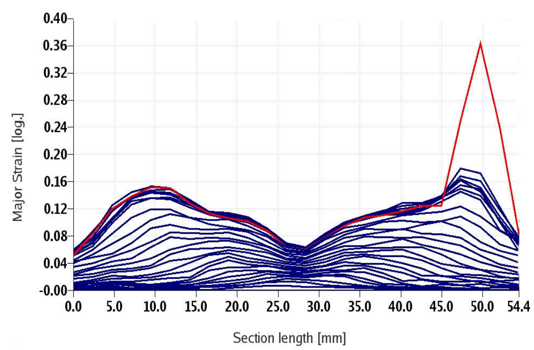

(c) Major strain distribution across weld line.

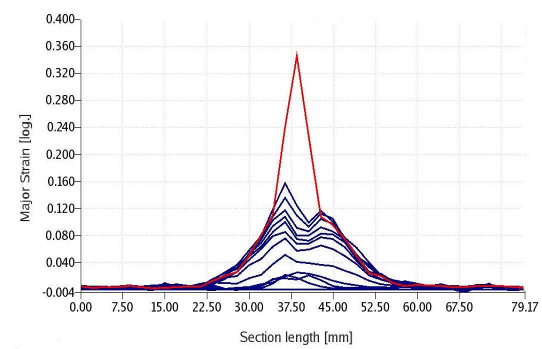

(d) Major strain distribution across weld line.

Figure 5.21. Major strain distributions up to fracture along and across weld line for DP780/DP780 1 mm/1 mm TWBs of 127 mm plane strain (left), and 12.7 mm uniaxial tension (right). (red curves indicate strain at fracture stage).

5.3.2 Effect on limiting dome height (LDH)

Measuring the hemispherical dome height just before fracture is the simplest method to check stretchability (or formability) of TWBs with respect to their parent materials. Figure 5.22 presents the punch load versus punch displacement traces for various DP780/DP780 1 mm/1 mm TWBs specimens. It was noted that the average LDH values were quite close for biaxial tension loading of 177.8 mm DP780 TWBs under different lubricant conditions (i.e., rubber, Teflon, and dry). This is not consistent with the general trends for most monolithic sheet materials where the LDH decreases with increasing friction (dry condition) as in case of DP780 parent materials (see Figure 5.23). This inconsistency in the LDH values may be due to occurrence of fracture in the welding area (FZ) at nearly similar punch load for all biaxial TWBs specimens with different lubricant condition (see Figure 5.24).

It has been proposed by many researchers that weld characteristics (e.g. strength, ductility, orientation and size) have a significant effect on the formability of the TWBs. However, if the weld (FZ) is sound, narrow and stronger than the BM (as in the case of fiber laser welding of steel sheets) and there is little distortion of BM (i.e., lower width of softening zone), it does not impact significantly the forming behavior of TWBs. LDH values were quite similar for both DP780 TWB and parent material in rubber and Teflon lubricant conditions with stretchability (i.e., ratio between LDH of TWB, and LDH of parent materials) higher than 98%. However, the LDH of TWB specimens in dry condition was higher than that of parent material with stretchability of about 114%. This may be due to similarity between biaxial TWB specimens of different lubricant conditions in terms of LDH and maximum breaking punch load values, which differ from the behavior of monolithic sheet materials as explained earlier. In other words, the stretchability of biaxial TWB specimen in dry condition was improved compared to the monolithic parent sheet. This is because of the softening zone was very small and surrounded by higher strength zones (constraint effect) and the strain was localized in higher strength area (FZ) (see earlier Figure 5.19). However, this is not the only reason to obtain higher LDH of TWBs specially those made from higher strength steels such as DP steel. The stretchability of the weld itself is an important factor. The stretchability of TWBs had been previously related to the hardness difference between the FZ and BM of the TWBs (Carlsson *et al.*, 2005). Although the hardness of the FZ of DP780

TWB is higher than the hardness of its BM, the hardness difference for AHSS is lower when compared with other steel TWBs. Therefore, stretchability of the weld can be improved and consequently LDH of the TWBs with decreasing the hardness difference between FZ and BM, especially when controlled and optimized laser welding parameters are used. In addition, the presence of the weld itself increases the resistance of the TWB specimen against contraction. This appeared in specimens where the weld was not stretched (i.e., transverse weld line with free edges) as in the case of 127 mm, 50.8 mm, and 12.7 mm TWBs specimens. The resistance against contraction along weld line (width direction) resisted the width deformation of TWB specimens compared to the parent material specimens, and consequently higher LDH at fracture for 127 mm, 50.8 mm, and 12.7 mm TWBs specimens was obtained with stretchability of about 120%, 127%, and 155% respectively.

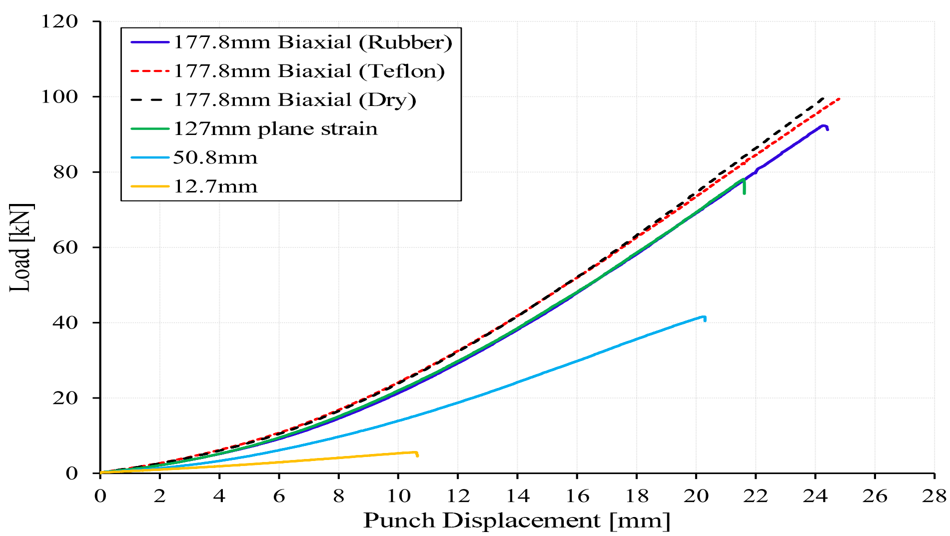

Figure 5.22. Punch load vs. punch displacement (LDH) for DP780/DP780 1 mm/1 mm TWBs specimens in different strain paths and lubricant conditions.

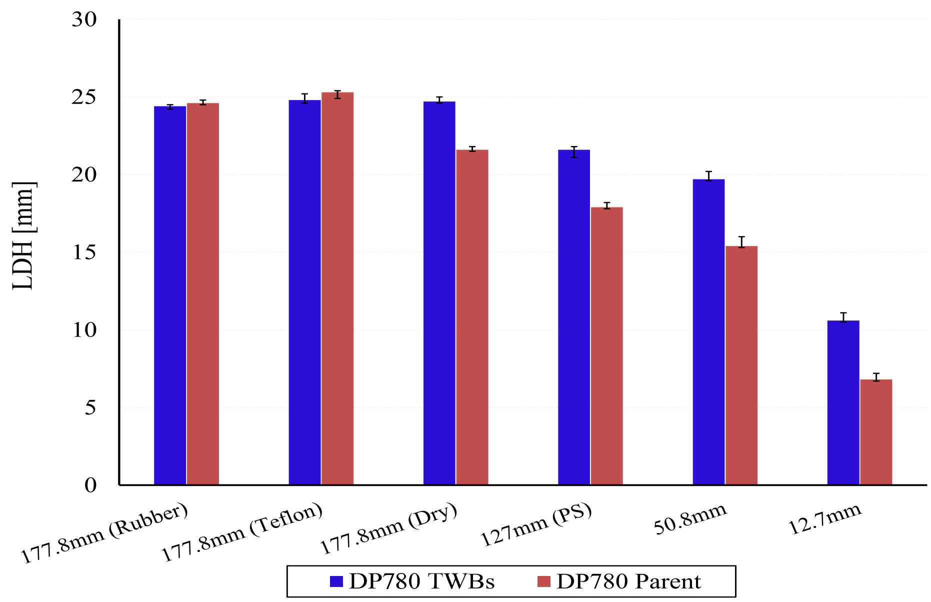

Figure 5.23. Comparison of average limiting dome height (punch displacement) for DP780/DP780 1 mm/1 mm TWBs, and DP780 1 mm parent material in different strain paths and lubricant conditions.

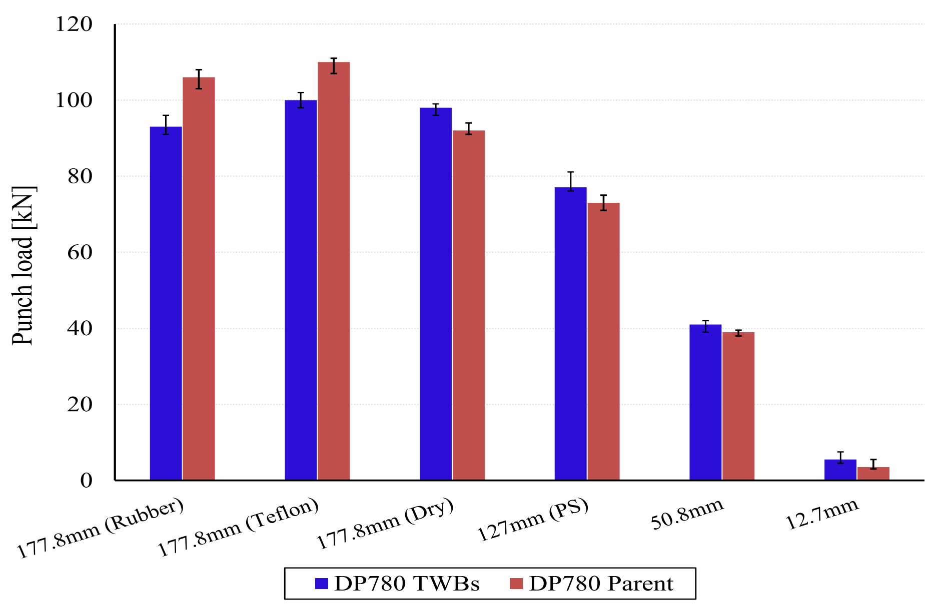

Figure 5.24. Comparison of average punch load at fracture for DP780/DP780 1 mm/1 mm TWBs, and DP780 1 mm parent material in different strain paths and lubricant conditions.

5.3.3 Effect of weld orientation on plane strain stretch forming

Figure 5.25 shows the failure location of the plane strain fractured samples with transverse and longitudinal weld lines respectively.

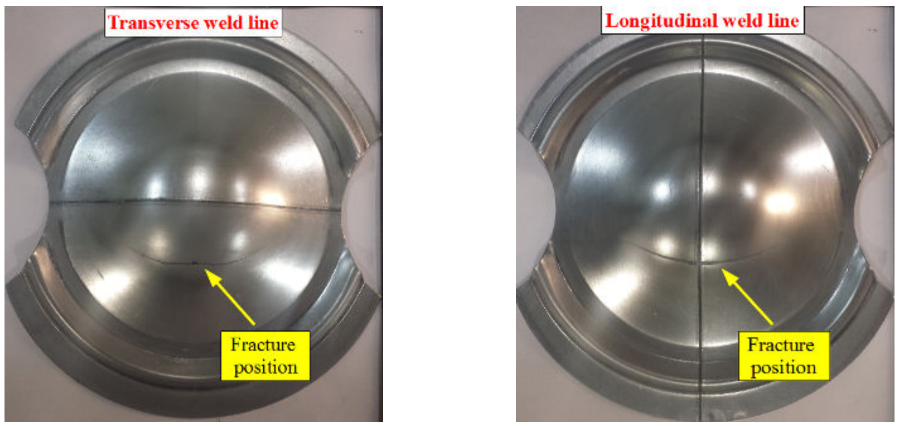

(a) Transverse weld line. (b) Longitudinal weld line.

Figure 5.25. Comparison between fracture positions for DP780/DP780 1 mm/1 mm TWBs with (a) transverse weld line, and (b) longitudinal weld line.

It can be seen that the fracture position was the same for both weld line orientations with respect to the loading direction. For the transverse weld line, the fracture occurred in the BM and parallel to the weld line. However, for the longitudinal weld line, the fracture initiated at the FZ and propagated perpendicular to the weld line toward the BM through the HAZ. Figure 5.26 illustrates the punch load versus punch displacement traces during the stretch forming tests for the 127 mm plane strain samples with both transverse and longitudinal weld line. One can observe that the two punch load versus punch displacement traces are nearly identical, i.e., there was no effect of weld line orientation on both limiting dome height (LDH) and the punch load (at fracture), although the weld lines in transverse and longitudinal orientations were subjected to different loads. For the transverse weld line, the loading direction was perpendicular to the weld line and to the softening zone while the weld line was free to move with punch movement due to the two free edges. The local orientation of the softening zone with respect to the loading direction is the most crucial factor which affects the deformation behavior of transverse weld TWBs. This effect was absent in the present case due to small width of softening zone and constraint effect. Therefore, the failure occurred in the unaffected BM as mentioned in Section 5.3.1. For the longitudinal weld line, the loading direction was along the weld line and in its vicinity, and the weld line was stretched with punch movement as it was constrained at the lock bead. The stretchability of the weld area played an important role in the deformation behavior of longitudinal weld TWBs. The stretchability of the weld increases as the amount of heat input decreases and consequently minimizing the hardness difference between the FZ and BM (see Section 5.3.2).

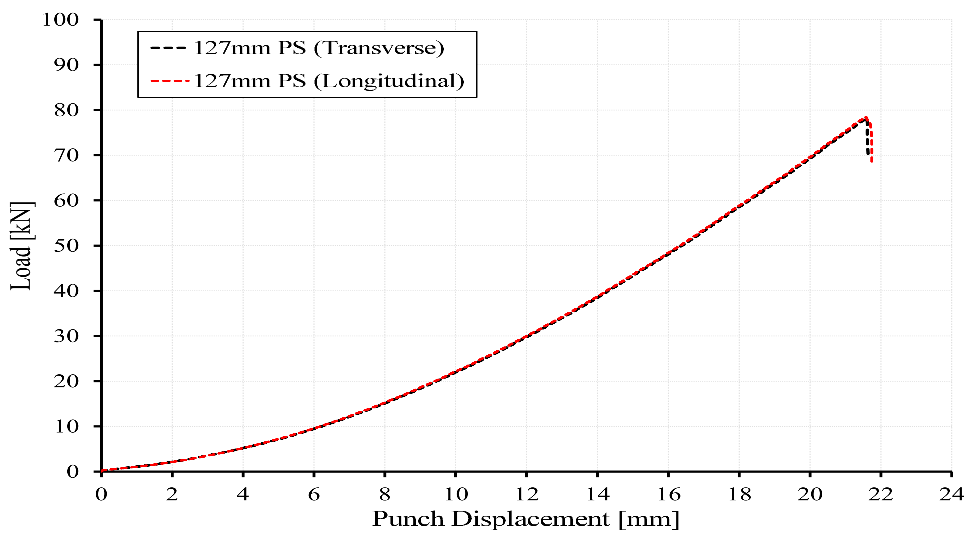

Figure 5.26. Comparison of punch load vs. punch displacement (limiting dome height) curves for DP780/DP780 1 mm/1 mm TWBs 127 mm plane strain specimens with transverse and longitudinal weld line orientations.

The effect of weld line orientation on the strain distribution is shown in Figure 5.27. The similarity between the strain maps of both transverse and longitudinal weld line orientations is noted even when the values of major and minor strains at the point of fracture for both orientations were nearly the same, i.e., a negligible effect of weld line orientation on limit strain. This may attributed to the narrow FZ, a higher cooling rate and a lower heat input for defocused fiber laser beam welding process. The process improved the deformation behavior of TWBs by decreasing the width of softening zone and improving the stretchability of the FZ.

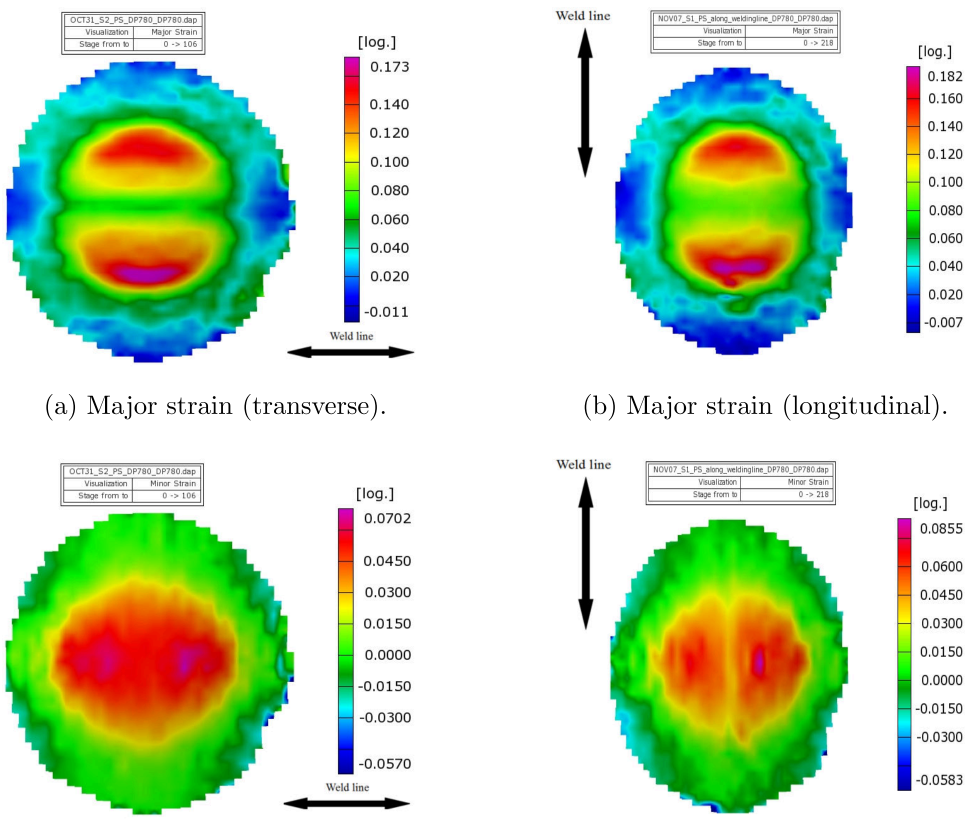

(a) Major strain (transverse).

(b) Major strain (longitudinal).

(c) Minor strain (transverse).

(d) Minor strain (longitudinal).

Figure 5.27. Major and minor strain maps distribution for DP780/DP780 1 mm/1 mm TWBs plane strain specimens with transverse weld line (left), and longitudinal weld line (right) at stages just before fracture as measured by Aramis on-line strain measurements.

5.3.4 Effect on forming limit diagram (FLD)

Figure 5.28 shows major and minor strain development traces (or strain paths) at the fracture points of DP780 1 mm parent material, and DP780/DP780 1 mm/1 mm TWBs. A significant reduction in maximum major strain values in all strain paths for DP780 TWBs compared to the DP780 parent material was observed. In addition, a reduction in maximum negative and positive minor strain values was observed for uniaxial tension and biaxial tension strain paths under rubber and Teflon lubricant conditions respectively.

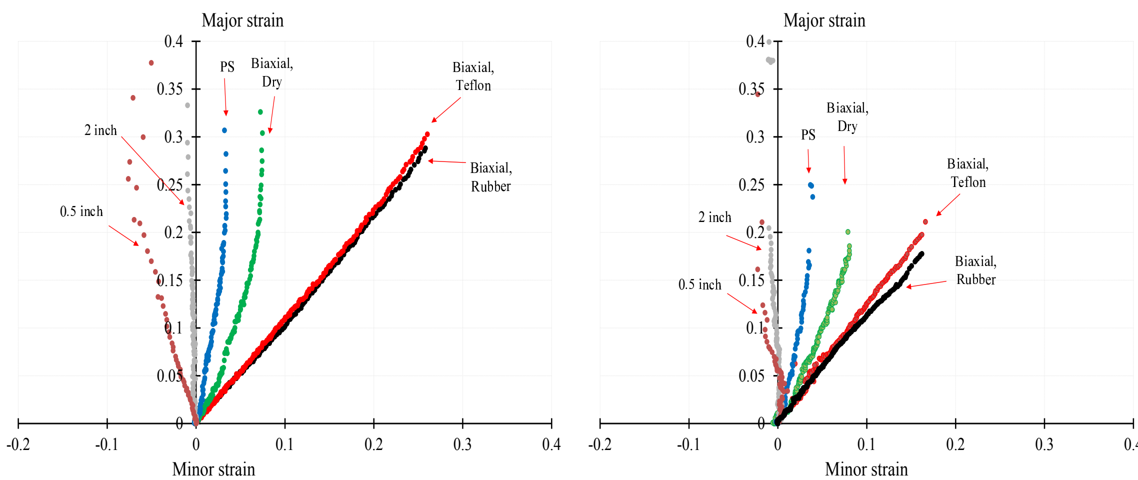

(a) DP780 1 mm parent material. (b) DP780/DP780 1 mm/1 mm TWB.

Figure 5.28. Major and minor strain development traces of the fracture points of (a) DP780 1 mm parent material, and (b) DP780/DP780 1 mm/1 mm TWBs in different strain paths as measured by Aramis on-line strain measurements.

Figure 5.29 demonstrates the FLD (or limit strain values) of DP780 TWBs and DP780 parents material. Despite the nearly matching values of total tensile elongation between DP780 TWBs and parent material, a significant drop in the FLD of the DP780 TWBs compared to that of the DP780 parent material was observed. It was reported that, if the weld is narrow, robust and stronger than the parent sheets (as in the case of fiber laser welded steel sheets), it does not impact significantly the forming behavior of the TWBs. The exception to this could be a situation where the weld is located in a critical region of TWB tested specimen where peak strains (major and minor strains) develop during forming (as in the case of full size biaxial strain paths where failure occurred in the FZ). In such cases, it may lead to a drop in the forming limit strain values since the weld tends to assist the development of the strain localization process. In addition, weld areas (FZ and HAZ) divide the material to two parts on both sides of weld line in the TWB specimen. Each side has a lower deformation compared to the parent material specimen where the whole material of the tested specimen is involved in the deformation. This results in lower major strain in TWB specimen. For plane strain and negative minor strain paths (strain paths of free edges weld line), the weld line is free to move and not stretched. It resists the contraction of the material in width direction (i.e., it resists the development of minor strain). In general, the presence of the weld in the TWBs increases their strength (yield and ultimate strength), than that of the base materials which in turn decreases the ductility and hence, reduction in the forming limit strains. Moreover, lower strain limits of the FLD (minimum major strain values for plane strain paths) were shifted to the right. It has been reported in the literature that strain paths during stretching over a punch become gradually nonlinear (or curved) toward plane strain, i.e., change of strain path occurs. This results in FLD shifting to the right (Graf and Hosford, 1993). In addition, the small prestraining that may occur to the specimens during clamping in lock-bead may also result in FLD shift (Hosford and Caddell, 2011).

The steps for determining the limit strain values using the time-dependent (t-d) method and the procedure for constructing the corresponding FLD, are presented in Appendix A.

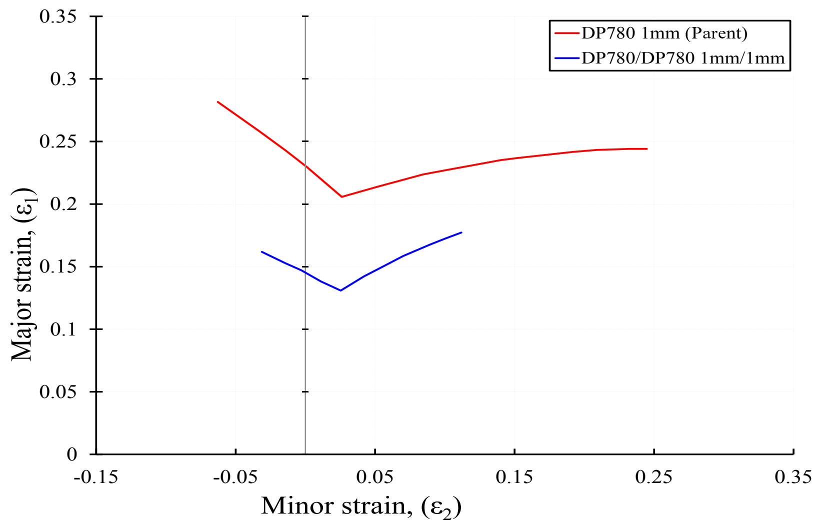

Figure 5.29. Forming limit diagram (FLD) for DP780 1 mm parent material, and DP780/DP780 1 mm/1 mm TWBs.

In summary, the effect of using defocused fiber laser beam welding on the formability and fracture of DP780/DP780 TWBs was compared to DP780 parent material. These were assessed in terms of fracture position, LDH, and FLD. The results showed that using defocused fiber laser beam is efficient in reducing the amount of heat input during welding process and consequently decreasing softening. No premature failure occurred in FZ or HAZ. The LDH values were quite similar for both TWB and parent material. However, a significant reduction in FLD was observed due to the presence of the weld itself. Therefore, methods to improve the ductility of the weld in the TWB should be explored in the future.

5.4 Deformation behavior of double-layer TWBs

5.4.1 IPPS double-layer TWBs

A newly developed formability test method (double-layer TWBs) was first assessed in in-plane plane strain (IPPS) tension mode. Figure 5.30 shows the load versus displacement traces of IPPS test specimens from DP780/DP780 1.5 mm/1 mm double-layer TWBs and HSLA/DP780 2.3 mm/1 mm double-layer TWBs with weld lines longitudinal and transverse to the loading axis.

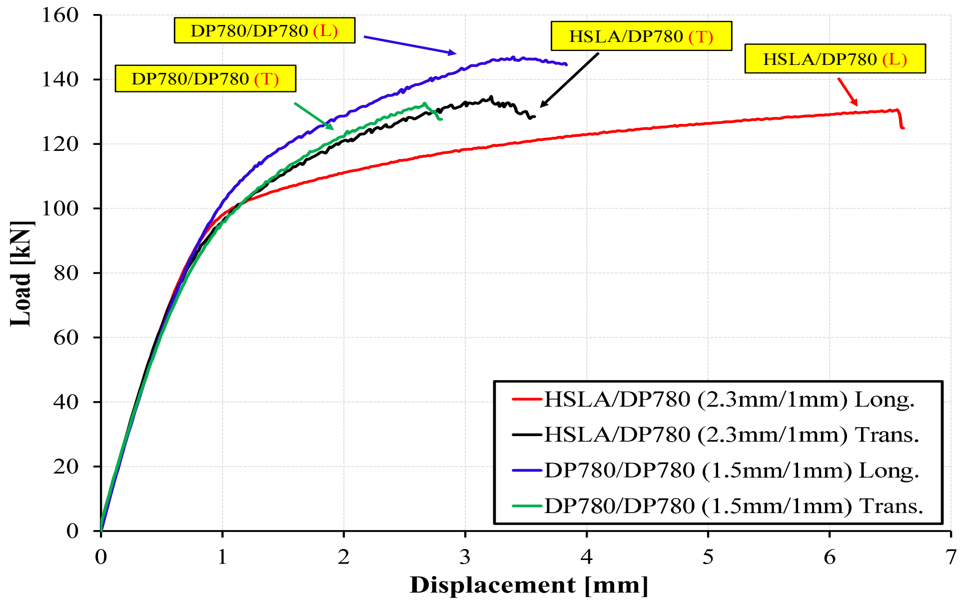

Figure 5.30. Comparison of load vs. displacement curves of IPPS tests of DP780/DP780 1.5 mm/1 mm and HSLA/DP780 2.3 mm/1 mm double-layer TWBs with longitudinal and transverse weld line orientations.

The results demonstrate that the total elongation of HSLA/DP780 double-layer TWBs with longitudinal weld line was higher than the elongation of the corresponding DP780/DP780 double-layer TWBs. The same behavior was observed for both configurations in case of transverse weld line orientation. A sketch representing the load transfer across these two weld configurations is shown in Figure 5.31. For the longitudinal weld line orientation, the weld area is exposed to the same load as the area in its vicinity (Figure 5.31a). Thus, the deformation mainly depends on the stretchability of the welding area (FZ) as well as the materials in its vicinity. Therefore, the larger elongation of HSLA/DP780 2.3 mm/1 mm double-layer TWBs compared to that of DP780/DP780 1.5 mm/1 mm double-layer TWBs may be attributed to the stretchability difference of the weld area of the two configurations. The stretchability of the FZ mostly related to the carbon contents and volume fraction of hard phases within the weld area. The higher carbon contents of the parent materials will likely lead to the lower stretchability of the FZ. For DP780/DP780 TWBs, both DP parent materials delivered higher carbon amount and martensite to the fusion zone during welding process than in case of HSLA/DP780 TWBs due to the more carbon contents and martensite phase from DP780 parent material compared to HSLA parent material. Hence, the weld area of DP780/DP780 TWBs became less stretchable than HSLA/DP780 TWBs. For the transverse weld line orientation, materials on both side of the weld area are exposed to the load and the weld line contributes less to load transfer (Figure 5.31b), i.e., for transverse weld line, the load transfer depends on the quality of weld area (no failure in the FZ), and not on the stretchability of weld area. Therefore, the total elongation of the TWBs with transverse weld line depends on the deformation of materials on both sides of weld line. For single-layer TWBs of thickness and/or strength difference, the deformation is confined to the thinner or weaker material during the uniaxial tensile test (see earlier section 5.2.1). However, in IPPS double-layer TWBs, there is force balance on both sides of the weld due to similar cross-section area and similar material combinations. Therefore, both thicker/stronger and thinner/weaker parent materials contribute to the total elongation. In other words, the deformation of thicker/stronger parent material is not negligible. This can be observed from the major strain distribution for both DP780/DP780 1.5 mm/1 mm and HSLA/DP780 2.3 mm/1 mm double-layer TWBs with transverse weld line (see Figure 5.32). However, more deformation occurred in HSLA 2.3 mm compared to the stronger DP780 1.5 mm as shear bands were observed in HSLA 2.3 mm, whereas, no shear bands in DP780 1.5 mm as depicted in the major strain distribution maps in Figure 5.32. Therefore, for transverse weld orientation, elongation of HSLA/DP780 2.3 mm/1 mm double-layer TWBs was larger compared to that of DP780/DP780 1.5 mm/1 mm double-layer TWBs.

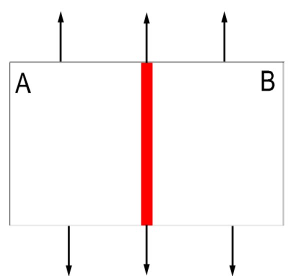

(a) Longitudinal.

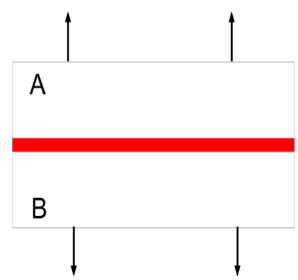

(b) Transverse.

Figure 5.31. Schematic drawing of load transfer along TWBs during IPPS tensile for (a) longitudinal weld line configuration, and (b) transverse weld line configuration.

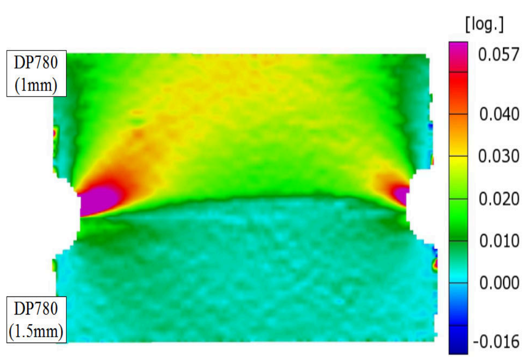

(a) DP780/DP780 1.5 mm/1 mm.

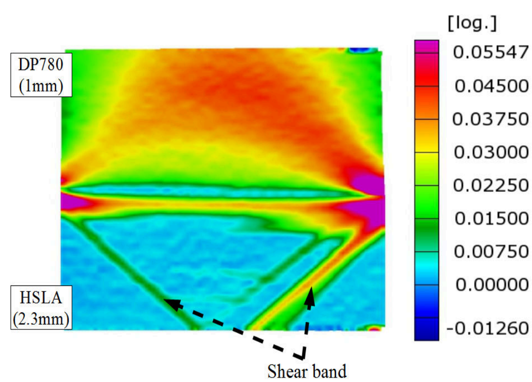

(b) HSLA/DP780 2.3 mm/1 mm.

Figure 5.32. Major strain mapping distributions just before fracture stage in the front TWB of IPPS double-layer TWBs with transverse weld line orientation for (a) DP780/DP780 1.5 mm/1 mm, and (b) HSLA/DP780 2.3 mm/1 mm.

With respect to the plane strain condition, Figure 5.33 demonstrates the average major and minor strain development in the front layer of IPPS test specimens for DP780/DP780 1.5 mm/1 mm double-layer TWBs and HSLA/DP780 2.3 mm/1 mm double-layer TWBs for longitudinal and transverse weld lines. Near plane strain condition (i.e., almost zero minor strain) can be observed.

Although the near plane strain condition was obtained, however, the fracture did not occur in the center of the tested specimens as the general trend of monolithic specimens. Figure 5.34 shows that the fracture occurred in the thinner sheet, DP780 1 mm, for both TWBs combinations and both weld line orientations. The crack initiated at the edge of the DP780 1 mm in front and back TWB layers for both TWBs combinations. Then, the crack propagated perpendicular to the weld line for TWB specimens with longitudinal weld line orientation, and, it propagated parallel to the weld line for TWB specimens with transverse weld line orientation. This was likely caused by the limited width of the available grips (4"). Wider grips have been suggested in the literature for obtaining in-plane plane strain condition and for fracture initiation in the middle of tested specimens. Also, for the longitudinal weld line orientation, the presence of the weld regions in the middle of the tested specimen made this area stronger but of poor ductility than the edge region (see Section 5.2.3). However, the crack initiated at the edge of thinner side, DP780 1 mm, instead of the weld region. This contradiction could not be explained on the basis of existing experimental data. Further experimental work or a FE analysis of the in-plane plane strain test would be needed.

It has to be noted that the weld line orientation with respect to the loading direction resulted in alteration of major strain development behavior. For the longitudinal weld line, a uniform increase of major strain behavior was observed for both TWBs configurations as shown in Figure 5.33b and c. This was due to the weld region as well as the thicker and thinner sheet in its vicinity continued carrying the load even after the fracture of thinner sheet occurred. In contrast, for transverse weld line for both TWBs configurations, uniform increase of major strain development occurred until crack started in thinner sheet. Then, a steep increase in major strain development behavior was observed (see Figure 5.33d and e). This was attributed to the fact that both thicker and thinner sheet contributed to carry the load until fracture initiated in the thinner sheet. Then, stress concentration occurred in the thinner sheet resulted in rapid increase in major strain development.

The results of IPPS test showed that the double-layer TWB test enabled testing of TBs incorporating sheets of different thickness and/or strength. The rapidity and reproducibility of double-layer test make it a quick test for checking the quality and the characteristics of the weld region as well as its applicability for wide range of TBs of any materials and thicknesses combinations. Moreover, in-plane forming tests show an advantage over out-of plane forming tests, in allowing strains to be measured on a flat surface with no effect of tooling geometry and friction condition. Out-of plane forming tests show greater deformation than those from in-plane forming tests, because the process of strain localization is much slower than that of in-plane stretching (Ghosh and Hecker, 1974).

The double-layer test method was used in in-plane test mode in one of the most critical strain path, plane strain. However, it was useful to check the applicability of the double-layer TWB method in out-of-plane test mode in different strain paths. The effect of this method on fracture position, fracture mode and limit strain was investigated and assessed.

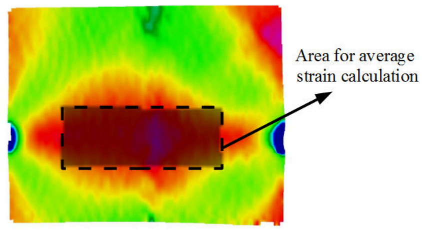

(a) Area for average strain calculations.

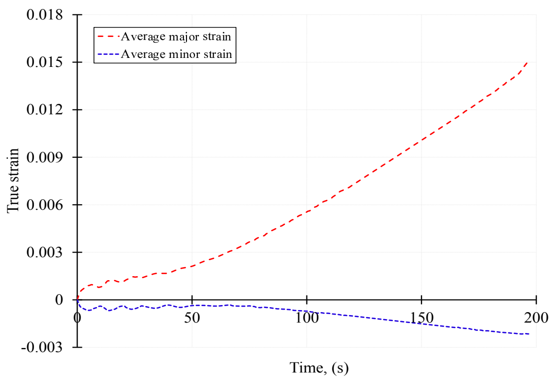

(b) DP780/DP780 1.5mm/1mm (Long.).

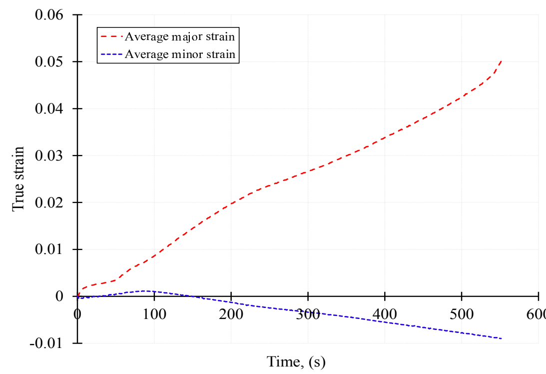

(c) HSLA/DP780 2.3mm/1mm (Long.).

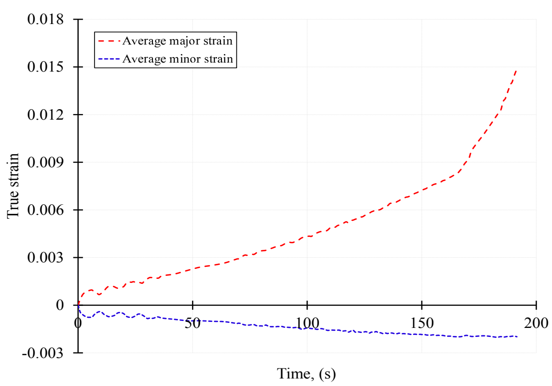

(d) DP780/DP780 1.5mm/1mm (Trans.).

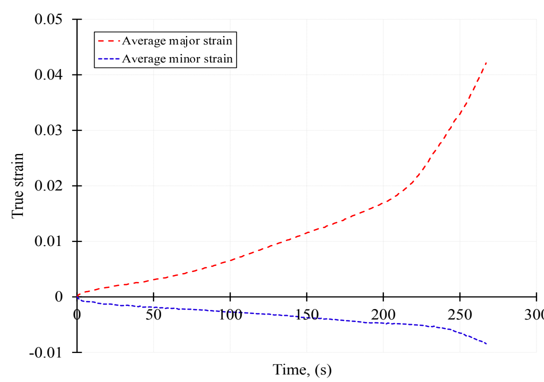

(e) HSLA/DP780 2.3mm/1mm (Trans.).

Figure 5.33. Average major and minor strain development measured in the selected area in (a) of IPPS test double-layer TWBs specimens with different weld line orientations; (b) longitudinal DP780/DP780 1.5 mm/1 mm, (c) longitudinal HSLA/DP780 2.3 mm/1 mm, (d) transverse DP780/DP780 1.5 mm/1 mm, and (e) transverse HSLA/DP780 2.3 mm/ 1mm.

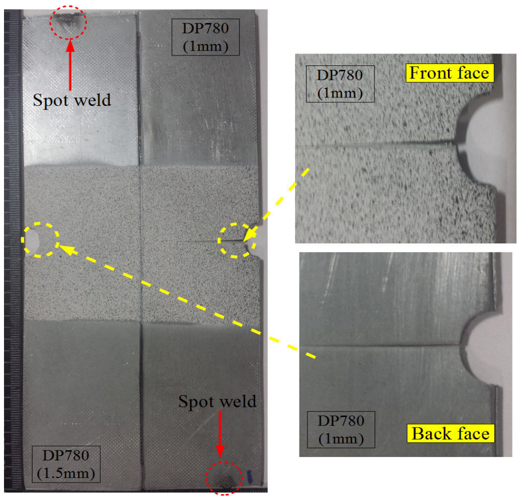

(a) DP780/DP780 1.5mm/1mm (Long.).

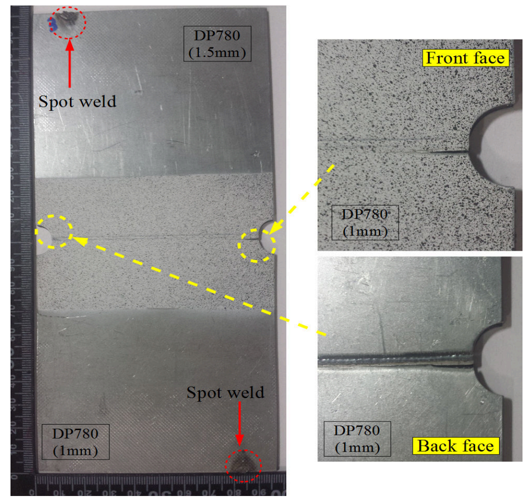

(b) DP780/DP780 1.5mm/1mm (Trans.).

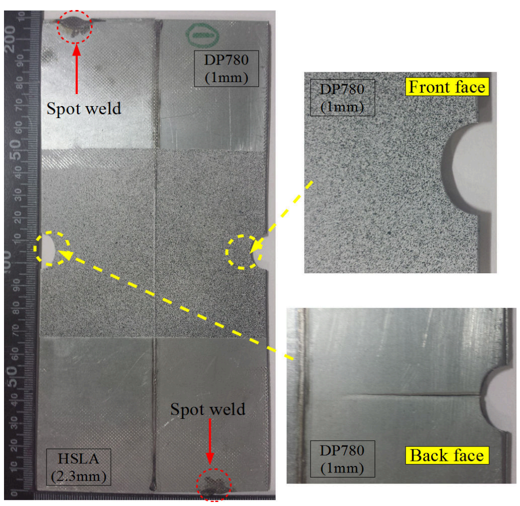

(c) HSLA/DP780 2.3mm/1mm (Long.).

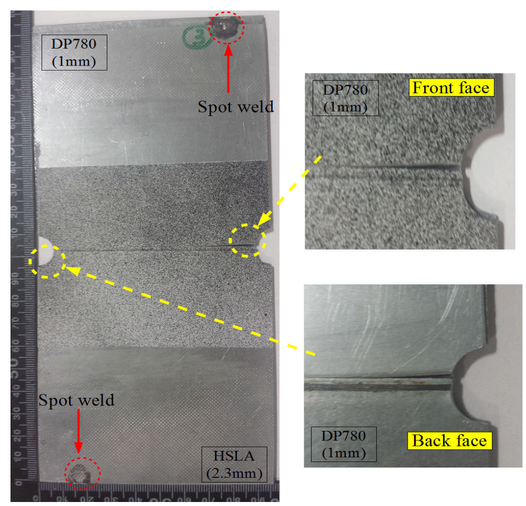

(d) HSLA/DP780 2.3mm/1mm (Trans.).

Figure 5.34. IPPS tests double-layer TWBs fractured specimens in different orientations of (a) longitudinal DP780/DP780 1.5mm/1mm, (b) transverse DP780/DP780 1.5 mm/1 mm, (c) longitudinal HSLA/DP780 2.3 mm/1 mm, and (d) transverse HSLA/DP780 2.3 mm/1 mm.

5.4.2 Out-of-plane double-layer TWBs

The TWBs combinations, DP780/DP780 1.5 mm/1 mm and HSLA/DP780 2.3 mm/1 mm double-layer and single-layer TWBs, were tested in out-of-plane test mode and for different strain paths by altering the specimen geometry and punch/sheet lubricant conditions, as earlier for single layer dome tests.

For the fracture position, the DP780/DP780 1.5 mm/1 mm single-layer TWB specimens fractured in the HAZ of DP780 1 mm side in all strain paths (Figure 5.35a). However, DP780/DP780 1.5 mm/1 mm double-layer TWB specimens fractured in the BM of DP780 1 mm side in all strain paths (Figure 5.35b), except for uniaxial strain path (12.7 mm width TWB with transverse weld line), where fracture occurred in the HAZ. In contrast, both HSLA/DP780 2.3 mm/1 mm single-layer and double-layer TWBs specimens fractured in the BM of DP780 1 mm side (see Figure 5.36a and b). The fracture position in single-layer specimens shifted somewhat away in BM from that of double-layer specimens due to weld line movement towards thicker HSLA 2.3 mm side as discussed later in this section. In addition, fracture in the BM of DP780 1 mm side occurred in all strain paths for double-layer specimens, as well as for bi-axial strain paths (right side of FLD) for single-layer specimens. For the plane strain and left side of FLD single-layer TWBs specimens with transverse weld line, all specimens failed in the welding area (FZ) once the clamping of tested specimen started in the lock-bead of upper and lower dies.

With respect to the fracture mode, no significant necking occurred in DP780 1 mm before fracture for all single-layer TWBs specimens from both TWBs combinations (see Figures 5.35a and 5.36a). The maximum thickness reduction at the fracture position was about 21% of the initial thickness of thinner sheet (DP780 1 mm) for DP780/DP780 1.5 mm/1 mm single-layer TWB specimens, whereas it was about 16% for HSLA/DP780 2.3

mm/1 mm single-layer TWB specimens. In other words, a rapid fracture occurred with no visible necking during limiting dome height tests of single-layer TWBs specimens. In contrast, visible necking was observed in the thinner sheet before fracture for all double-layer TWBs specimens from both TWBs combinations (see Figures 5.35b and 5.36b). The maximum thickness reduction at the fracture position was about 62% of the initial thickness of thinner sheet (DP780 1 mm) for DP780/DP780 1.5 mm/1 mm double-layer TWB specimens, whereas it was about 47% for HSLA/DP780 2.3 mm/1 mm double-layer TWB specimens. In other words, more necking occurred before fracture during limiting dome height tests of double-layer TWBs specimens.

(a) Single-layer TWB.

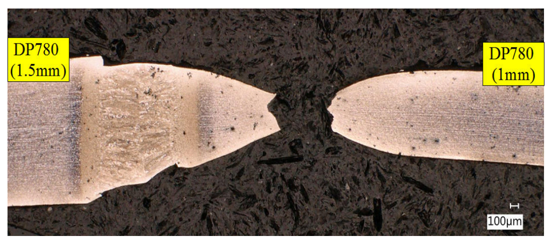

(b) Double-layer TWB.

Figure 5.35. OM image of fractured joint cross-section of 177.8 mm full size (Teflon) DP780/DP780 1.5 mm/1 mm TWBs for (a) single-layer TWB, and (b) double-layer TWB configuration.

(a) Single-layer TWB.

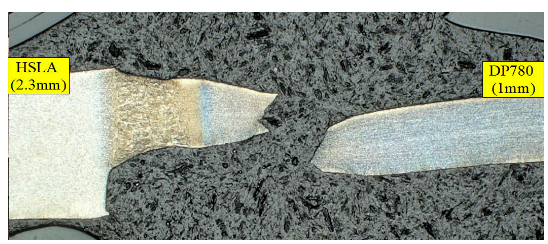

(b) Double-layer TWB.

Figure 5.36. OM image of fractured joint cross-section of 177.8 mm full size (Teflon) HSLA/DP780 2.3 mm/1 mm TWBs for (a) single-layer TWB, and (b) double-layer TWB configuration.

The differences between failure locations and degree of necking for DP780/DP780 1.5 mm/1 mm and HSLA/DP780 2.3 mm/1 mm single-layer and double-layer TWBs specimens, may be analyzed in terms of uniformity of deformation. The double-layer TWBs specimens during LDH tests deformed more uniformity due to both thickness balance (thickness compensation), and force balance (uniform contact). Moreover, the higher friction between upper and lower layer in the double-layer specimen compared to that between single-layer TWB and punch surface, tended to resist the deformation in the upper layer farther from the punch surface. This resulted in retardation of the failure of the upper TWB layer and consequently more necking occurred in this layer. In contrast, nonuniform deformation of the single-layer TWB was developed during LDH tests due to thickness difference and consequently nonuniform load distribution within the tested specimens. Although there was no material draw-in from the lock bead area of thinner sheet due to large applied clamping load, more stress developed within the thinner sheet due to weld line movement leading to fast deterioration of its formability.

For the effect of using double-layer TWBs on the limit strain of tested specimens, Figure 5.37 shows the FLD of both single-layer and double-layer TWBs specimens from DP780/DP780 1.5 mm/1 mm. It can be observed that the FLC of the double-layer TWB was higher than that of single-layer. However, positive and negative minor strain achieved for the double-layer case were lower than that of the single-layer.

The higher FLD (or higher major strain) may be attributed to the occurrence of more necking before fracture for the double-layer TWBs specimens which means that there was more deformation of the upper TWB specimens before fracture. i.e., more strain development within the specimens before failure. In contrast, lower necking (less strain development) occurred within the single-layer TWBs specimens before failure. In addition, the increased total thickness of the double-layer test specimens compared to that of the single-layer test specimens resulted in more stretching of the upper layer and consequently more strain due to a bending effect (increased radius of curvature). With respect to minor strain, the friction between the upper and lower TWBs in double-layer specimens which resisted the deformation of the upper TWBs in stretching strain paths (positive minor strain) and contraction strain paths (negative minor strain). This friction increased with increasing the size of the specimen, i.e., increasing contact area between the upper and lower TWBs. Also, the positive minor strain values were close together for all double-layer full size TWB specimens due to a similar friction coefficient between the upper and lower TWB layers even with changing lubricant condition between the lower TWB and the punch. The friction in the double-layer TWB specimens was higher than the friction between TWB and the punch in case of single-layer specimens which changed with specimen width as well as lubricant conditions. So, different values of minor strains were observed from single-layer TWB specimens.

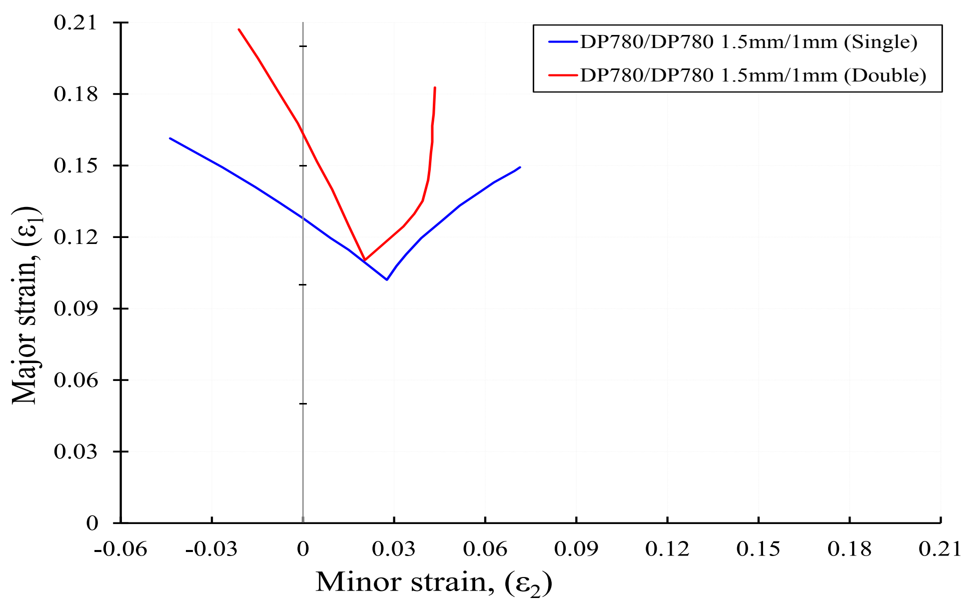

Figure 5.37. Forming limit diagram (FLD) for both DP780/DP780 1.5 mm/1 mm single-layer and double-layer TWBs.

One of the objectives of using double-layer TWBs was to decrease the weld line movement of TWBs of thickness and/or strength differences during limiting dome height tests by compensating for thickness differences and introducing uniform clamping force at the circumference of the tested specimens. Figures 5.38 and 5.39 show the results of hemispherical dome height tests of 177.8 mm full size single-layer and double-layer TWBs specimens from DP780/DP780 1.5 mm/1 mm and HSLA/DP780 2.3 mm/1 mm with two different lubricant conditions, Teflon and dry. For DP780/DP780 1.5mm/1mm TWBs (thickness ration=1.5), a slight decrease of the weld line movements were observed. The average reduction was about 8% and 20% for teflon and dry lubricant condition respectively. With increasing thickness ratio by 2.3 in the case of HSLA/DP780 2.3 mm/1 mm TWBs, a large reduction of the weld line movement was observed. The average reduction was about 67% and 86% for Teflon and dry lubricant condition respectively. Figure 5.40 shows the comparison between weld line movements for the two TWBs configuration with two different lubricant conditions. Therefore, the thickness balance and load balance introduced by the double-layer method as well as the friction between the upper and lower TWBs could reduce weld line movement and thereby, decrease the deterioration that may occur in the deformation behavior of the thinner sheet.

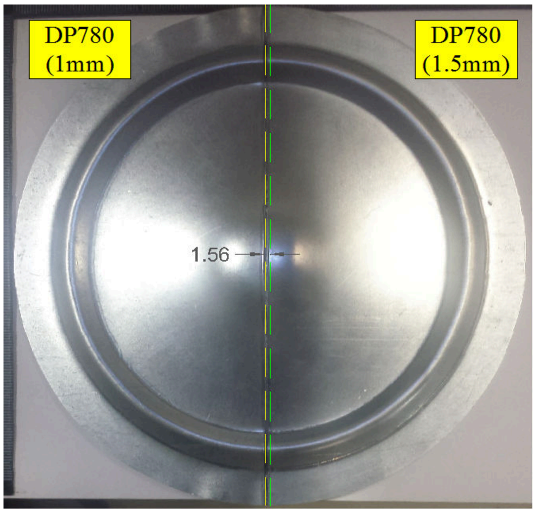

(a) Single-layer TWB (Teflon).

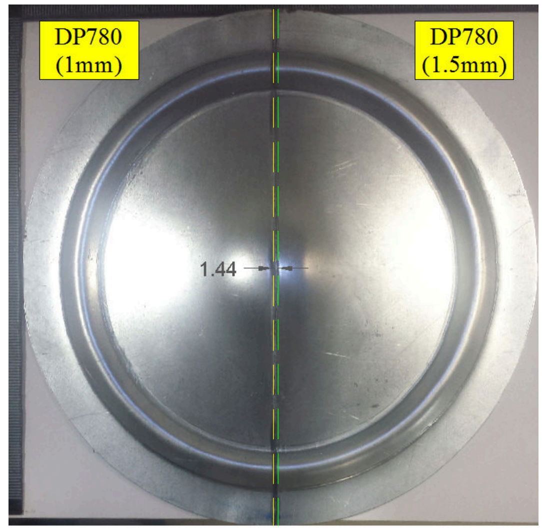

(b) Double-layer TWB (Teflon).

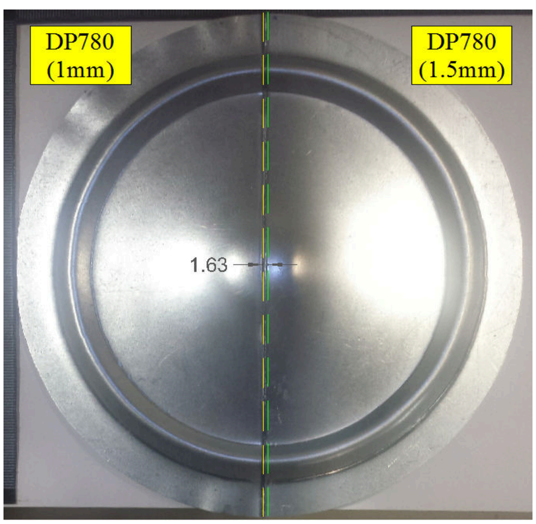

(c) Single-layer TWB (Dry).

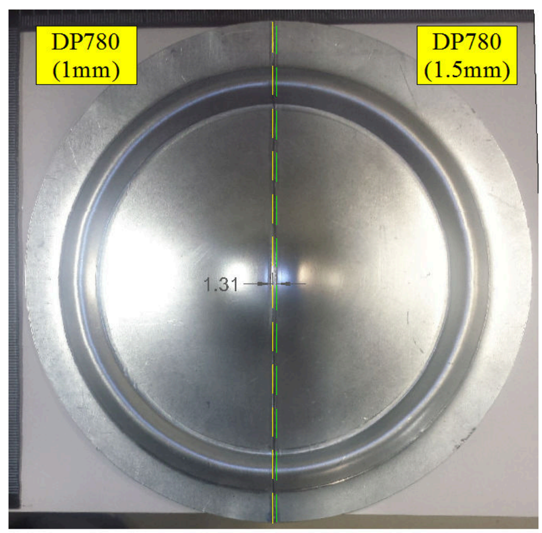

(d) Double-layer TWB (Dry).

Figure 5.38. Weld line shift of single-layer and double-layer in 177.8 mm full size DP780/DP780 1.5 mm/1 mm TWBs with two different lubricant conditions (a) single-layer TWB (Teflon), (b) double-layer TWB (Teflon), (c) single-layer TWB (dry), and (d) double-layer TWB (dry).

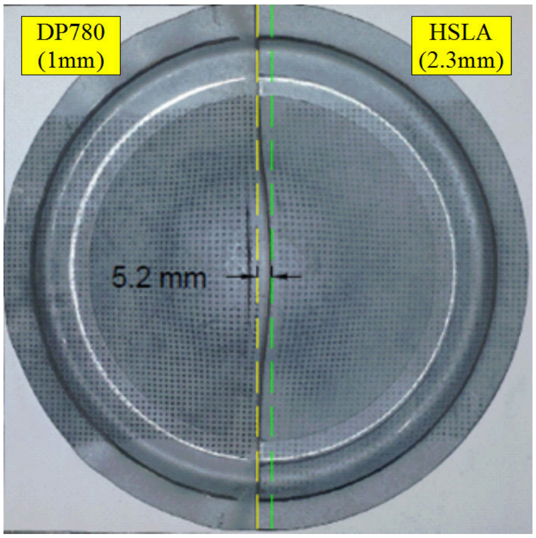

(a) Single-layer TWB (Teflon).

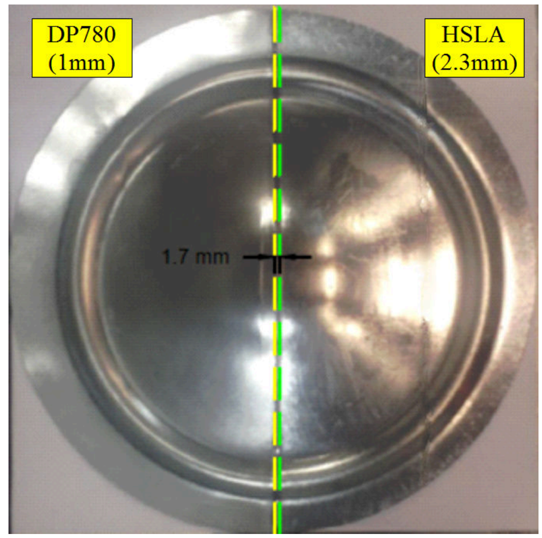

(b) Double-layer TWB (Teflon).

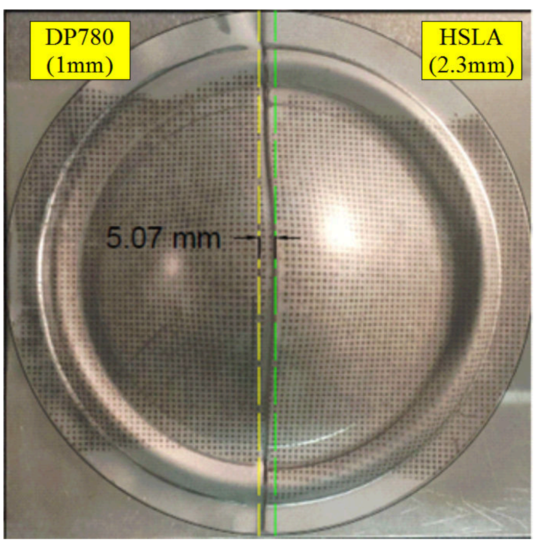

(c) Single-layer TWB (Dry).

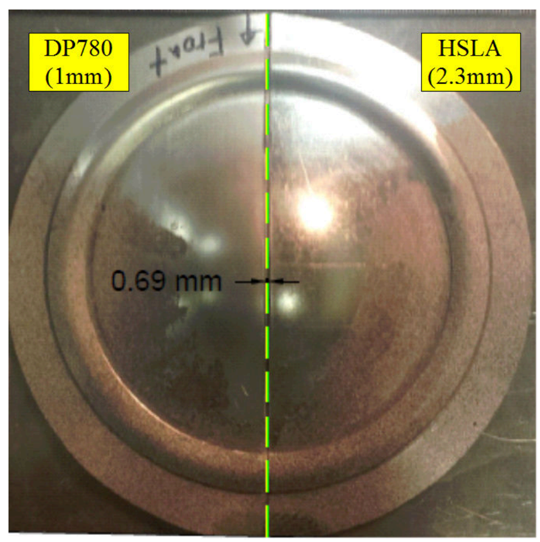

(d) Double-layer TWB (Dry).

Figure 5.39. Weld line shift of single-layer and double-layer in 177.8 mm full size HSLA/DP780 2.3mm/1mm TWBs with two different lubricant conditions (a) single-layer TWB (Teflon), (b) double-layer TWB (Teflon), (c) single-layer TWB (dry), and (d) double-layer TWB (dry).

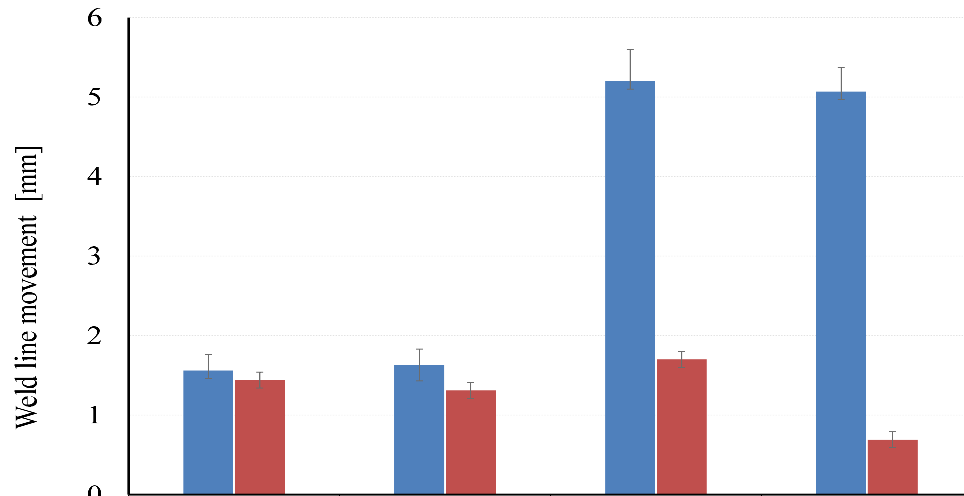

	DP780/DP780 (Teflon) 1.5mm\1mm	DP780\DP780 (Dry) 1.5mm\1mm	HSLA\DP780 (Teflon) 2.3mm\1mm	HSLA\DP780 (Dry) 2.3mm\1mm
Single-layer	1.56	1.63	5.2	5.07
Double-layer	1.44	1.31	1.7	0.69

Figure 5.40. Comparison between weld line shift of single-layer and double-layer of 177.8 mm full size DP780/DP780 1.5 mm/1 mm TWBs and HSLA/DP780 2.3 mm/1 mm TWBs with Teflon and dry lubricant conditions.

The following observations can be made from the results of out-of-plane double-layer TWBs specimens during hemispherical dome test.

- The tested specimens should be exactly centered with respect to the center of the punch. Any offset distance between the weld line and the center of the punch affects significantly the weld line movement.

- The upper and lower TWB layers should be perfectly stacked to each other. Any offset distance or overlap between the two weld lines results in stress concentration and premature failure.

- There is no constraint on the material or thickness combinations. It can be used with any TWB configuration.

- out-of-plane double-layer test can be applied for any strain paths, from biaxial stretch forming to uniaxial tension. However, the in-plane double-layer can not be applied for biaxial stretch forming.

- The friction coefficient between the upper and lower TWBs affects the strain measurements in the upper TWB.

- The double-layer test can be especially useful to assess poor weld due to lack of weld movement. It can assist with rapid weld quality assessment process.

In conclusion, the double-layer TWBs method was introduced as easy and reproducible method to test the formability of TWBs of thickness and/or strength difference. The results showed the applicability of this method in both in-plane and out-of-plane test mode. The failure location, failure mode and limit strain of double-layer TWBs were changed from that of single-layer TWBs. In addition, weld line movement was significantly reduced when using double-layer TWBs to compensate for a thickness difference.

5.5 Deformation behavior of steel-to-aluminum TBBs

Samples of AA2024/DP780 sheets in gauge combination 1.27 mm/1 mm from Laser/MIG and CMT brazing methods with sufficient wetting length for both upper and bottom faying surfaces were selected for the deformation behavior study. Three specimens from each brazing method were subjected to uniaxial tensile tests transverse to the braze line. The specimens were taken to fracture and assessed for fracture location, mechanical properties, and strain distribution in the vicinity of fracture.

Figure 5.41 shows the fracture locations for Laser/MIG and CMT brazing methods TBB specimens. Visible necking can be observed in area adjacent to the brazed area in aluminum BM for Laser/MIG brazing specimens. However, a catastrophic fracture occurred in the brazed area at aluminum/steel interface for CMT brazing specimens.

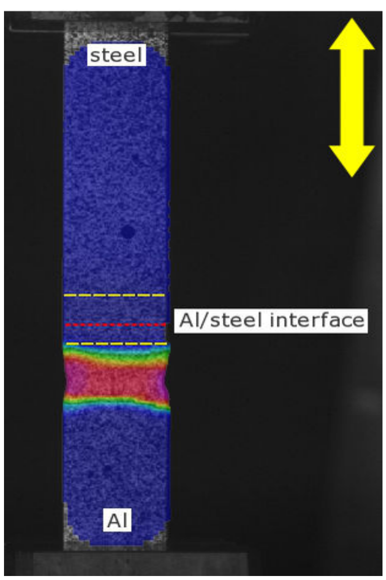

(a) Laser/MIG brazing.

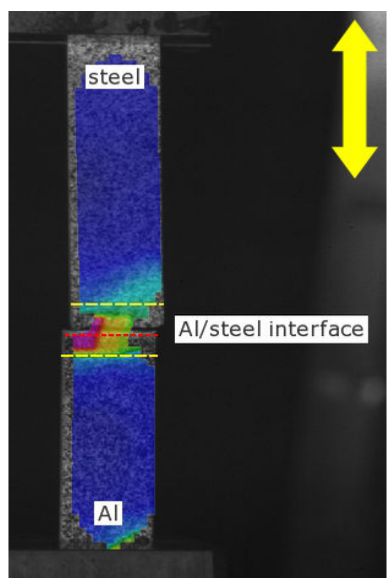

(b) CMT brazing.

Figure 5.41. Major strain mapping superimposed on the actual deformed specimen of AA2024/DP780 1.27 mm/1 mm TBBs made by (a) Laser/MIG hybrid brazing, and (b) CMT brazing methods. (vertical arrows indicate the direction of loading).

The major and minor strain maps and strain distribution profiles that were obtained along the tested samples for Laser/MIG and CMT brazing methods are shown in Figures 5.42 and 5.43 respectively. For Laser/MIG brazing, a much larger major strain of about 0.35 occurred on the aluminum side with visible necking. The steel side exhibited a rather small major strain of only 0.015 and the brazed area remained undeformed. In contrast, for TBB specimens produced by CMT brazing method, both aluminum and steel sides remained undeformed with only a small deformation of about 0.017 in the brazed region prior to its catastrophic fracture.

Due to such large difference in deformation and fracture behavior for the two methods of production of TBBs, further investigations were conducted with miniature tensile specimens using an in-situ uniaxial tensile test jig under a digital optical microscope. The results of these experiments are presented in the next section.

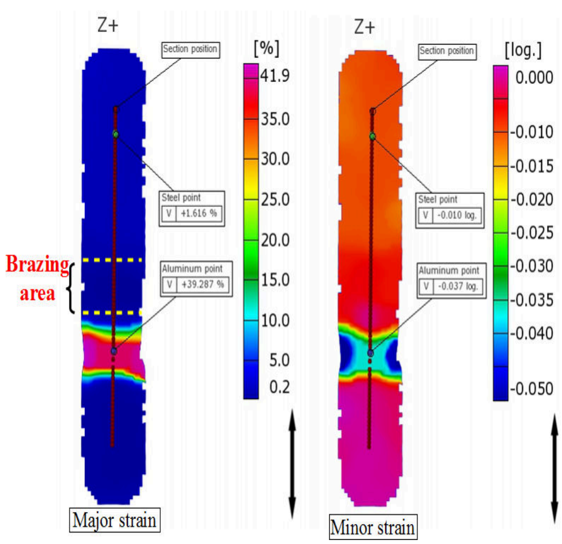

(a) Laser/MIG brazing.

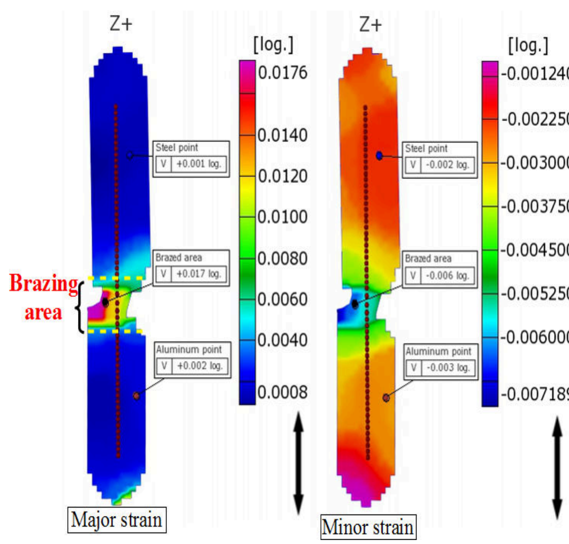

(b) CMT brazing.

Figure 5.42. Major and minor strain maps of AA2024/DP780 1.27 mm/1 mm TBBs for (a) laser/MIG hybrid brazing, and (b) CMT brazing.

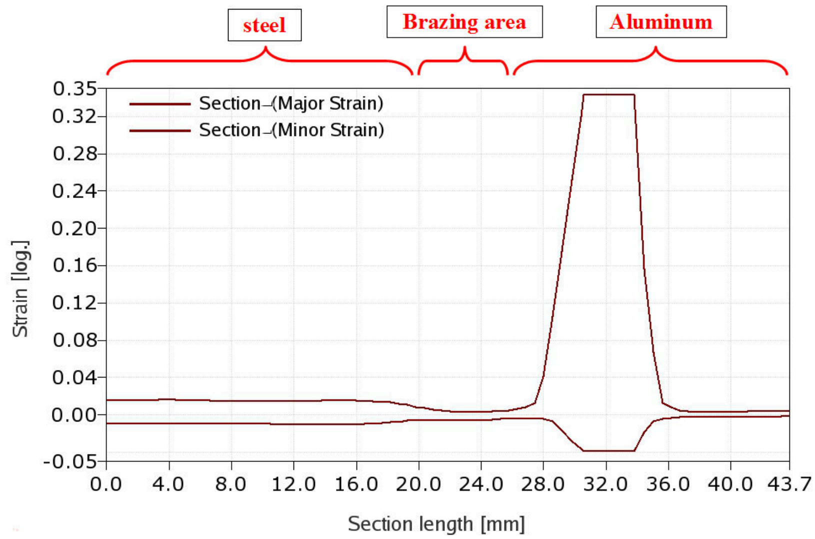

(a) Laser/MIG brazing.

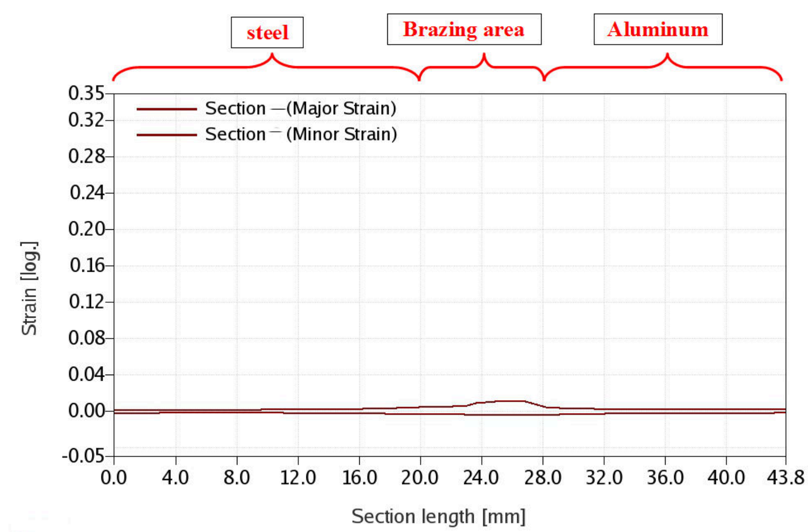

(b) CMT brazing.

Figure 5.43. Major and minor strain line properties as per Figure 5.42 just before fracture of TBB specimens of (a) Laser/MIG hybrid brazing, and (b) CMT brazing methods.

Figure 5.44 shows a comparison of the localized true stress-true strain curves to fracture of AA2024/DP780, 1.27 mm/1 mm, TBBs for both Laser/MIG and CMT brazing methods. It is clear that Laser/MIG brazed TBB specimens resulted in a much larger localized elongation of 28% and lower static tensile stress of 142 MPa. In contrast, the TBBs specimens of CMT brazing resulted in negligible localized elongation of 0.76% and a higher static tensile stress of 184 MPa. The procedures of construction of the localized true stress-true strain curves are presented in Appendix B.

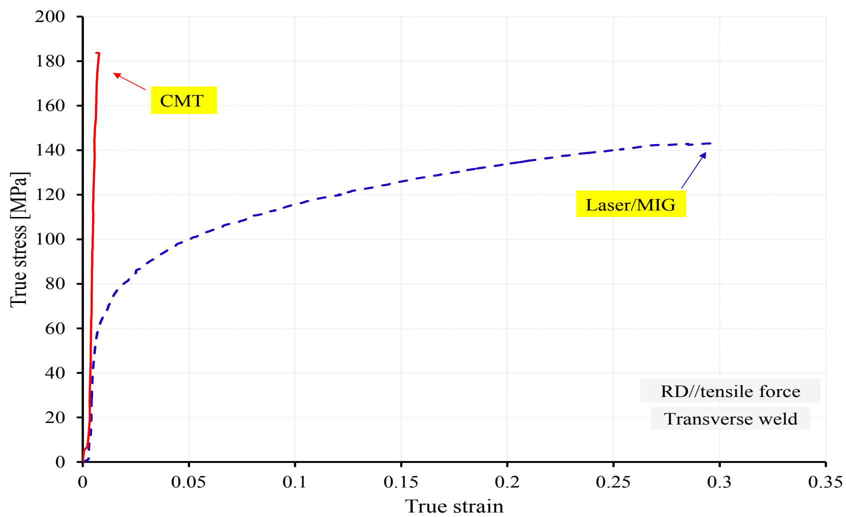

Figure 5.44. Comparison between localized true stress-true strain curves for AA2024/DP780 1.27 mm/1 mm TBBs specimens produced by Laser/MIG and CMT brazing methods.

The difference in the mechanical behavior of TBBs specimens from both brazing methods may be attributed to the difference in fracture location as well as the effect of the heat input during the respective brazing processes. For Laser/MIG TBBs specimens, visible necking occurred in aluminum BM adjacent to brazing area due to strength degradation after brazing process and the strain localized in this area (Figure 5.43a). The specimens became more ductile and more localized elongation was obtained. In contrast, CMT TBBs specimens failed in the thick brazing area which required more load to be fractured. In addition, much lower strain development was observed in the brazed area of CMT specimens compared to that occurred in aluminum BM of Laser/MIG specimens

(Figure 5.43b). It is to be noted that Laser/MIG hybrid brazing was used to decrease the amount of heat input by increasing the welding speed, and consequently lower the thickness of IMC layer at faying surfaces in the brazing area to get better mechanical performance. However, the area adjacent to the brazing area in the aluminum side was affected by this heat and became softer than the aluminum BM and the brazed area. In other words, loss of strength due to the partial annealing occurred adjacent to the braze during Laser/MIG hybrid brazing process. This phenomenon is well known in fusion welding and brazing processes of aluminum metal sheets (Schwartz, 2003; Kou, 2003). The loss of strength was also observed from the hardness values measured along the brazed specimens where a drop in hardness profile, compared to that of aluminum BM and brazing area, occurred in the area adjacent to the brazing area (see Figure 5.13). In contrast, CMT brazing TBBs did not show this behavior, i.e., no loss of strength occurred in the aluminum sheet. Thus, the strain concentrated in the thick brazing area which possessed lower hardness values and fractured at higher static tensile stress than that of Laser/MIG brazing TBBs which failed at the weaker area of aluminum BM (see Figure 5.14). The degree of annealing in aluminum BM sheet during Laser/MIG brazing process, and consequently the degradation of the strength, depends largely on the heat input and the exposure time.

5.5.1 Uniaxial tensile behavior of miniature TBBs

Magnified images (20x) of the brazed area and its vicinity were taken from through-thickness (LT) and width (NP) surfaces using miniature in-situ uniaxial tensile test jig in conjunction with the optical microscope (see earlier Section 4.4.2.1, Chapter 4). Figure 5.45 presents photograph of deformed test samples as well as major and minor strain maps from width region (NP plane) just before fracture for both Laser/MIG and CMT brazing TBBs.

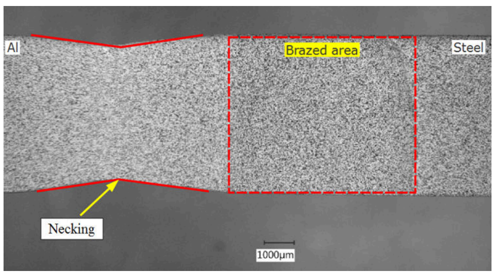

(a) Laser/MIG brazing, width region.

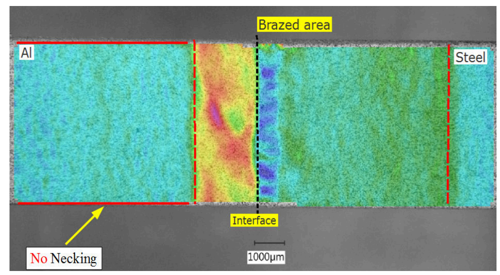

(b) CMT brazing, width region.

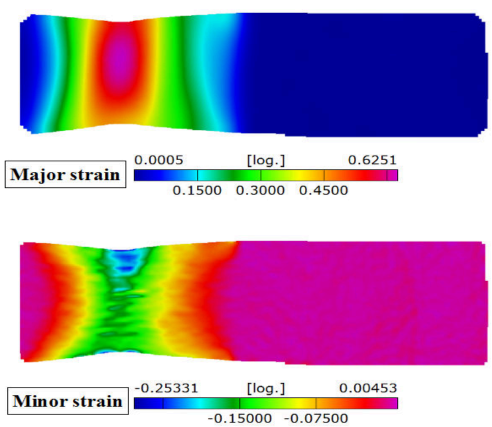

(c) Major and minor strain distribution.

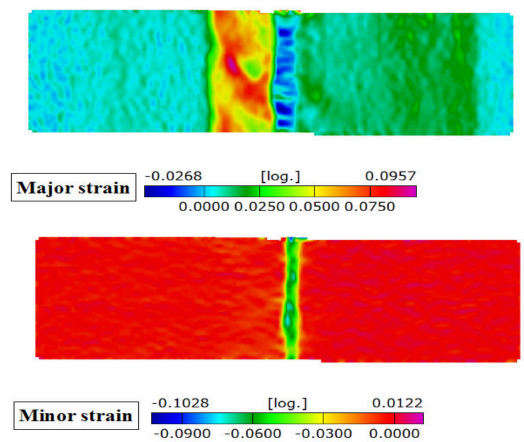

(d) Major and minor strain distribution.

Figure 5.45. Photograph of deformed samples and major and minor strain maps from width region of miniature test specimens of AA2024/DP780 1.27 mm/1 mm TBBs for Laser/MIG hybrid brazing (left), and CMT brazing (right).

For Laser/MIG TBB specimens, necking in the width region was clearly visible in aluminum BM adjacent to the brazed area without any deformation in the brazed area (Figure 5.45a and c). In contrast, results of CMT TBB specimens showed no necking or deformation in the the width region in the vicinity of the brazed area (see Figure 5.45b). However, the brazed area incorporated different deformation behavior according to the distribution of the major strain in this area as shown in Figure 5.45b and d. For example, weld seam, wetting area and the interface area show different colors in the major strain spectrum corresponding to large, moderate and low strains, respectively. The interface area of the CMT TBB specimens has the minimum value of major strain (see Figure 5.45d). Fracture occurred catastrophically in this area.

Figure 5.46 demonstrates the development of major and minor strain in the through-thickness region for both Laser/MIG and CMT brazing TBBs. For Laser/MIG specimens, the strain maps show that strain increased in the area adjacent to the brazed area where necking in the thickness direction was clearly visible in aluminum BM and a ductile fracture occurred in this area with no deformation in the brazed area (see Figure 5.46a, c and e). However, a negligible increase in strain for CMT brazing TBBs was observed (see Figure 5.46b, d and f). The strain concentrated in a region at the side faying surface, i.e., at the aluminum/steel interface, as seen in Figure 5.46f leading to a catastrophic brittle fracture. This may be attributed to lack of adhesion between aluminum and steel at side faying surface (steel/aluminum interface) due to the lack of a zinc coating layer at the steel edge. It was reported that the zinc coating layer on steel sheet surfaces is crucial in improving the wetting and adhesion between molten aluminum and steel substrate at the faying surfaces (see earlier Section 2.5.1, Chapter 2). However, the edge of steel sheets to be joined was cut and milled. So, the zinc coating layer at the side faying surface was removed and consequently affected the adhesion at aluminum/steel interface. The difference between the failure of TBBs for both Laser/MIG and CMT brazing can be clearly seen in the through-thickness optical images from polished sections as presented in Figure 5.47.

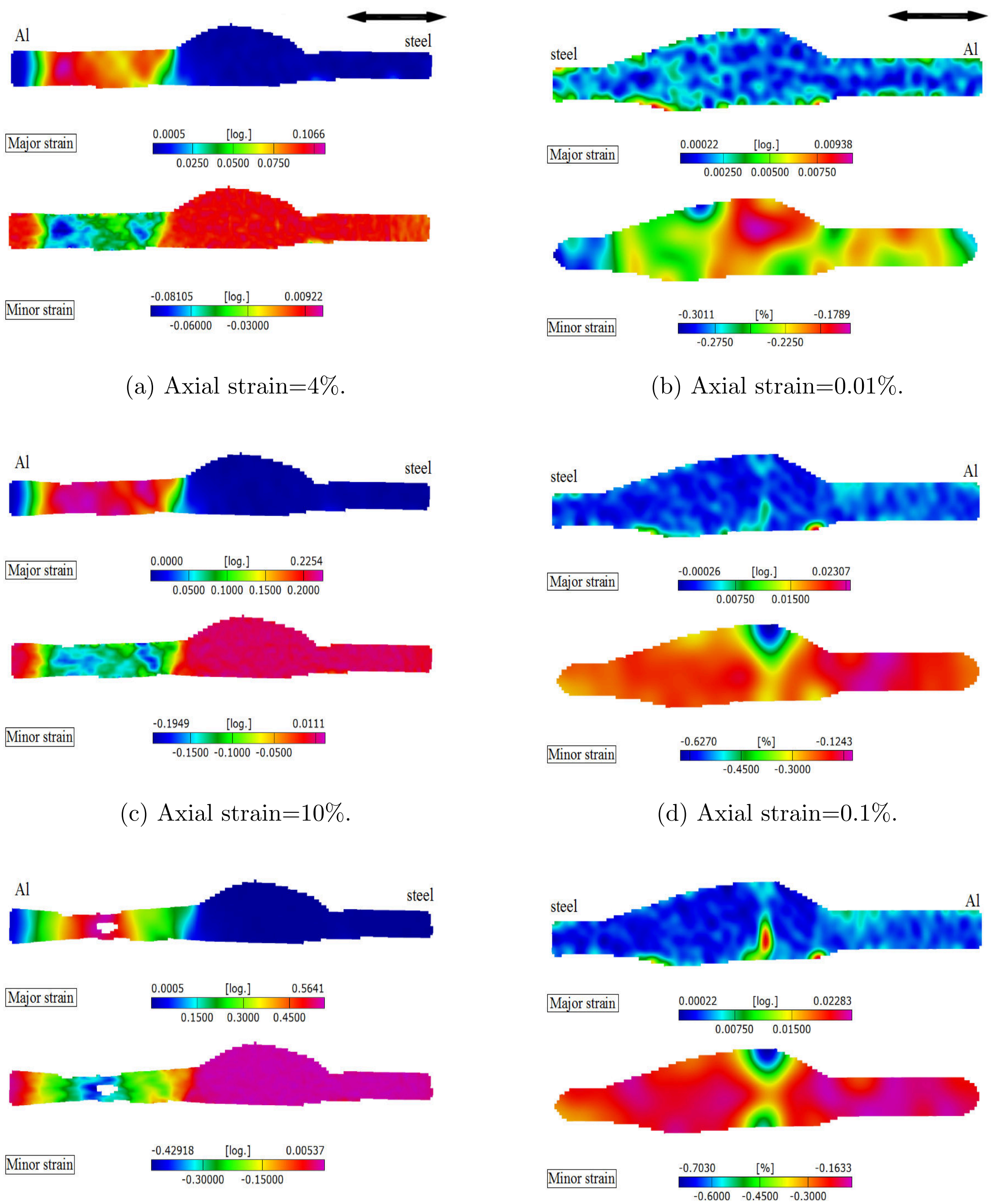

(a) Axial strain=4%.

(b) Axial strain=0.01%.

(c) Axial strain=10%.

(d) Axial strain=0.1%.

(e) Axial strain=17%.

(f) Axial strain=0.17%.

Figure 5.46. Sequence of major and minor strain development at different axial strains of miniature through-thickness surface of AA2024/DP780 1.27 mm/1 mm TBBs for Laser/MIG hybrid brazing (left), and CMT brazing (right).

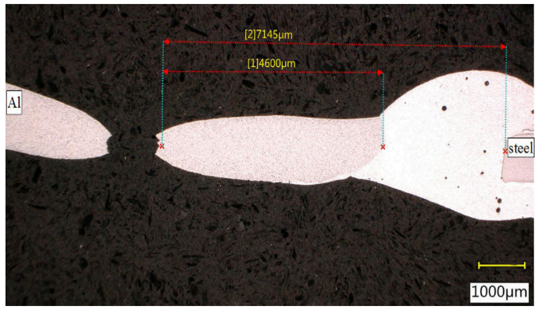

(a) Laser/MIG brazing.

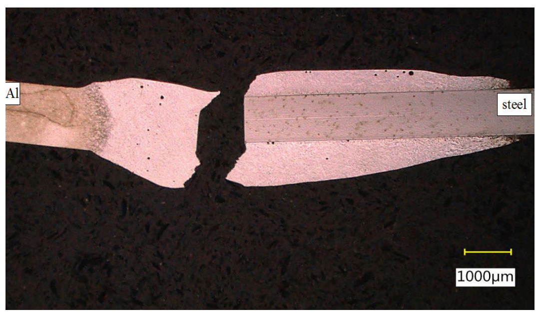

(b) CMT brazing.

Figure 5.47. OM images of through-thickness plane of fractured AA2024/DP780 1.27 mm/1 mm TBBs for (a) Laser/MIG hybrid brazing, and (b) CMT brazing.

Figure 5.48 shows plots of point strain histories of six, (1-6) and three (7-9), different positions in TBBs for Laser/MIG and CMT test specimens respectively. It is to be noted that the strain at fracture point 2 started to increase earlier than any other point in TBBs until fracture for Laser/MIG brazing TBB specimens. This means that strain localization set in early in aluminum BM in the area adjacent to the brazed area. In contrast, the strain in TBBs of CMT brazing was slightly higher in the area in the vicinity of the brazed area, point 8, in aluminum BM until close to fracture when a catastrophic increase in strain occurred at the fracture point 7. This means that the area in the vicinity of the brazed area was only slightly affected by the heat input during the CMT brazing process and the softening of this region was not dominant.

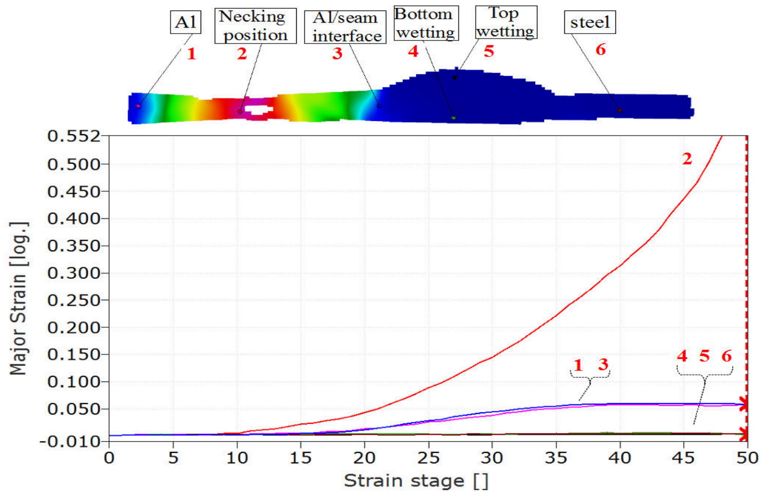

(a) Laser/MIG brazing TBBS specimens.

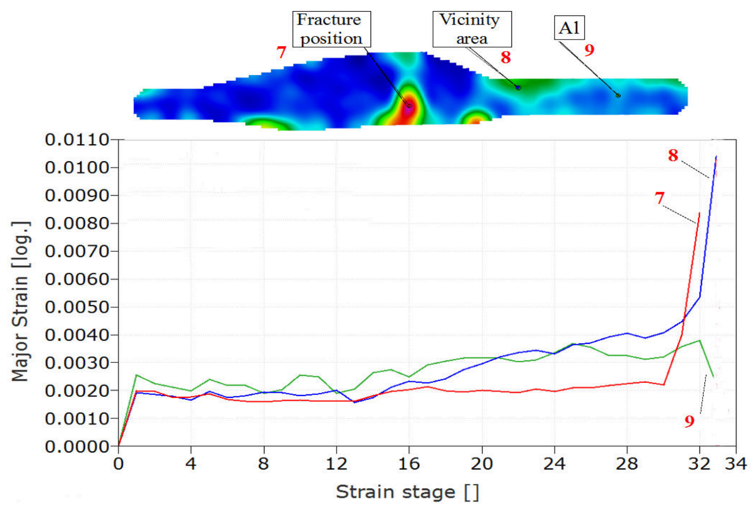

(b) CMT brazing TBBS specimens.

Figure 5.48. Point strain histories at different positions of AA2024/DP780 1.27 mm/1 mm TBBs specimens for (a) Laser/MIG hybrid brazing, and (b) CMT brazing.

Since failure of Laser/MIG brazing TBBs always occurred in the area adjacent to the brazed area, the brazed area (points 4 and 5 in Figure 5.48a) remained less strained. Therefore, to "enable" the failure in the brazed area, specimens of Laser/MIG brazing TBBs were notched in the width direction at the steel/aluminum interface with different width ratios. The presence of a notch was expected to cause failure of the brazed region rather than the weak adjacent area in aluminum BM. These results are presented next.

5.5.2 Deformation behavior of notched TBBs

TBBs specimens from Laser/MIG brazing with initial width of 10 mm and average wetting length of 4 mm were cut at steel/aluminum interface to reduced width of 6 mm, 4 mm and 2 mm, respectively as shown in Figure 5.49. Width ratio was defined as the ratio of reduced width over the full width of the specimen. Three samples per each width ratio were subjected to uniaxial tension along X-axis (i.e., perpendicular to the notch direction), while magnified images of deformed specimens were continuously recorded using optical microscope. A speckle-pattern was applied to the notch region and Aramis system was used for obtaining strain maps in the notched region.

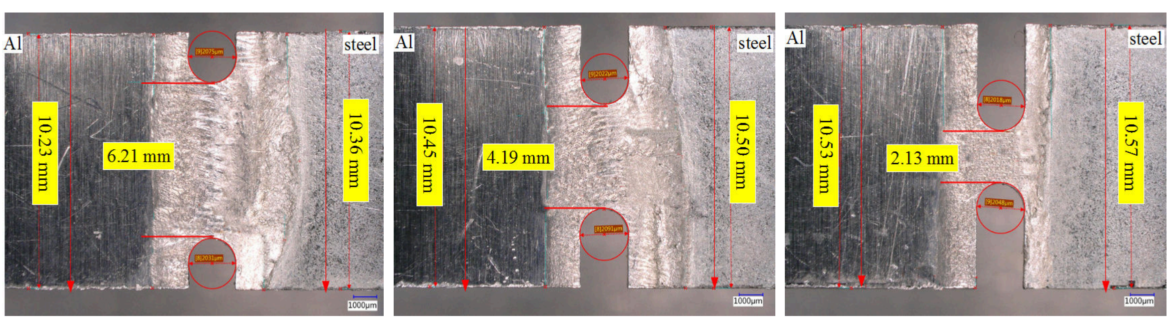

(a) 0.6 width ratio. (b) 0.4 width ratio. (c) 0.2 width ratio.

Figure 5.49. Geometries of notched specimens of AA2024/DP780 1.27 mm/1 mm TBBs with: (a) 0.6 width ratio, (b) 0.4 width ratio, and (c) 0.2 width ratio.

Figure 5.50 shows a plot of major and minor strain distributions along the length AB of the notched specimen for a width ratio of 0.6. The failure still occurred in the area adjacent to the brazing area in aluminum BM. As noted earlier, the degradation of the strength in this area was due to the partial annealing that occurred from the heat input during Laser/MIG brazing process. The strain tended to concentrate in this area rather than in the brazed area. No strain development occurred in the brazed or wetting length areas (see Figure 5.51). Similar results were obtained at the next lower width ratio of 0.4 as shown in Figure 5.52. The strain was still localized in the affected area adjacent to the brazing area and extended to the weld seam zone in the transition area between weld seam and aluminum BM. Moreover, the strain concentration occurred in the transition area between the brazed area and steel BM due to the increase in load transfer through the upper and lower wetting areas (shear area) with decreasing the cross-section at the brazed zone. The minor strain distribution in Figure 5.52, shows that necking occurred in width direction in the affected area adjacent to the brazed area as well as in the brazed area itself. However, it was closer in the brazed area and the fracture occurred catastrophically at steel/aluminum interface. This may be caused by a lack of adhesion between aluminum and steel at steel/aluminum interface (side faying surface) because of the absence of the zinc coating during edge preparation of steel sheets before joining process. In addition, the presence of different materials in this area consisting of steel, aluminum weld seam and IMC layer and their different physical and mechanical behavior could further localize the fracture process. When the strain concentrates in this area, the deformation starts first in the weaker or more ductile material (aluminum weld seam) within the brazed area. Due to the diversity of relative deformation between materials in this area, separation occurred in the weaker/stronger material interface and consequently crack and subsequent fracture took place and propagated from this point. The development of major and minor strain from the start of loading till the fracture at the steel/aluminum interface, for a width ratio of 0.4, is shown in Figure 5.53.

On further decreasing the width ratio to 0.2, the strain initiated in the area adjacent to the brazed area. However, it was higher and localized in the transition area between the brazed area and steel BM and consequently separation and fracture occurred in this area as shown in Figure 5.54. This also can be seen from the development of the major and minor strains presented in Figure 5.55. This may be attributed to the increase in the load transfer to the smaller wetting area (i.e., shear area) that could not bear this load. Excessive loading of this shear area could separate the upper and lower wetting lengths from the steel substrate (see Figure 5.55g and h).

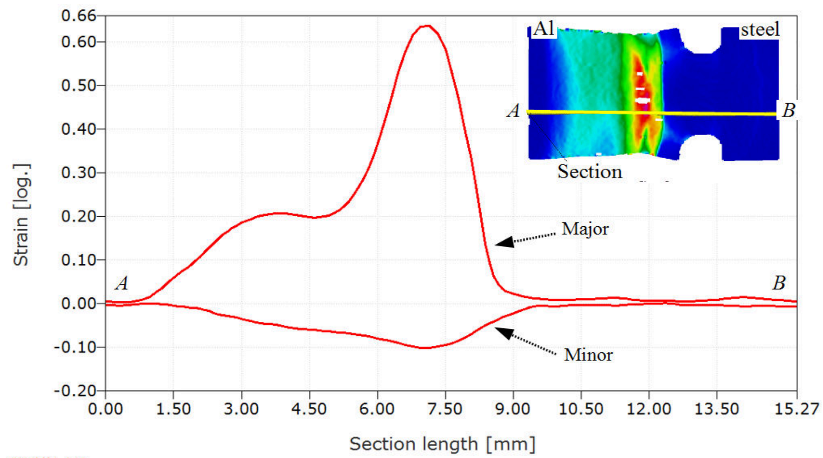

Figure 5.50. Major and minor strain distributions in miniature notched specimen of AA2024/DP780 1.27 mm/1 mm TBBs for Laser/MIG hybrid brazing (0.6 width ratio).

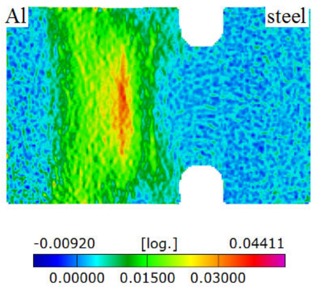

(a) Axial strain=0.75%.

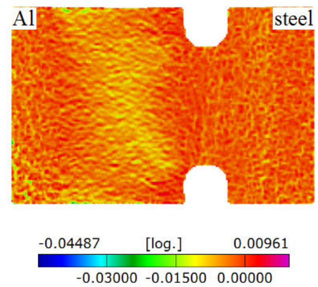

(b) Axial strain=0.75%.

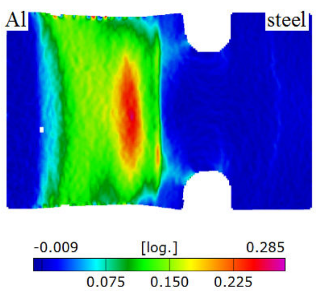

(c) Axial strain=6.5%.

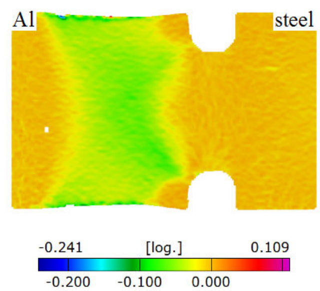

(d) Axial strain=6.5%.

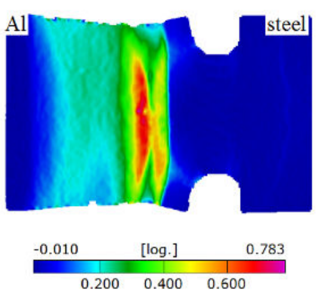

(e) Axial strain=12.5%.

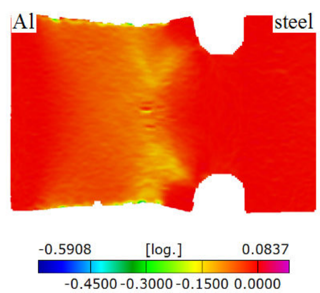

(f) Axial strain=12.5%.

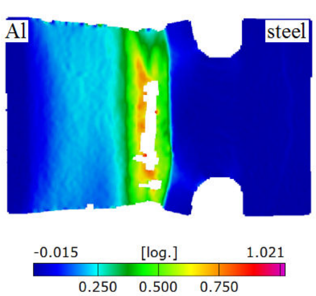

(g) Axial strain=14%.

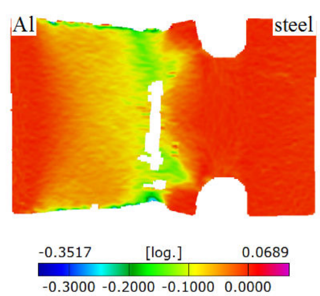

(h) Axial strain=14%.

Figure 5.51. Major (left column), and minor (right column) strain development at different axial strains in miniature notched specimen of AA2024/DP780 1.27 mm/1 mm TBBs for Laser/MIG hybrid brazing (width ratio=0.6).

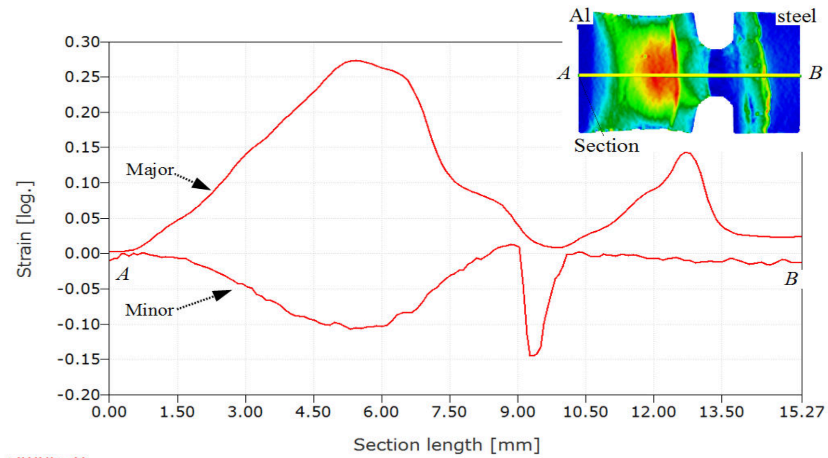

Figure 5.52. Major and minor strain distributions in miniature notched specimen of AA2024/DP780 1.27 mm/1 mm TBBs for Laser/MIG hybrid brazing (width ratio=0.4).

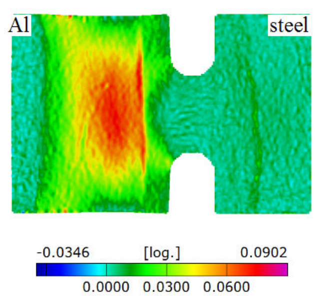

(a) Axial strain=2%.

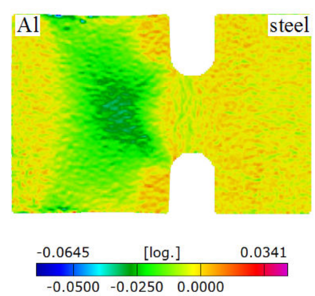

(b) Axial strain=2%.

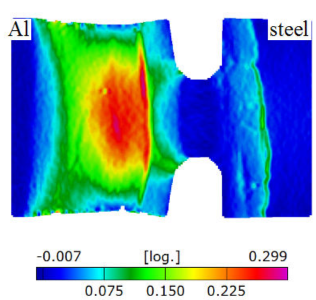

(c) Axial strain=8%.

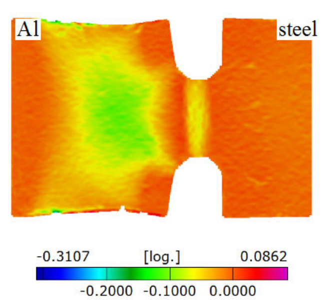

(d) Axial strain=8%.

(figure continued on next page)

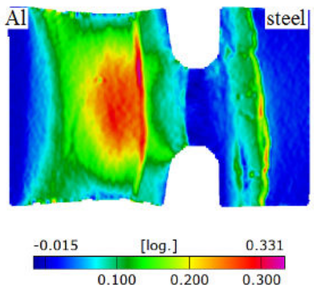

(e) Axial strain=9.5%.

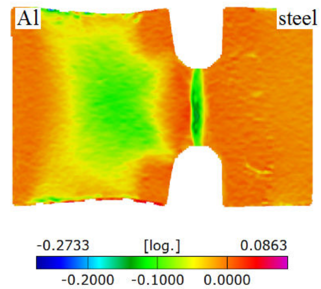

(f) Axial strain=9.5%.

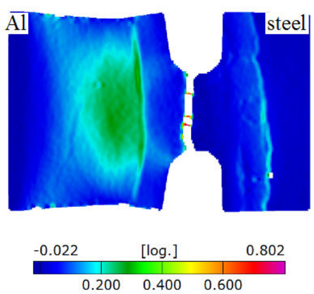

(g) Axial strain=10.5%.

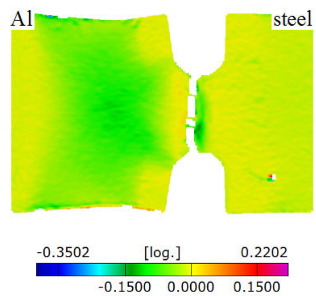

(h) Axial strain=10.5%.

Figure 5.53. Major (left column), and minor (right column) strain development in miniature notched specimen of AA2024/DP780 1.27 mm/1 mm TBBs for Laser/MIG hybrid brazing (width ratio=0.4).

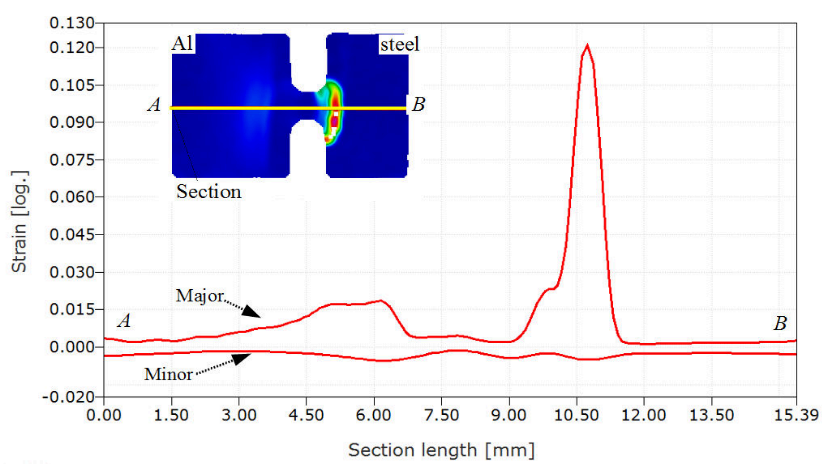

Figure 5.54. Major and minor strain distributions in miniature notched specimen of AA2024/DP780 1.27 mm/1 mm TBBs for Laser/MIG hybrid brazing (0.2 width ratio).

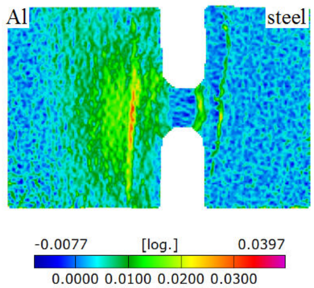

(a) Axial strain=0.45%.

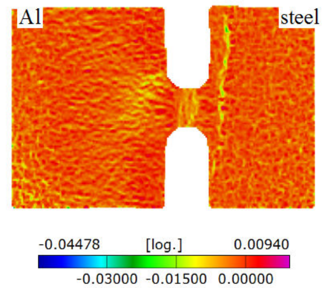

(b) Axial strain=0.45%.

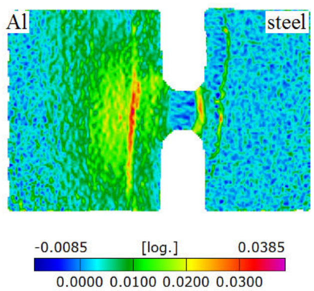

(c) Axial strain=0.55%.

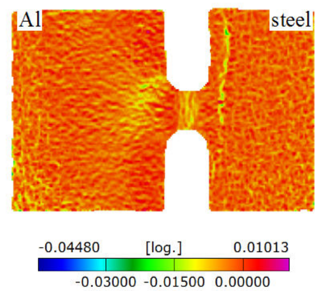

(d) Axial strain=0.55%.

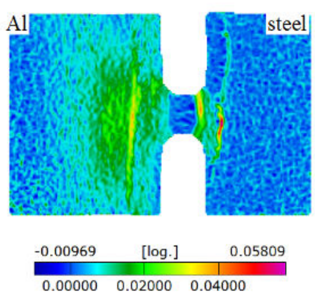

(e) Axial strain=0.65%.

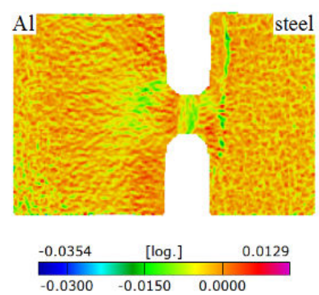

(f) Axial strain=0.65%.

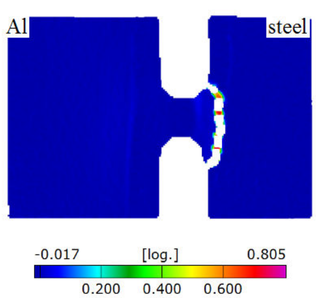

(g) Axial strain=2%.

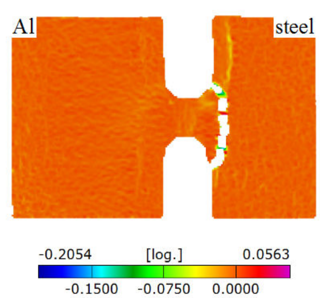

(h) Axial strain=2%.

Figure 5.55. Major (left column), and minor (right column) strain development at different axial strains in miniature notched specimen of AA2024/DP780 1.27 mm/1 mm TBBs for Laser/MIG hybrid brazing (width ratio=0.2).

From the aforementioned results it can be said that the amount of heat input during the brazing process between steel and aluminum is a key factor. It was reported in the literature that decreasing the heat input during the brazing process could improve the mechanical properties of TBBs due to a decrease in the thickness of the IMC layer to less than 10 µm. The present results also indicate that edges preparation conditions, and the degree of degradation of the mechanical properties in the area adjacent to the brazed area also affects the mechanical performance of TBBs. Such degradation is also related to the amount of heat input during the joining process. Susceptibility of the BM and time of exposure to the heat sources during joining process are also important.

Chapter 6

Conclusions and Future Work

6.1 Conclusions

In the current research, the mechanical performance and formability of the welded and brazed TBs were experimentally investigated and analyzed. Two different TBs configurations were utilized, steel-to-steel TWBs and steel-to-aluminum TBBs. Most recent joining techniques in the form of defocused fiber laser beam welding for TWBs, and Laser/MIG hybrid and CMT brazing methods for TBBs were used to produce such TBs. The aim of using such joining method was to reduce the amount of heat input during joining process so as to decrease the deterioration that occurs to the base metal properties, and consequently improve the mechanical performance of the produced TBs. Based on the characteristics of the joining process as well as constituent properties of materials incorporated in TBs, both TBs configurations introduced different behavior during deformation. The major findings of the current research for the 3 proposed objectives are as follows:

i. Assessment of the formability of defocused fiber laser welded steel blanks made from DP780 steel:

DP780/DP780 1 mm/1 mm TWB was successfully produced by using defocused fiber laser welding technique to minimize the amount of heat input during welding process and consequently decrease softening in the HAZ. The deformation behavior of the TWB was compared to that of parent materials.

1. The in-plane uniaxial tensile test results showed that defocused laser beam-based TWBs specimens fractured in BM away from FZ and HAZ. These preliminary results indicate superior result from defocused laser beam welding process without any strain concentration in HAZ.

2. A close match was observed between the ultimate strength of TWBs and parent materials with slight difference in total elongation. In other words, no significant deterioration in elongation and tensile strength of TWBs from defocused fiber laser welding technique was observed.

3. No significant drop in hardness values in the HAZ was observed. In other words, no significant softening occurred in the HAZ.

4. The width of the softening zone was reduced to less than the thickness of the DP sheet. So, plastic flow of softening zone could be suppressed by the strong areas in the vicinity of the softening zone (i.e., constraint effect).

5. The out-of-plane formability results of the TWBs using hemispherical punch test, in terms of failure locations and the LDH values, were nearly similar with that of parent material. No fracture occurred in the softening zone. In addition, a slight increase in the LDH values of TWBs were obtained in plane strain and negative

minor strain paths (strain paths of the free edges weld line). Thus, improving the formability of TWBs in terms of LDH values.

6. The stretchability of the weld area as measured by LDH values showed crucial effect on the total deformation of the TWB. Better stretchability of the fusion area was observed after welding by defocused fiber laser beam welding. The stretchability of TWBs increased with a decrease in hardness difference between FZ and BM as in case of DP steel TWBs.

7. A recently published time-dependent method (t-d method) developed by Martínez-Donaire *et al.* (2014) was utilized for the determination of limit strain values for both TWBs and parent materials.

8. A significant drop in the limit strain values (or FLC) of the TWBs compared to that of parent materials after welding was observed. This was due to the presence of weld areas which increase the strength of the TWB and consequently decrease its ductility.

9. The weld areas (FZ and HAZ) divide the material to two parts on both sides of weld line in the TWB specimen, each side exhibited lower deformation compared to the parent material where the whole material of the tested specimen was involved in the deformation resulting in more gradual evolution of major strain within TWB.

10. The weld line resisted the contraction of TWB in width direction as in case of plane strain and negative minor strain paths with transverse weld line resulting in more gradual evolution of minor strain.

11. The limit strain values and consequently the FLC of TWB depend on the location of necking/fracture point (calculation point). Critical regions such as FZ and its

vicinity showed lower strain values compared to the corresponding regions in parent material.

ii. Devise a new method of formability testing of welded steel blanks of dissimilar thickness and/or strength combinations:

TWBs made from DP780/DP780 1.5 mm/1 mm and HSLA/DP780 2.3 mm/1 mm were tested in both in-plane plane strain and out-of-plane test modes utilizing a new method of double-layer testing of TWBs which compensated the thickness difference and introduced uniform deformation of the tested TWB specimens.

1. For in-plane plane strain test mode, thickness and/or strength differences between TWB sheets were compensated using double-layer method.

2. Close to the plane strain condition, longitudinal welds were subjected to much larger strain compared to the transverse welds.

3. Near plane strain condition was obtained with longitudinal and transverse weld line orientation for both TWBs configurations. Fracture occurred in the thinner/weaker sheet in front and rear TWB. This was due to the thickness difference within each TWB and the limited width of the grips utilized in the tests.

4. For out-of-plane test mode, double-layer TWB showed a significant effect on reducing the weld line movement during hemispherical dome height test. A more uniform deformation was obtained by thickness compensation and force balance for both sides of the tested samples (double-layer TWBs).

5. Increased reduction in thickness (intense necking) was observed in the failure location before fracture occurred in the thinner sheet of the TWB when using double-layer TWB specimen for all strain paths. In contrast, negligible necking was

obtained when conventional single-layer TWB specimen was used. This was attributed to the imbalance in the stress distribution within the single-layer TWBs.

6. A noticeable increase in the limit strain values (or FLC) were observed for double-layer TWB compared to single-layer TWBs. This was attributed to the friction between upper and lower layers in the double-layer configuration that resisted the development of deformation in upper TWB layer which in turn took more time to fracture and consequently higher limit strain. In addition, increased total thickness of the double-layer test specimen compared to single-layer test specimen resulted in more stretching in the upper layer surface and consequently more strain due to bending effect (increased radius of curvature).

7. The double-layer TWB method is new, reproducible and much simpler than other available techniques (e.g., shims and variable blank holder force) in terms of thickness difference compensation as well as force balance in TWBs of thickness and/or strength difference so as to decrease weld line movement.

8. Double-layer test method is a rapid, simple and inexpensive test that can be used to check the quality of the weld and the effect of welding parameters on the TWB, especially when sheets of thickness and/or strength differences are utilized in the welding process.

9. The double-layer TWB method can be used for testing a wide range of materials and thickness combinations.

iii. Assessment of the deformation behavior of steel-to-aluminum TBBs made by Laser/MIG hybrid and CMT brazing methods under uniaxial strain paths: Welding of steel to aluminum has been a challenge in the past. The two brazing methods studied in the present work, Laser/MIG hybrid and CMT brazing, could join the DP780 steel to AA2024 sheets successfully. However, TBBs produced from each method showed significantly different deformation behavior.

1. Uniform appearance of TBBs from CMT brazing method was obtained with longer wetting lengths and better transition between brazing area and steel substrate at the end of wetting lengths.

2. Both brazing methods yielded IMC layer thickness less than 10 µm. The IMC layer thickness was lower for CMT brazing specimens than that of Laser/MIG brazing specimens.

3. Loss of strength was observed for Laser/MIG brazing TBBs specimens. The hardness values measured along through-thickness plane showed a significant drop of hardness profile in the area adjacent to the brazing area in aluminum BM. This was attributed to partial annealing occurred in this area due to the heat input from continuous fusing during brazing process. Failure always occurred in this area.

4. No drop in hardness profile was observed in aluminum BM for CMT TBBs specimens. Aluminum base material was not affected by the heat input and a catastrophic failure occurred in the brazing area at steel/aluminum interface. This was due to the lack of zinc coating layer in the side faying surface which was removed during edge preparation before brazing process.

5. The results of Laser/MIG TBBs notched tensile specimens showed that the degradation of tensile properties of aluminum BM was dominant for all aspect ratios. On decreasing the width aspect ratio by introducing a pair of notches in the width

of the specimen, the location of final fracture depended on the relative strengths (loading capacity) of different regions of TBBs.

6. The results of testing steel-to-aluminum TBBs proved that better wetting length and lower IMC layer thickness are not the only factors that improve the mechanical behavior of TBBs. Edges preparation conditions, and the susceptibility of the BM and time of exposure to the heat sources during joining process are also important.

The general conclusion of the current research is that controlling or even reducing the amount of heat input during welding/brazing process can yield robust welded/brazed joints with less deterioration of the base metal. Consequently, better mechanical strength and mechanical performance of the produced TBBs can be obtained.

Based on the results from the current research, the main contribution are as follows:

1. Using defocused fiber laser beam welding in production of TWBs incorporating DP steel sheets is an effective welding technique to reduce of the amount of heat input during welding and consequently decreasing the base metal distortion (softening) occurred in the DP steel after welding process and improving the formability of TWBs.

2. Using a simple, rapid, reproducible and versatile formability test (double-layer test) in testing the formability of TWBs incorporating thickness and/or strength difference. This method can be used in testing of wide range of thicknesses and materials combinations. The method can aid welding process optimization effort.

3. A study of the formability of steel-to-aluminum TBBs produced by most recent brazing techniques was conducted and analyzed from mechanical behavior point of view. The results proved a correlation between the heat input during welding

and the IMC layer thickness as well as the distortion that occurs in aluminum base metal. The mechanical performance of TBBs is affected by the degree of distortion (partial annealing) that occurs in aluminum base metal.

6.2 Future work

1. The current work was conducted using optimized welding parameters that work well with the tested materials. However, the effected of certain parameters which mostly affect the amount of heat input during welding process of AHSS should be investigated in more detail such as the effect of various defocus distances of fiber laser welding on formability of TWBS.

2. The efficiency of using defocused fiber laser welding technique with other materials of higher martensite contents should be tested and assessed.

3. The formability of TWBs produced by defocused fiber laser welding technique should be assisted by quantitative microscopy work and numerical modeling.

4. For the double-layer TWBs in out-of-plane mode, lubricant should be introduced between the upper and lower TWB to reduce friction. The effect of lubricant on limit strain and weld line movement should be investigated.

5. With respect to steel-to-aluminum TBBs, other aluminum sheets from different aluminum alloys (AA5xxx-AA6xxx) should be joined using both Laser/MIG hybrid and CMT brazing methods and tested to broaden the understanding of deformation behavior and formability of steel-to-aluminum TBBs.

Appendix A

Determination of limit strain values

In the following, the procedures for determination of limit strains at the onset of necking of the deformed specimen using (t-d method) developed by Martínez-Donaire *et al.* (2014) are presented.

First, the surface of the deformed specimen was divided in small facet size. The major strain traces of series of aligned points in section perpendicular to the fracture zone on the surface of specimen were measured. i.e., necking point (point of maximum major strain), and point at the boundary of the necking zone. A six degree polynomial curve fitting was done for the major strain history of the point at the boundary of the necking zone. Then, the 1^{st} derivative (or strain rate) was taken for the fitted curve. The time corresponding to the maximum point of the strain rate was determined. This time was identified as the time for onset of localized instability (or necking). Finally, the major and minor strain values corresponding to this time in the strain traces of the necking point were specified as initial limit strains values. These steps were conducted in three adjacent sections perpendicular to the necking region and the final limit strain was the average value of the three limit strains.

The process of curve fitting and the first derivative (strain rate) were conducted using Origin® software. The drawing of FLC was conducted using drawing software Autocad such that it best fitted the limit strain points. After that, the drawn curve was digitized to receive several points. The coordinates of these points, (i.e., the major and corresponding minor strains), were imported into excel file for constructing the final FLC. The following figures depict the steps for determination of limit strains and drawing of FLCs.

Figure A.1 shows the steps for determination of limit strain for the 177.8 mm full size DP780 parent sheet in biaxial strain path with Teflon lubricant.

Figure A.2 shows the steps for determination of limit strain for the 127 mm DP780 parent sheet in plane strain path.

Figure A.3 shows the steps for determination of limit strain for the 12.7 mm DP780 parent sheet in uniaxial tension strain path.

Figure A.4 shows the average limit strains values in different strain paths and the final FLD for DP780 1 mm parent material and P780/DP780 1 mm/1 mm TWBs.

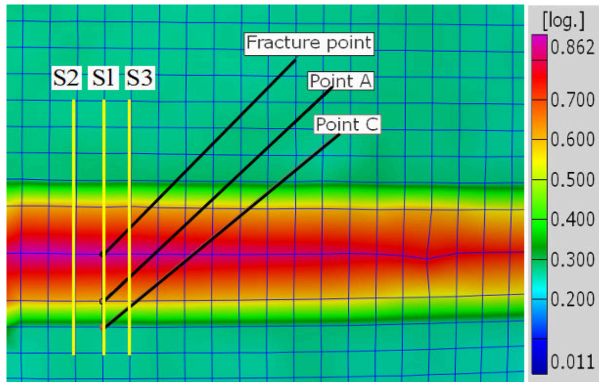

(a) Step 1: Major strain measurements by Aramis.

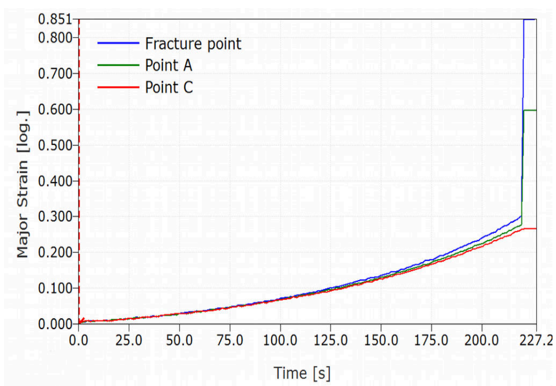

(b) Step 2: Major strain histories.

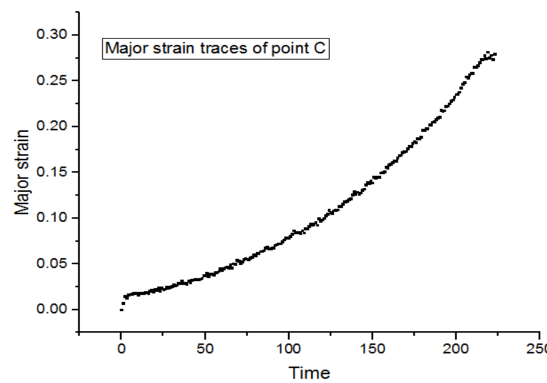

(c) Step 3: Major strain of point C.

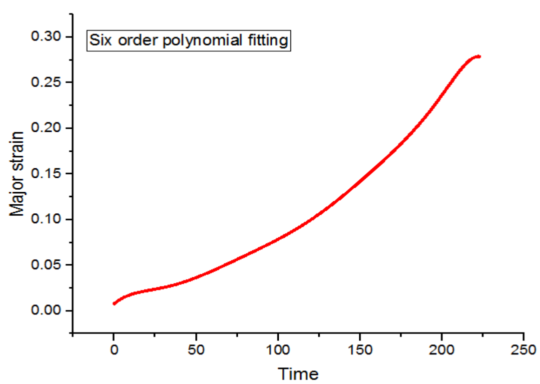

(d) Step 4: Six order polynomial curve fitting.

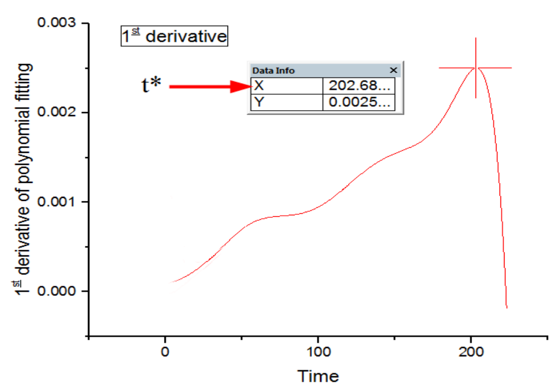

(e) Step 5: 1^{st} derivative.

Figure A.1. Procedure for determination of limit strain using (t-d) method for full size biaxial (Teflon) DP780 parent sheet specimen, (a) major strain mapping measurements by Aramis, (b) major strain histories for the selected points, (c) major strain history of point at the boundary of necking area (point C), (d) six order polynomial curve fitting of major strain of point C, and (e) 1^{st} derivative of the fitting curve.

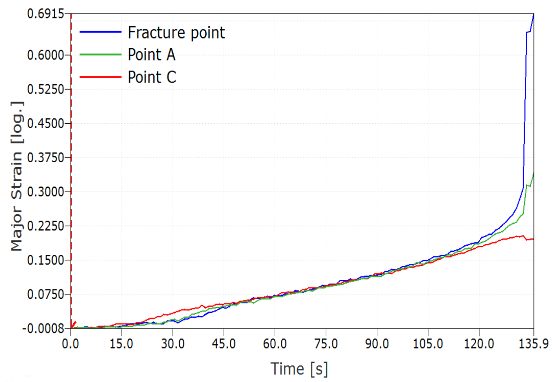

(a) Step 1: Major strain histories.

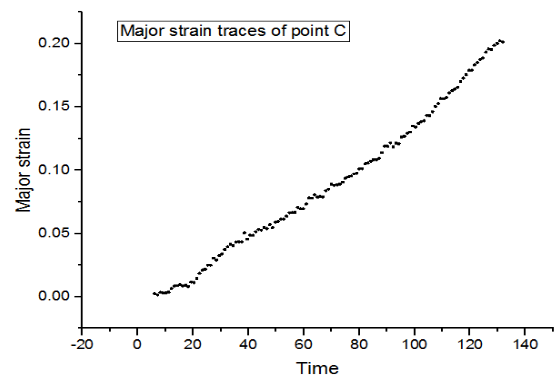

(b) Step 2: Major strain of point C.

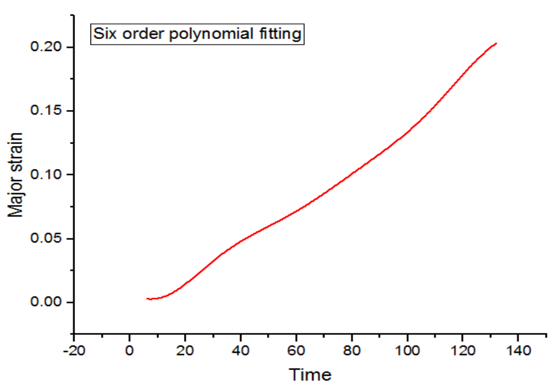

(c) Step 3: Six order polynomial curve fitting.

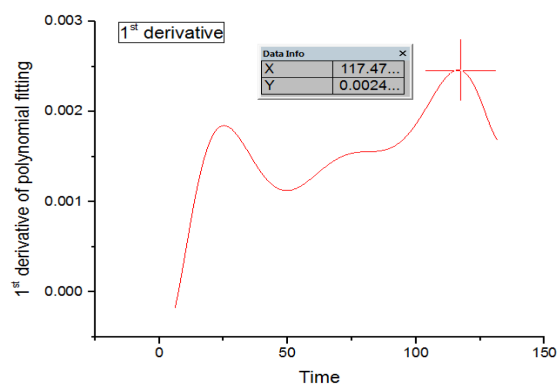

(d) Step 4: 1^{st} derivative.

Figure A.2. Procedure for determination of limit strain using (t-d) method for 127 mm (plane strain) DP780 parent sheet specimen.

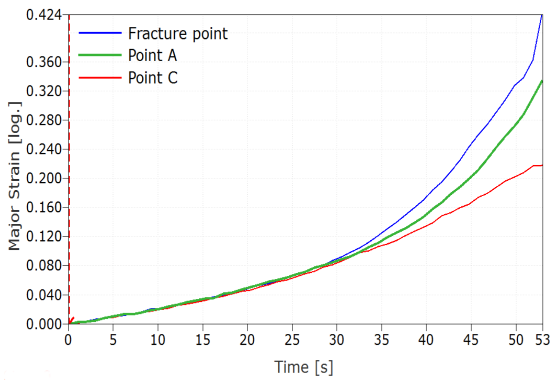

(a) Step 1: Major strain histories.

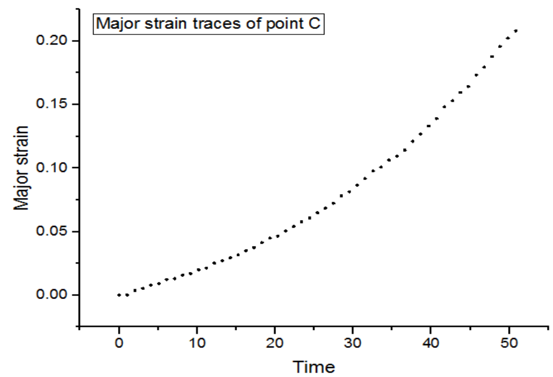

(b) Step 2: Major strain of point C.

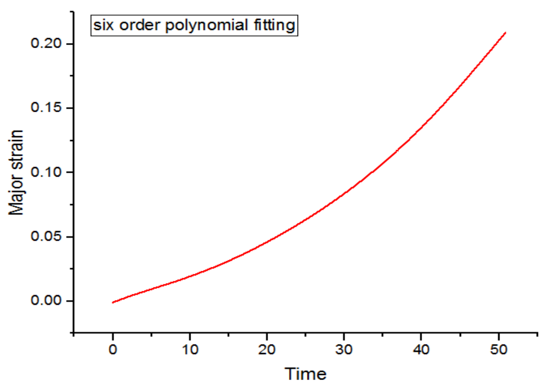

(c) Step 3: Six order polynomial curve fitting.

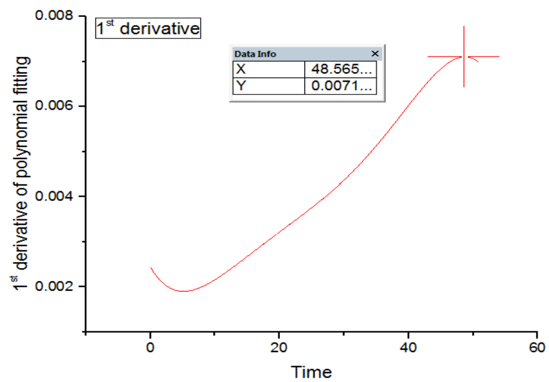

(d) Step 4: 1^{st} derivative.

Figure A.3. Procedure for determination of limit strain using (t-d) method for 12.7 mm (uniaxial tension) DP780 parent sheet specimen.

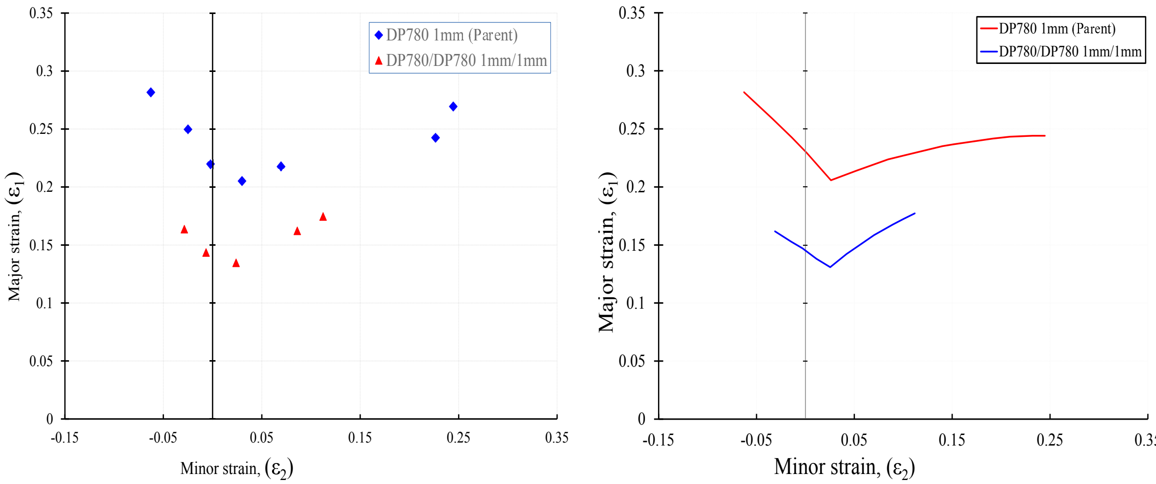

(a) Average limit strains points.

(b) Final FLD.

Figure A.4. Determination of limit strain values and FLD for DP780 1 mm parent material and P780/DP780 1 mm/1 mm TWBs; (a) average limit strains points, and (b) final FLD.

Appendix B

True stress-strain curves of TBBs

The load (F) and displacement are recorded by tensile machine controller. Major strain (ϵ_1) and minor strain (ϵ_2) developments are measured at the point of necking/fracture (localized strains) using Aramis. Strain development in thickness direction (ϵ_3) is measured by:

$$\epsilon_3 = -(\epsilon_1 + \epsilon_2)$$

The current width w and current thickness t are calculated by:

$$w = w_0 e^{\epsilon_2}$$

$$t = t_0 e^{\epsilon_3}$$

Where w_0 and t_0 are the initial width and thickness of aluminum BM of the TBB specimen.

The current area (A) at the point of necking/fracture:

$$A = wt$$

The true stress (σ) is calculated by:

$$\sigma = \frac{F}{A}$$

The true stress (σ) vs. true major strain (ϵ_1) are plotted to construct localized true stess-true strain curves for both Laser/MIG and CMT TBBs specimens as shown in Figure B.5.

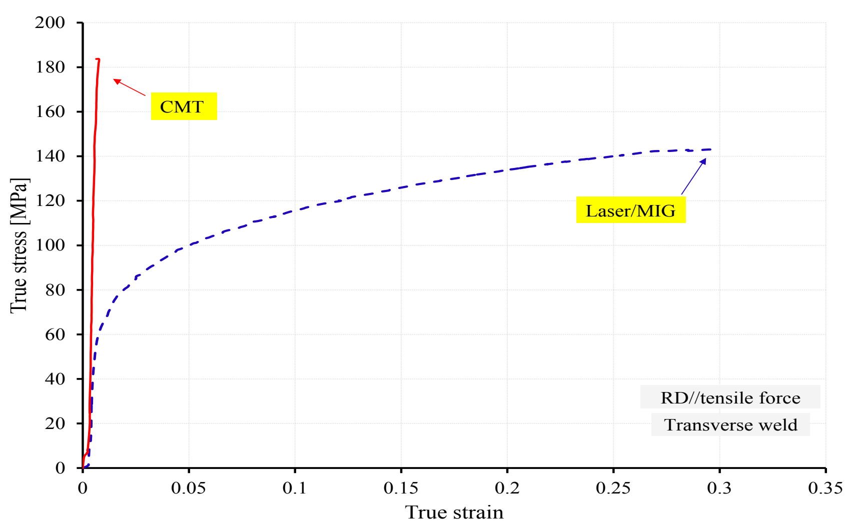

Figure B.5. Localized true stress-true strain curves for AA2024/DP780 1.27 mm/1 mm TBBs specimens produced by Laser/MIG and CMT brazing methods.

Bibliography

Abbasi, M., Ketabchi, M., Shakeri, H., and Hasannia, M. (2012). Formability enhancement of galvanized IF-steel TWB by modification of forming parameters. *Journal of materials engineering and performance*, **21**(4), 564–571.

Agudo, L., Weber, S., Pinto, H., Arenholz, E., Wagner, J., Hackl, H., Bruckner, J., and Pyzalla, A. (2008). Study of microstructure and residual stresses in dissimilar al/steels welds produced by cold metal transfer. In *Materials Science Forum*, volume 571, pages 347–353. Trans Tech Publications.

AluMatter (2010). Wrought Aluminum Alloys. http://www.aluminium.matter.org.uk/. Retrieved: April 2016.

ArcelorMittal (2015a). High strength low alloy (HSLA) steels for cold forming. Technical report, Automotive Worldwide. Accessed: April 2016.

ArcelorMittal (2015b). Multi-thickness laser welded blanks: Tailored Blanks. Technical report, Automotive Worldwide. Accessed: April 2016.

ASTM E8/E8M-13a (2013). Standard test methods for tension testing of metallic materials. *Annual book of ASTM standards. ASTM.*

Bhadeshia, H. and Honeycombe, R. (2006). *Steels: microstructure and properties*. Butterworth-Heinemann.

Bhattacharya, D. (2011). Metallurgical perspectives on advanced sheet steels for automotive applications. In Y. Weng, H. Dong, and Y. Gan, editors, *Advanced Steels*, pages 163–175. Springer.

Bleck, W. (1996). Cold-rolled, high-strength sheet steels for auto applications. *JOM*, **48**(7), 26–30.

Campbell, F. C. (2008). *Elements of metallurgy and engineering alloys*. ASM International.

Carlsson, B., Larsson, J., and Nilsson, T. (2005). Dual phase steels for auto body: design, forming and welding aspects. Technical report, SSAB Tunnplat AB, Borlange. Accessed: April 2017.

Chan, L., Chan, S., Cheng, C., and Lee, T. (2005). Formability and weld zone analysis of tailor-welded blanks for various thickness ratios. *Journal of engineering materials and technology*, **127**(2), 179–185.

Chan, S. M., Chan, L. C., and Lee, T. C. (2003). Tailor-welded blanks of different thickness ratios effects on forming limit diagrams. *Journal of Materials Processing Technology*, **132**(1-3), 95–101.

Cretteur, L. (2015). High-power beam welding of advanced high-strength steels (ahss). In M. Shome and M. Tumuluru, editors, *Welding and Joining of Advanced High Strength Steels (AHSS)*, pages 93 – 119. Woodhead Publishing.

Davies, G. (2012). *Materials for automobile bodies*. Butterworth-Heinemann.

Davies, R. (1978). Influence of martensite composition and content on the properties of dual phase steels. *Metallurgical Transactions A*, **9**(5), 671–679.

Davis, J. R. (2001). *Alloying: understanding the basics*. ASM international.

Dawes, C. (1992). *Laser welding: A practical guide*. Woodhead Publishing.

De Meester, B. (1997). The weldability of modern structural tmcp steels. *ISIJ international*, **37**(6), 537–551.

Denys, R. (1989). The effect of haz softening on the fracture characteristics of modern steel weldments and the practical integrity of marine structures made by tmcp steels.(retroactive coverage). In *International Conference on Evaluation of Materials Performance in Severe Environments.*, volume 2, pages 1013–1027.

Dharmendra, C., Rao, K., Wilden, J., and Reich, S. (2011). Study on laser welding-brazing of zinc coated steel to aluminum alloy with a zinc based filler. *Materials Science and Engineering: A*, **528**(3), 1497–1503.

Dong, H., Hu, W., Duan, Y., Wang, X., and Dong, C. (2012). Dissimilar metal joining of aluminum alloy to galvanized steel with al–si, al–cu, al–si–cu and zn–al filler wires. *Journal of Materials Processing Technology*, **212**(2), 458–464.

Ducker Worldwide (2014). 2015 North American Light Vehicle Aluminum Content Study. Technical report, DriveAluminum. Accessed: April 2016.

Duley, W. W. (1999). *Laser welding*. Wiley.

Fronius (2015). CMT: Cold Metal Transfer. http://www.digitalweldingsolutions.com/cmt.pdf. Retrieved: April 2016.

Ganesh, N. G. (2015). *Bending characteristics and Stretch Bendability of Monolithic and Laminated sheet Materials*. Ph.D. thesis, McMaster University.

Ghosh, A. K. and Hecker, S. S. (1974). Stretching limits in sheet metals: in-plane versus out-of-plane deformation. *Metallurgical and Materials Transactions B*, **5**(10), 2161–2164.

GOM-mbH (2011). GOM Optical Measuring, Aramis v6.3 user's manual. *Braunschweigh, Germany: GOM-mbH*.

Graf, A. F. and Hosford, W. F. (1993). Calculations of forming limit. *Metallurgical and Materials Transactions A*, **24**(11), 2497–2501.

Habibnia, M., Shakeri, M., Nourouzi, S., and Givi, M. B. (2015). Microstructural and mechanical properties of friction stir welded 5050 al alloy and 304 stainless steel plates. *The International Journal of Advanced Manufacturing Technology*, **76**(5-8), 819–829.

Haddadi, F. and Abu-Farha, F. (2015). Microstructural and mechanical performance of aluminium to steel high power ultrasonic spot welding. *Journal of Materials Processing Technology*, **225**, 262–274.

Hecker, S. S. (1974). A cup test for assessing stretchability. *Metals Engineering Quarterly*, **14**, 30–36.

Hilditch, T., de Souza, T., and Hodgson, P. (2015). Properties and automotive applications of advanced high-strength steels (AHSS). In M. Shome and M. Tumuluru, editors, *Welding and Joining of Advanced High Strength Steels (AHSS)*, pages 9–28. "Woodhead Publishing.

Hosford, W. F. and Caddell, R. M. (2011). *Metal forming: mechanics and metallurgy*. Cambridge University Press.

Ion, J. (2005). *Laser processing of engineering materials: principles, procedure and industrial application*. Elsevier Butterworth-Heinemann.

Jain, M. (2000). A simple test to assess the formability of tailor-welded blanks. *International Journal of Forming Processes*, **3**, 185–212.

Kang, S., Min, K., and Kim, K. (2000). A study on resistance welding in steel sheets using a tailor-welded blank. i. evaluation of upset weldability and formability. *Journal of Materials Processing Technology(Netherlands)*, **101**(1), 186–192.

Kannatey-Asibu, E. (2009). *Principles of Laser Materials Processing*. John Wiley & Sons.

Katayama, S. (2004). Laser welding of aluminium alloys and dissimilar metals. *Welding International*, **18**(8), 618–625.

Katayama, S. (2009). Fundamentals of hybrid laserarc welding. In F. O. Olsen, editor, *Hybrid laser-arc welding*, pages 28–46. Elsevier.

Kielwasser, M. (2009). First production experience acquired with laser scanner welding at psa peugeot citroen. *Proc. Of 10th European Automotive Laser Application EALA*.

Kinsey, B. L. and Wu, X. (2011). *Tailor Welded Blanks for Advanced Manufacturing*. Woodhead Publishing.

Kou, S. (2003). *Welding metallurgy*. John Wiley & Sons.

Kreimeyer, M. and Sepold, G. (2002). Laser steel joined aluminium-hybrid structures. In *Proceedings of ICALEO*, volume 2.

Kuryntsev, S. and Gilmutdinov, A. (2015). Welding of stainless steel using defocused laser beam. *Journal of Constructional Steel Research*, **114**, 305–313.

Li, J., Nayak, S., Biro, E., Panda, S., Goodwin, F., and Zhou, Y. (2013). Effects of weld line position and geometry on the formability of laser welded high strength low alloy and dual-phase steel blanks. *Materials & Design*, **52**, 757–766.

Lin, S., Song, J., Yang, C., Fan, C., and Zhang, D. (2010). Brazability of dissimilar metals tungsten inert gas butt welding–brazing between aluminum alloy and stainless steel with al–cu filler metal. *Materials & Design*, **31**(5), 2637–2642.

Lincoln Electric (2016). Hybrid Laser/GMAW welding process. http://www.lincolnelectric.com/en-us/support/process-and-theory/hybrid-laser-gmaw. Retrieved: November 2016.

Maiman, T. H. (1960). Stimulated optical radiation in ruby. *Nature*, **187**(4736), 493–494.

Mallick, P. K. (2010). *Materials, Design and Manufacturing for Lightweight Vehicles*. Woodhead Publishing.

Martínez-Donaire, A., García-Lomas, F., and Vallellano, C. (2014). New approaches to detect the onset of localised necking in sheets under through-thickness strain gradients. *Materials & Design*, **57**, 135–145.

Massalski, T. B., Okamoto, H., Subramanian, P., Kacprzak, L., and Scott, W. W. (1986). *Binary alloy phase diagrams*, volume 1. American Society for Metals Metals Park, OH.

Mathers, G. (2002). *The welding of aluminium and its alloys*. Woodhead Publishing.

Mathieu, A., Pontevicci, S., Viala, J.-c., Cicala, E., Matteï, S., and Grevey, D. (2006). Laser brazing of a steel/aluminium assembly with hot filler wire (88% al, 12% si). *Materials Science and Engineering: A*, **435**, 19–28.

Mathieu, A., Shabadi, R., Deschamps, A., Suery, M., Matteï, S., Grevey, D., and Cicala, E. (2007). Dissimilar material joining using laser (aluminum to steel using zinc-based filler wire). *Optics & Laser Technology*, **39**(3), 652–661.

Maurer, W., Ernst, W., Rauch, R., Kapl, S., Pohl, A., KrÜssel, T., Vallant, R., and Enzinger, N. (2012a). Electron beam welding of a tmcp steel with 700 mpa yield strength. *Welding in the World*, **56**(9), 85.

Maurer, W., Ernst, W., Rauch, R., Kapl, S., Vallant, R., and Enzinger, N. (2012b). Numerical simulation on the effect of haz softening on static tensile strength of hsla steel welds. In *Proc. of 10th Int. Seminar on Weldability*.

Merklein, M., Johannes, M., Lechner, M., and Kuppert, A. (2014). A review on tailored blanksproduction, applications and evaluation. *Journal of Materials Processing Technology*, **214**(2), 151–164.

Messler, R. (2004). *Joining of Materials and Structures*. Elsevier Butterworth-Heinemann.

Moller, F. and Thomy, C. (2013). Laser welding and brazing of dissimilar materials. In S. Katayama, editor, *Handbook of Laser Welding Technologies*, pages 255 – 279. Woodhead Publishing.

Moreira, M. P., Silva, M. L. F., and Castro, M. P. (2012). *Structural connections for lightweight metallic structures*. Springer.

Narasimhan, K. and Narayanan, R. (2011). Deformation of tailor welded blanks during forming. In B. L. Kinsey and X. Wu, editors, *Tailor Welded Blanks for Advanced Manufacturing*, pages 24– 47. Woodhead Publishing.

Nayak, S., Biro, E., and Zhou, Y. (2015). Laser welding of advanced high-strength steels (AHSS). In M. Shome and M. Tumuluru, editors, *Welding and Joining of Advanced High Strength Steels (AHSS)*, pages 71–92. Woodhead Publishing.

Olsen, F. O. (2009). *Hybrid laser-arc welding*. Elsevier.

Omar, M. A. (2011). *The Automotive Body Manufacturing Systems and Processes*. John Wiley & Sons, first edition.

Ozaki, H. and Kutsuna, M. (2009). Laser-roll welding of a dissimilar metal joint of low carbon steel to aluminium alloy using 2 kw fibre laser. *Welding International*, **23**(5), 345–352.

Ozaki, H., Kutsuna, M., Nakagawa, S., and Miyamoto, K. (2010). Laser roll welding of dissimilar metal joint of zinc coated steel to aluminum alloy. *Journal of Laser Applications*, **22**(1), 1–6.

Padmanabhan, R., Oliveira, M. C., and Menezes, L. F. (2008). Deep drawing of aluminium-steel tailor-welded blanks. *Materials and Design*, **29**(1), 154–160.

Padmanabhan, R., Oliveira, M. C., and Menezes, L. F. (2011). Lightweight metal alloy tailor welded blanks. In B. L. Kinsey and X. Wu, editors, *Tailor Welded Blanks for Advanced Manufacturing*, pages 97 – 117. Woodhead Publishing.

Panda, S., Baltazar Hernandez, V., Kuntz, M., and Zhou, Y. (2009). Formability analysis of diode-laser-welded tailored blanks of advanced high-strength steel sheets. *Metallurgical and Materials Transactions A*, **40**(8), 1955–1967.

Qiu, R., Iwamoto, C., and Satonaka, S. (2009). Interfacial microstructure and strength of steel/aluminum alloy joints welded by resistance spot welding with cover plate. *Journal of Materials Processing Technology*, **209**(8), 4186–4193.

Quintino, L., Miranda, R., Dilthey, U., Iordachescu, D., Banasik, M., and Stano, S. (2012). Laser welding of structural aluminium. In M. P. Moreira, M. L. F. Silva, and M. P. Castro, editors, *Structural Connections for Lightweight Metallic Structures*, pages 33–57. Springer.

Schwartz, M. M. (2003). *Brazing*. ASM international.

Shah, L. H. and Ishak, M. (2014). Review of Research Progress on AluminumSteel Dissimilar Welding. *Materials and Manufacturing Processes*, **29**(8), 928–933.

Sharma, C., Dwivedi, D., and Kumar, P. (2012). Influence of in-process cooling on tensile behaviour of friction stir welded joints of aa7039. *Materials Science and Engineering: A*, **556**, 479–487.

Shi, H., Qiao, S., Qiu, R., Zhang, X., and Yu, H. (2012). Effect of welding time on the joining phenomena of diffusion welded joint between aluminum alloy and stainless steel. *Materials and Manufacturing Processes*, **27**(12), 1366–1369.

Shome, M. and Tumuluru, M. (2015). *Welding and joining of advanced high strength steels (AHSS)*. Woodhead Publishing.

Song, J., Lin, S., Yang, C., and Fan, C. (2009). Effects of si additions on intermetallic compound layer of aluminum–steel tig welding–brazing joint. *Journal of Alloys and Compounds*, **488**(1), 217–222.

Sreenivasan, N., Xia, M., Lawson, S., and Zhou, Y. (2008). Effect of laser welding on formability of dp980 steel. *Journal of Engineering Materials and Technology*, **130**(4), 041004.

Sun, J., Yan, Q., Gao, W., and Huang, J. (2015). Investigation of laser welding on butt joints of al/steel dissimilar materials. *Materials & Design*, **83**, 120–128.

Sun, Z. and Ion, J. C. (1995). Review Laser welding of dissimilar metal combinations. *Journal of Materials Science*, **30**, 4205–4214.

Thomy, C. and Vollertsen, F. (2012). Laser-mig hybrid welding of aluminium to steeleffect of process parameters on joint properties. *Welding in the World*, **56**(5-6), 124–132.

Tricarico, L. and Spina, R. (2010). Experimental investigation of laser beam welding of explosion-welded steel/aluminum structural transition joints. *Materials & Design*, **31**(4), 1981–1992.

Vaamonde, C. E. and Vázquez, G. J. (2012). *Structural Connections for Lightweight Metallic Structures*, chapter Laser Beam Welding and Automotive Engineering, pages 59–84. Springer.

Wei, C., Zhang, J., Yang, S., Sun, L., Tao, W., Wu, F., and Xia, W. (2015). Improving formability of laser welded automotive dual phase steels with local cooling. *Science and Technology of Welding and Joining*, **20**(2), 145–154.

Wirth, A., Kreimeyer, M., Gnauk, J., Thomy, C., and Vollertsen, F. (2007). Analyses on the phase seam of a laser-mig joined aluminum-steel sample. In *Proceedings of the 4 th International WLT-Conference on Lasers in Manufacturing*, pages 111–115.

WorldAutoSteel (2014). *Advanced High-Strength Steels Application Guidelines Version 5.0*. WorldAutoSteel. Available from:http://www.worldautosteel.org.

Xia, M., Sreenivasan, N., Lawson, S., Zhou, Y., and Tian, Z. (2007). A Comparative Study of Formability of Diode Laser Welds in DP980 and HSLA Steels. *Journal of Engineering Materials and Technology*, **129**(July), 446–452.

Xu, W., Westerbaan, D., Nayak, S., Chen, D., Goodwin, F., and Zhou, Y. (2013). Tensile and fatigue properties of fiber laser welded high strength low alloy and dp980 dual-phase steel joints. *Materials & Design*, **43**, 373–383.

Yang, J., Li, Y., Zhang, H., Guo, W., Weckman, D., and Zhou, N. (2015). Dissimilar laser welding/brazing of 5754 aluminum alloy to dp 980 steel: Mechanical properties and interfacial microstructure. *Metallurgical and Materials Transactions A*, **46**(11), 5149–5157.

Yasuyama, M., Fukui, K., Ogawa, K., and Taka, T. (1996). Spot welding of aluminum and steel sheet with insert of aluminum clad steel sheet. *Sumitomo Met*, **48**(4), 87–95.

Zadpoor, A., Sinke, J., and Benedictus, R. (2007). Mechanics of tailor welded blanks: an overview. *Key Engineering Materials*, **344**, 373–382.

Zhang, H. and Liu, J. (2011). Microstructure characteristics and mechanical property of aluminum alloy/stainless steel lap joints fabricated by mig welding–brazing process. *Materials Science and Engineering: A*, **528**(19), 6179–6185.

Zhang, W., Sun, D., Han, L., and Liu, D. (2014). Interfacial microstructure and mechanical property of resistance spot welded joint of high strength steel and aluminium alloy with 4047 alsi12 interlayer. *Materials & Design*, **57**, 186–194.